Modeling Fire Spread in Large Compartments using Computational Fluid Dynamics

by

Alyssa DeSimone

A dissertation submitted in partial fulfillment
of the requirements for the degree of
Doctor of Philosophy
(Civil Engineering)
in the University of Michigan
2021

Doctoral Committee:

Associate Professor Ann Jeffers, Chair
Professor James Barber
Professor Sherif El-Tawil
Professor Jason P. McCormick

Alyssa DeSimone

adesimon@umich.edu

ORCID iD: 0000-0002-8716-2285

Dedication

This dissertation is dedicated to my family, friends, and colleagues who have supported me throughout this journey. Most of all, this work is dedicated to my fiancé Lucca. Thank you for your constant love, understanding, and guidance. Without all of you, this work would not have been possible.

Acknowledgements

First, I would like to thank my advisor Prof. Ann Jeffers for her constant support and guidance throughout my Ph.D. work. In addition to proving excellent insight into my work and demonstrating what it means to be a good researcher, she has always shown me patience and kindness which I greatly appreciate. I am also grateful for the support and encouragement of my committee members, Prof. Barber, Prof. El-Tawil, and Prof. McCormick. Their advice and guidance have improved the work presented in this dissertation.

I would also like to thank the members of the Jeffers' research group, including Ha Nguyen, Paul Beata, Ning Liu, and Jason Martinez, and my colleagues from the GGB 1267A office. Throughout my time at Michigan, they have been there to support me and make my time at Michigan more enjoyable.

The dissertation would not be possible without the financial support from the Department of Civil and Environmental Engineering, the Society of Fire Protection Engineers through their Student Research Grant, and the Gerstacker Fellowship. This research was also supported in part through computational resources and services provided by the University of Michigan's Advanced Research Computing (ARC) Flux HPC cluster.

Table of Contents

List of Tables

List of Figures

Abstract

Architectural design of buildings in the 21st century has emphasized large open spaces, atriums, high ceilings, and glazed facades. Traditional design fires developed for small enclosures assume uniform burning throughout the compartment and may not apply to these modern building layouts. In contrast, large compartment fires burn over a limited area and move across a floor system over time resulting in non-uniform and transient heating [1]. Recent advances have introduced simplified models for spreading (i.e., "traveling") fires in large compartments, but the models have not been experimentally validated and only account for 1D fire spread. The purpose of the work presented in this dissertation is to (1) improve thermal and structural modeling of large compartments during traveling fire events and (2) to use these improved modeling techniques to characterize the range of possible thermal environments that a compartment can experience during a traveling fire. The goal of this work is to aid engineers in designing effective fire protection for large compartments.

In order to model non-uniform temperatures and realistic fire dynamics, computational fluid dynamics (CFD) simulations of fire are utilized throughout this dissertation. The CFD fire simulations are coupled with finite element (FE) models to study the thermo-mechanical structural fire response. In the existing literature, a wide range of parameters are used when determining the boundary condition at the structure-fire interface. This dissertation investigates the various methods to identify best practices while balancing accuracy and computational expense.

A novel fire spread model for large compartments using a transient flux-time product model for ignition was formulated to model realistic traveling fire behavior. The fire (modeled using CFD) begins with the assumed ignition of an object. The fire is allowed to spread realistically from object to object through the use of a transient flux-time product ignition model. Burning objects are represented as equivalent burners to reduce computational expense. The fire spread model for large compartments is validated using experimental data from NIST [2].

A parametric study of fire spread was performed using the transient flux-time product ignition model to characterize the behavior of fire spread in large compartments, and to quantify the range of thermal environments a structure can experience when subjected to traveling fires. Compartment characteristics and fire inputs were varied such as the ignition location of the fire, ventilation conditions, heat release rate of the objects, and fuel load density. The results of this study are compared to the simplistic traveling fire model (TFM) to determine if current models are adequate for predicting the thermal environment in large compartments.

The work in this dissertation shows that fire spread can be accurately modeled using computational fluid dynamics through the implementation of a transient flux-time product ignition model, and that the response of structural members to localized burning can be accurately modeled through the use of an appropriate boundary condition at the structure-fire interface. The parametric fire spread study showed that ventilation conditions and the fuel load density had a significant impact on the thermal environment in the compartment. Additionally, when this detailed model was compared to TFM, it was concluded that large temperature gradients occur through the width of the compartment that may be significant for structural response. Also, TFM underpredicts far field temperatures given certain compartment conditions.

Chapter 1 Introduction

Advances in structural fire engineering have the potential to improve lives and livelihoods. In the past year, there was estimated to be over one million fires, tens of thousands of civilian deaths and injuries, and tens of billions in direct property damage in the United States alone, according to the National Fire Protection Association [3]. Therefore, it is extremely important that structural fire design is continuously updated to reflect new advancements in fire dynamics and is applicable to buildings that incorporate new architectural trends. Architectural design of buildings in the 21st century has, for example, emphasized large open spaces, atriums, high ceilings, and glazed facades. Traditional design fires that are presently used were developed for small enclosures, in which it is assumed that burning is uniform throughout the compartment. These models may not apply to modern building layouts.

In contrast, large compartment fires burn over a limited area and move across a floor system over time resulting in non-uniform and transient heating [1]. This behavior has been observed in numerous large, accidental fires, most notably, the World Trade Center Towers 1, 2 [4-5], and 7 [6], the Windsor Tower in Spain [7], Faculty of Architecture at TU Delft in the Netherlands [8], Interstate Bank in Los Angeles [9], the One Meridian Plaza in Philadelphia [10], and the Plasco Building in Tehran [11]. In these real fire events, the fires were observed to have traveled horizontally across floor plates and vertically between floors. In addition, the burning duration was much larger than prescribed by traditional fire design methods, which can have a significant impact

on structural heating. The report on WTC building 7 [6] concluded the building's collapse was caused by an uncontrolled traveling fire, and the report on the Faculty of Architecture Building at TU Delft [8] concluded that the collapse of the building was in part due to the building's large open compartment design which allowed the fire to spread freely through entire floors. The report calls for the "characterization for the movement of large fires and how such fires affect structural response" [8].

Moreover, structural engineers are moving away from using traditional design fires in favor of performance-based design methodologies, which can have economic and safety advantages. Traditional design fires are often presented as a standard time-temperature curve or set of time-temperature curves that can be used to approximate fire behavior in a compartment. These traditional design fires have many limitations; they often employ simplistic models of fire dynamics and do not apply to large, open-space building layouts. In contrast, performance-based design approaches provide a flexibility and an engineering approach to fire protection. They can be applied to any building layout as long as the designer shows that the design is safe and that any deviations from prescriptive design codes are acceptable. Characterizing a realistic design fire for large compartments will aid current structural fire engineers in their endeavor to provide safe, economic, sustainable, and modern structural fire designs.

This dissertation is motivated by the need for more robust computational tools to predict fire spread in large open compartments. The novel fire spread model using a transient flux-time product model for ignition outlined in this dissertation realistically models fire progression by considering fire spread from object to object through use of a transient flux-time product ignition model. The non-uniform heating of structural elements will be modeled using computational fluid dynamics. The research seeks to understand how realistic fire spread in large compartments affects

the response of the structure. This novel fire spread model for large compartments is the most realistic design fire for structural application and can be used by fire protection and structural fire engineers to make the most informed decisions regarding fire design of modern buildings.

This document is made up of the following chapters. Chapter 1 provides an introduction and motivation to the research presented in this dissertation, and Chapter 2 provides a review of literature related to modeling fire behavior. Chapter 3 is a manuscript entitled, "Best Practices for Modeling Structural Boundary Conditions due to a Localized Fire," which originally appeared in the journal *Fire and Materials* [12]. Chapter 4 is a draft of a manuscript that describes the derivation and framework for the fire spread model that forms the basis for this dissertation. It also presents validation of the fire spread model. Chapter 5 is a draft of a manuscript that presents a parametric fire study using the fire spread model presented in this dissertation. It analyzes the effect that certain compartment and fire characteristics have on fire behavior and compares the results of the study to current fire models. Chapter 6 presents the conclusions of this dissertation and provides recommendations for future work.

Chapter 2 Background

The background section of this dissertation will focus on a discussion of the existing design fires and the corresponding structural response. The section will end with a discussion of computational fire models. Current design fires to be discussed are the standard fire curve, Eurocode parametric time-temperature curves, fire models for large firecells, the traveling fire model and the extended traveling fire model.

2.1 The Standard Fire Curve

The standard fire curve is the basis for most structural fire design building codes (BS 476 [13], ISO 834 [14], and ASTM E119 [15]). It was published in 1917 and was meant to represent the time-temperature development of a worst-case (i.e., post-flashover) fire scenario. It is well known that the standard fire curve does not represent a realistic fire [16]. Many limitations of the standard fire have been identified since, such as the exclusion of the cooling phase of the fire, which can have a large impact on structural response [17]. Additionally, the standard fire does not consider various parameters that influence fire development such as geometry of the compartment, fuel load or ventilation conditions. Most importantly, the standard fire curve assumes that all structural components in the compartment are subjected to uniform heating, which is an inaccurate assumption, especially when considering large modern enclosures.

2.2 Eurocode Parametric Time-Temperature Curves

The Eurocode parametric time-temperature curve [18] addresses many of the limitations of the standard fire curve. It considers the total compartment area, the thermal inertia of the boundaries or wall linings, the ventilation conditions and the fuel load density when determining the time-temperature curve, but they have limited applicability. For example, they can only be used for the fire design of compartments that have a floor area less than 500 m^2, no openings in the roof, compartment height less than 4 m, and wall linings that have a thermal inertia between 100 and 2,200 $J/m^2s^{1/2}K$. Most notably this excludes glass facades and large enclosures, which are common features in modern buildings. It was found that because of these limitations, the Eurocode parametric time-temperature curves are not applicable to 92% of the total volume of buildings [19]. This method also does not consider radiation from soot [16]. In addition, the parametric fire curve also employs a uniform heating assumption to all structural components in the compartment.

2.3 Fire Models for Large Firecells

This design fire model [20-21], divides each compartment into a number of "firecells" referred to as "design areas". Each "design area" has an individual classification as either fire, preheat, smoke logged or burned out. Design areas have a designated area of 50 m^2. The fire spread rate is based on experimental data [22], and is specified as 1 m/s for well ventilated conditions and 0.5 m/s for less ventilated conditions. Windows are assumed to break when the gas temperature near the window reaches 350°C. The Eurocode parametric time-temperature curves are employed by this method to determine temperatures of the burning firecells. Fixed temperatures are assigned to the pre-heating and burnt out firecells.

This fire model employs a uniform heating assumption for each design area but not throughout the entire compartment, which is an improvement on previous design fires, but the

author noted that it uses many assumptions regarding fire size, ventilation, fire spread, fuel distribution and fuel type which results in an overly simplistic model that should only be used as a research tool.

2.4 Traveling Fire Model (TFM)

In an effort to provide structural fire engineers with a realistic design fire for modern buildings, the travelling fire methodology (TFM) was developed [1, 23-24]. TFM divides the design fire into two distinct thermal fields: the near field and the far field. The near field represents the part of the floor system that is actively burning and where structural elements are exposed to flames. The far field represents the part of the floor system that is not actively burning and where structural elements are being heated due to hot combustion gases. The near field temperature is assumed to be uniform at 1200ºC, representing a worst-case scenario. The far field temperature is represented by Alpert's ceiling jet correlation [25] which notably assumes an unconfined ceiling with no accumulated smoke layer.

TFM accounts for a family fires that vary in size (percentage of floor area subjected to the near field temperatures) from 1%-100% of the floor area, duration, and temperature. In TFM, smaller area fires result in lower overall temperatures but a longer fire duration, while larger area fires result in higher overall temperatures and a shorter fire duration. TFM assumes a uniform fuel load across the floor system and therefore a uniform heat release rate of the fire. The fire progression is simplified to a single linear path, meaning the fire will start on one side of the floor system and progress linearly to the other end of the floor system. This assumes that the width of the floor system burns uniformly.

TFM was an important improvement in structural design fires but its uniform near field temperature, one dimensional fire path, uniform fuel distribution, inability to model a ventilation-

controlled fire, and the far field temperature model are significant limitations to the ability of TFM to model realistic fires dynamics.

2.4.1 Improved Traveling Fire Model (iTFM)

Recently, an improved version of the original traveling fire was developed [26]. In the original TFM, a family of fires that ranged from 1%-100% of the floor area was considered. The authors noted it is unlikely that a very thin line fire (e.g. 1% of floor area) across the width of the compartment would spread, or that in a very large compartment, the entire floor would be burning at once (e.g. 100% of the floor area). To address this issue and to reduce computational expense, the authors sought to limit the range of fires that TFM would consider. A calculation was introduced to determine the realistic maximum and minimum fire size based on fuel load density, heat release rate per unit area, and the minimum and maximum fire spread rate based on experimental and real fire data. The far-field model in iTFM is still based on Alpert's correlation [25], but the authors developed their own analytical equations for the far-field temperatures. These equations allow for the rapid calculation of temperature variations and remove errors that were imposed by the discrete method used in TFM. In addition, the near-field temperature model in iTFM was expanded to consider a range of temperatures. The authors introduced a flapping angle to determine the length of ceiling subject to impinging flames called the flapping length. Then, the average temperature over this length is determined based on the far-field temperatures and peak-near field temperature (1200°C). Ultimately, this results in a lower near-field temperature than TFM.

While the improved traveling fire model makes notable improvements, such as the near field temperature model, there are many shortcomings to the original traveling model that it does

not address, such as uniform fuel distribution, the one-dimensional fire path and ventilation-controlled fires.

2.4.2 Extended Traveling Fire Model

An additional traveling fire model was developed for large compartments with fire resistant islands [27-28]. It employs a traveling version of Hasemi's localized fire model which defines the near field temperatures [29] and the far field temperatures are determined through the FIRM zone model [30] which allows for the consideration of a ventilation-controlled fire. The method generally assumes a uniform fuel load but includes an option for the designer to distribute additional lumped fuel at the most critical or vulnerable parts of the structure. The spread rate of the front edge of the fire is assumed to be constant and is determined based on available experimental data. The back-edge location of the fire is dictated by the burn out time, a factor that determined by the maximum heat release of the fire and the fuel load density. The spread rate of the front edge of the fire and the burn out time determine the burning area of the fuel. This model considers flashover (i.e., a transition from the localized fire model to a compartment fire model) when certain thresholds are met, such as the hot smoke layer exceeds a temperature of 500°C or heat flux at the floor level exceeds 20 kW/m^2. The fire path of the extended traveling fire model is predetermined. It travels around the perimeter of the floor system with the fire-resistant island in the center.

The extended traveling fire model accounts for variable near field temperatures and an accumulated smoke layer, but it still employs a predetermined fire path and assumes that all available fuel is consumed during the fire which may not realistically represent the true fire spread. Because of its use of a zone model to represent far field temperatures, it assumes temperatures in the far field are uniform. It also assumes a uniform fire diameter and heat release rate of the fire,

parameters that change over the course of a natural fire. Additionally, it is only applicable to floor plans that contain a fire-resistant center island, and Hasemi's fire model is not applicable when fire diameters are larger than 10 m or the heat release rate of the fire exceeds 50 MW [18].

2.5 Structural Response

2.5.1 Response of Structures to Localized Heating

Recent studies suggest that the assumption of uniform heating used in traditional structural fire design cannot be assumed to be conservative, especially in the case of localized heating, which occurs during a traveling fire. Zhang et al. [31] suggests that the failure mode of a beam may be different if it is exposed to a localized heating instead of the standard fire curve, which assumes uniform heating. In particular, Zhang et al. [31] found that when many beams were subjected to the standard fire curve, they failed due to deflection limitations but when they were subjected to a localized heating, they failed due to buckling. A study by Dwaikat et al. [32] on the effect of thermal gradients in steel columns concluded that the thermal gradient caused a bending moment in the column, which reduced the column's capacity. These studies suggest that structural members subjected to thermal gradients behave fundamentally different from how they were originally conceived in traditional fire models, leading to the potential for premature failure. In addition, another study by Zhang et al. [33] found that the failure temperature of steel columns subjected to an adjacent localized fire could be higher or lower than the failure temperature predicted by the standard fire curve. These studies show that the current design codes do not have the capability to predict the behavior of structural elements subjected to non-uniform heating, and therefore a more detailed approach to modeling these structures is needed.

2.5.2 Response of Structures to the Traveling Fire Model

Law et al. [34] applied the traveling fire methodology with a range of fires from 1%-100% of the floor to a generic reinforced concrete frame. The standard fire curve and the Eurocode parametric fire curves for a short hot fire, and a long cool fire were also applied to the concrete frame for comparison. The study found that traveling fires resulted in a more critical response of the structure when compared to the Eurocode parametric fires, especially for smaller size fires, and concludes that the Eurocode fires cannot be assumed to be a conservative design model. A fire size equal to 25% of the floor area in TFM resulted in the most severe structural response. Additionally, the study considered fire paths besides a linear progression. It modeled a corner fire that spread around the building's core, a ring fire that progressed inward and a ring fire that progressed outward. It was found that the corner fire resulted in the most critical response of the structure, although this fire path is not considered within the traveling fire model.

TFM was applied to a generic concrete floor system and a thermal analysis was conducted [1]. A family of fires was considered with fire areas ranging from 1% to 100% of the floor area. The study found that fire sizes ranging from 5%-20% of the floor area were most critical for the structure. The smaller size fires (5-20% of the floor area) produce highly nonuniform temperatures across the floor system and resulted in the highest bay temperatures and peak rebar temperatures. The study showed that it is essential to model the entire compartment (i.e., both near field and far field) because members may be preheated during a long duration traveling fire.

Rackauskaite et al. [26] applied the improved Traveling Fire Model to a steel and concrete frame. The family of fire sizes investigated was reduced to a range of 0.3-55% of the floor area. The peak steel beam temperatures occurred for a 10% size fire, and peak temperature within the

compartment was found to occur near the end of the fire path. This response is similar to that predicted by Stern-Gottfried and Rein [1].

Additionally, Martinez [35] applied the improved Traveling Fire Methodology to two steel-concrete composite floor systems. This study found that both floor systems designed with a 1-hr fire protection rating exceeded their displacement limit when subjected to traveling fire exposure. Floor systems designed with a 2-hr fire protection rating only exceeded their displacement for the 5% and 10% size traveling fires. This demonstrates that current fire protection designs may be unsafe against traveling fires.

2.6 Computational Fire Models

2.6.1 Zone Fire Models

Zone models solve the conservation equations for relatively large control volumes. There is a number of zone models used in fire protection engineering, and the majority of zone models divide the compartment into two distinct "zones" [36-37]. The first zone is a lower, cooler layer, and the second zone is an upper, hot layer. The hot, upper layer and the cooler, lower layer are both assumed to be of uniform temperature and composition. The advantage of zone models is it allows for the consideration of specific building materials, ventilation conditions, and room furnishings. Additionally, zone models are relatively computationally inexpensive. But, the uniform treatment of the hot, upper layer in zone models limits it applicability to large compartments [38-39].

2.6.2 Computational Fluid Dynamics Fire Models or Field Models

Computational fluid dynamics (CFD) solves the full, partial differential equation set for the conservation of mass, momentum, energy and species. A CFD model divides the compartment

into thousands or millions of elements. As with zone models, the user can specify a range of characteristics of the compartment. Building materials, compartment linings, ventilation conditions, and room furnishings can all be explicitly modeled by the user. Currently, CFD fire models are the most detailed approach available to modeling fire behavior. Most importantly, CFD models only assume uniform temperature within an element, and therefore with a sufficient number of elements, CFD fire models can be used to accurately predict fire behavior in large compartments [36, 39-40].

While CFD is a powerful tool for modeling fire dynamics, there are limitations. Currently, empirical understanding of fire behavior exceeds the ability to model it computationally. Specifically, CFD codes lack the ability to reliably predict fire spread, extinction, and suppression, as well as carbon monoxide and smoke production [39]. The work presented in this dissertation overcomes these limitations by developing a novel model for fire spread and using it in tandem with a current CFD code. This model has the potential to expand current CFD capabilities in regard to modeling fire spread.

In this dissertation, the CFD code Fire Dynamics Simulator (FDS) [40], developed by the National Institute of Standards and Technology, is used as a tool to model fire behavior. FDS numerically solves a form of the Navier-Stokes equation that can be used for "low-speed, thermally-driven flow." Turbulence is modeled using Large Eddy Simulation (LES). The combustion model uses a single step, mixing-controlled chemical reaction that uses three lumped species (i.e., air, fuel and products) and radiative heat transfer is solved for using the radiation transport equation for grey gas [40].

Chapter 3 The Boundary at the Structure-Fire Interface

This chapter has been previously published in *Fire and Materials* [12].

3.1 Introduction and Background

A common approach to simulating structural members subjected to localized heating, is a coupled computational fluid dynamics (CFD) - finite element (FE) model [41]. The CFD analysis of the fire allows for the full consideration of the non-uniform effect of the localized fire. Heat flux and temperature data from the CFD analysis are passed to the FE model as a thermal boundary condition, and the FE analysis determines the thermal and mechanical response of the structure. An example of this can be seen in Figure 3.1, where the image on the left is the CFD simulation of an I-beam subjected to a pool fire. Data from the CFD simulation is transferred to the FE analysis, and the image on the right shows the solid heat transfer analysis of the I-beam due to the pool fire.

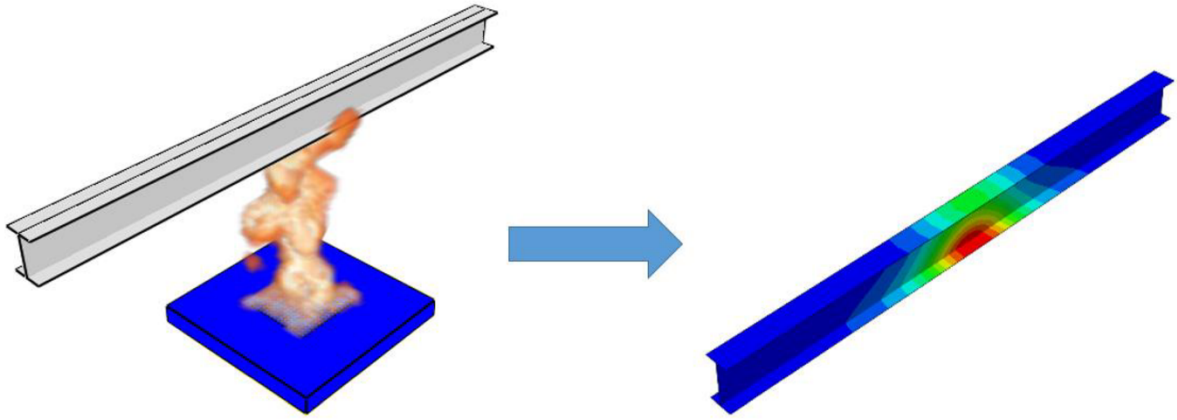

Figure 3.1 - CFD-FE coupling schematic

The study described in this chapter focuses on the representation of the boundary condition at the structure-fire interface for coupled CFD-FE analyses of localized fires. In the existing literature [18], [42]–[46] many different methods and parameters have been used when determining the thermal boundary conditions at the fire-structure interface. The issue is that the methods being used lack consistency, which could lead to significant modeling errors when applied in practice. The purpose of this study is to investigate the existing methods for accuracy and computational efficiency and then to identify best practices so as to guide readers in the very complicated CFD-FE analysis of structures in fire. This study also aims to show the impact that certain modeling assumptions can have on the prediction of structural response. The main inconsistencies found in the literature were related to the representation of solid temperatures, the convective heat transfer coefficient, and the surface emissivity of steel at the structure-fire interface.

Net heat flux is used as the thermal boundary condition and two different representations of net heat flux are considered in this study which employ different models for heat transfer in the solid. Heat flux is defined as a flow of energy per unit area per unit time. The net heat flux to a surface can be predicted by the incident radiative heat flux and the gas temperature, the adiabatic surface temperature [44] (AST), or directly in the CFD simulation. The first two methods listed

use the FE conduction model to determine solid temperature while the final method listed uses the CFD code's solid conduction model. Next, the convective heat transfer coefficient was considered, which is a parameter used to determine the convective heat flux component of the boundary condition. This study considers the heat transfer coefficient as a constant value of 35 W/m^2K (as specified in references [18], [42]) or 9 W/m^2K (as specified in reference [45]) or calculated directly from the CFD analysis (as recommended in reference [46]). In addition, the surface emissivity of steel is explored in this study. Emissivity is the ratio between the radiative heat absorbed by the surface to that absorbed by a blackbody, and it is related to determining the radiative heat flux to a solid. Eurocode [18] suggests using a value of 0.7 for calculations of steel exposed to fire and the value of 0.9 has been used for the emissivity of steel when considering localized fires [43]. Furthermore, The ASCE Manuals and Reports on Engineering Practice No. 138, Structural Fire Engineering [47] reports the emissivity of steel at room temperature to be between 0.2 and 0.9 and recommends a value towards the higher end of the provided range when modeling unprotected steel under fire exposure as a conservative measure because soot may adhere to the surface of the steel.

This study considers the various methods and parameters described above in two localized fire scenarios. The first scenario considers a square hollow section (SHS) column subjected to an adjacent burner fire, which has been tested experimentally [48]. The second scenario consists of a steel I-beam subjected to a pool fire at mid-span, which was experimentally tested at the University of Edinburgh [49].

3.2 Validation Studies

3.2.1 Case 1 – Experiment by Kamikawa et al. [48]

Case 1 is modeled after an experiment conducted by Kamikawa et al. [48]. It consisted of an SHS column subjected to an adjacent burner fire. Specifically, the fire source was a square diffusion burner (dimensions: 0.3m x 0.3m x 0.25m tall) located beside the base of the column. The fuel source was propane, and the heat release rate (HRR) was kept constant at 52.5 kW. The column section tested was STKR400, with dimensions, 0.1m x 0.1m x 1.6m and a 3.2mm wall thickness. The column was only restrained at the base where a fixed boundary condition was imposed. The experiment conducted by Kamikawa et al. [48] included 4 different test cases, the case studied here is referred to as case 1 in their work. This experiment was conducted to study the thermal and mechanical response of the column as a result of thermal expansion and no mechanical load placed on the column. Figure 3.2 displays the experimental setup [48]. The set-up depicts the column within a load bearing frame and an oil jack set above the specimen. The oil jack was controlled by an electric hydraulic pump. Installed between the specimen and the jack were a load cell for axial force (although no axial force was applied in the case studied here), a cylindrical sliding bearing and a cruciform steel plate for vertical displacement measurements. Partition walls for smoke exhaust were placed around the experimental apparatus [48].

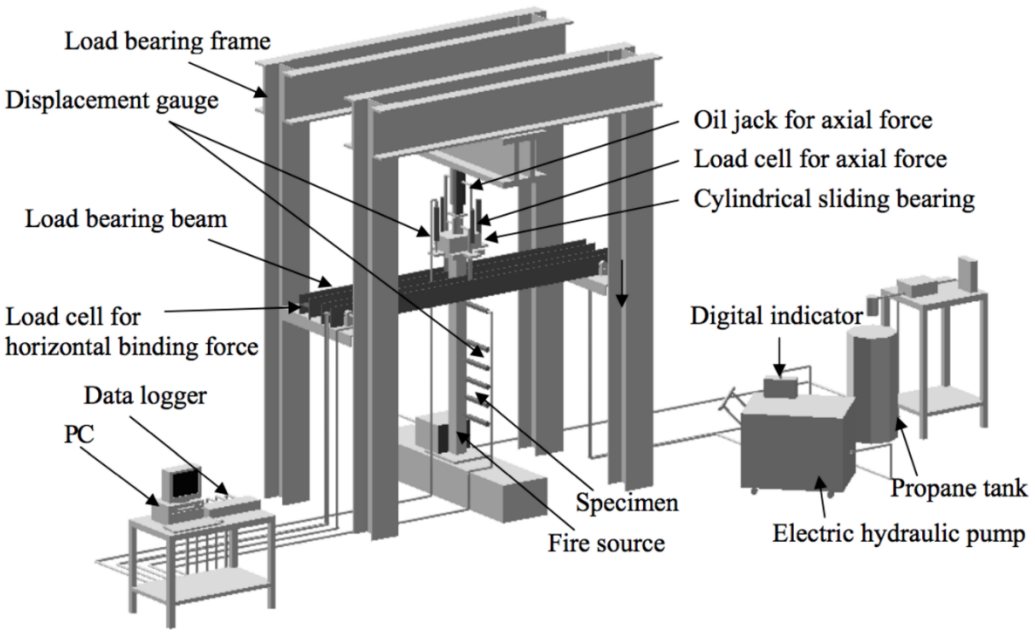

Figure 3.2 - Experimental setup in Kamikawa et al. [48]

3.2.2 Case 2 – Experiment by University of Edinburgh [49]

Case 2 is modeled after an experiment performed at the University of Edinburgh [49]. It consisted of a steel I-beam subjected to a pool fire at mid-span. The fire source was a 0.4 m square heptane pool fire with a mass of 1.6 kg. The fire was located one meter below the beam at mid-span. The I-beam used in the test was a simply supported 203x133x30 UB section. The measured mass loss rate of the heptane fuel was 0.0203 kg/m^{2}s. This experiment was conducted as part of a round-robin study to examine the consistency of different modeling approaches to determine the thermal response of a beam subjected to a pool fire. There was no mechanical load placed on the beam in this study. The test set-up [49] is shown in Figure 3.3. The set-up depicts the beam being simply supported by two metal stands. The fire is located under the beam at mid-span, and the fire source was placed in a water bath.

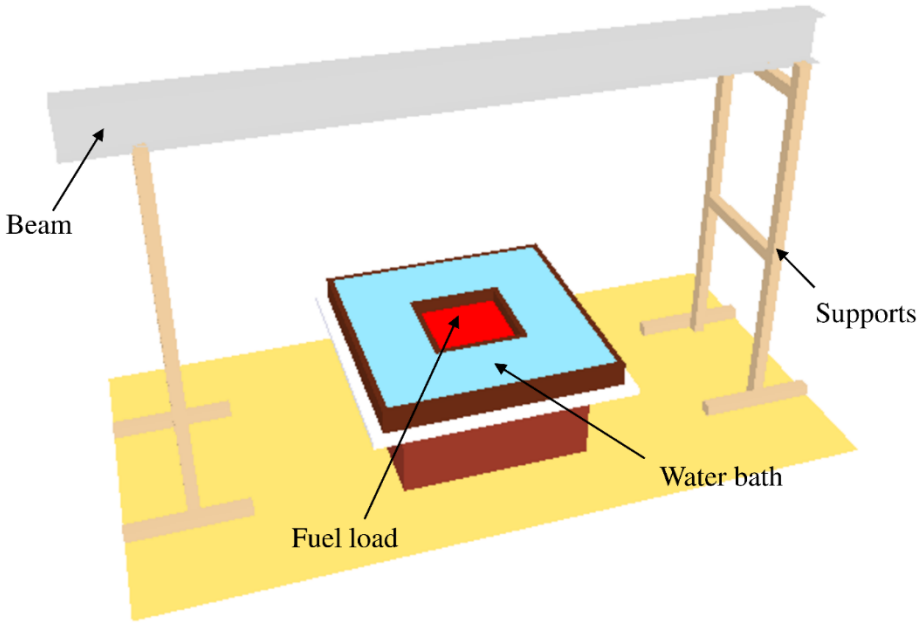

Figure 3.3 - Experimental setup in Higginson et al. [49]

3.3 Methodology and Numerical Methods

This study uses a one-way (or weak) coupling algorithm to couple the CFD-FE analyses, illustrated in Figure 3.4. In a one-way coupling scheme, the CFD and FE analyses are run separately, and information from the CFD simulation, namely temperature and heat flux data, is transferred to the FE model, which determines the thermal and mechanical response of the structure. There is no feedback from the FE analysis to the CFD code. Broadly, this means that characteristics captured in the FE analysis such as displacements and other changes in geometry are not considered in the CFD simulation. Spatial [50] and temporal [51] homogenization algorithms were used to overcome differences in the space and time scale used in the CFD and FE analyses.

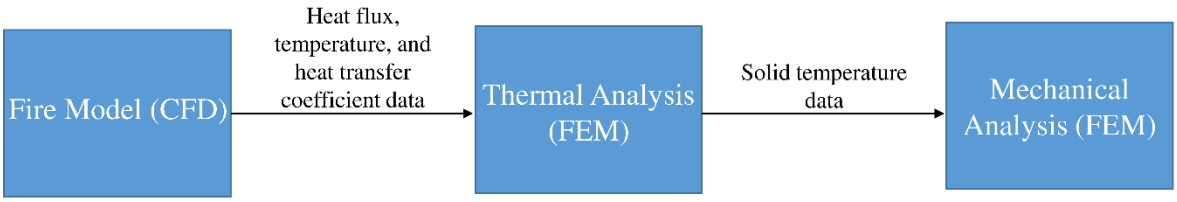

Figure 3.4 - One way (weak) coupling scheme

The CFD code used to model the localized fire in this study was Fire Dynamics Simulator (FDS) developed by NIST. Specifically, version 6.6.0 was used for the analyses presented in this report. FDS numerically solves a form of the Navier-Stokes equation that can be used for "low-speed, thermally-driven flow". Turbulence is modeled using Large Eddy Simulation (LES). The combustion model uses a single step, mixing-controlled chemical reaction that uses three lumped species (i.e., air, fuel and products) and radiative heat transfer is solved for using the radiation transport equation for grey gas [52][53].

Temperature-dependent material properties were used for the steel members in both the CFD and FE models. The temperature-dependent Eurocode [18]models for conductivity and specific heat were input into both the CFD and FE models, and the stress-strain model and thermal expansion model from Eurocode [18] were used in the FE analysis. The elastic modulus used was 202,000 MPa, and the yield strength used was 404 MPa.

The spatial mesh for the CFD code was determined based on the equation for the characteristic diameter of a plume [52].

$$D^* = \left(\frac{\dot{Q}}{p_\infty c_p T_\infty \sqrt{g}}\right)^{\frac{2}{5}} \qquad [3.1]$$

where D^* = characteristic diameter of the plume (m), $\dot{Q}$ = total heat release rate (kW), p_∞ = ambient air density (kg/m^3), c_p = ambient specific heat of air (kJ/kg-K), T_∞ = ambient air temperature (K), and g = acceleration of gravity (m/s^2).

The characteristic diameter of the plume can then be used to determine mesh size using the following relation.

$$R^* = \frac{dx}{D^*} \quad [3.2]$$

where R^* = spatial resolution and dx = mesh size (m).

Using Eqns. 3.1 and 3.2, a mesh size of 0.025 m was found to be sufficient for both case 1 and case 2 (assuming R* = 1/12) as recommended [43]. Additionally, a CFD mesh sensitivity study was carried out for case 1. Because of the similar nature of case 1 and case 2 and that the same mesh size was used, an additional mesh sensitivity analysis was not carried out for case 2. The results of the CFD mesh sensitivity study are presented in Figure 3.5**.** A mesh size of dx = 0.025 m and dx = 0.0125 m were tested and compared. Figure 3.5a presents the thermal results recorded on the center of the front side of the column (closest to the fire) measured 400 mm from the base. Figure 3.5b presents the displacement results recorded on the center of the front side of the column (closest to the fire) measured 1440 mm from the base. The refined CFD mesh (dx = 0.0125 m) predicted higher temperatures as seen in Figure 3.5a and larger displacements as seen in Figure 3.5b. In Figure 3.5a the maximum difference in predicted temperature between the original mesh (dx = 0.025 m) and the refined mesh (dx = 0.0125 m) is less than 10%. In Figure 3.5b the maximum difference in predicted displacement between the original mesh (dx = 0.025 m) and the refined mesh (dx = 0.0125 m) is approximately 14%. These results confirm that refining the CFD mesh does not notably impact the results and does not justify the significant increase in computational expense that would be required.

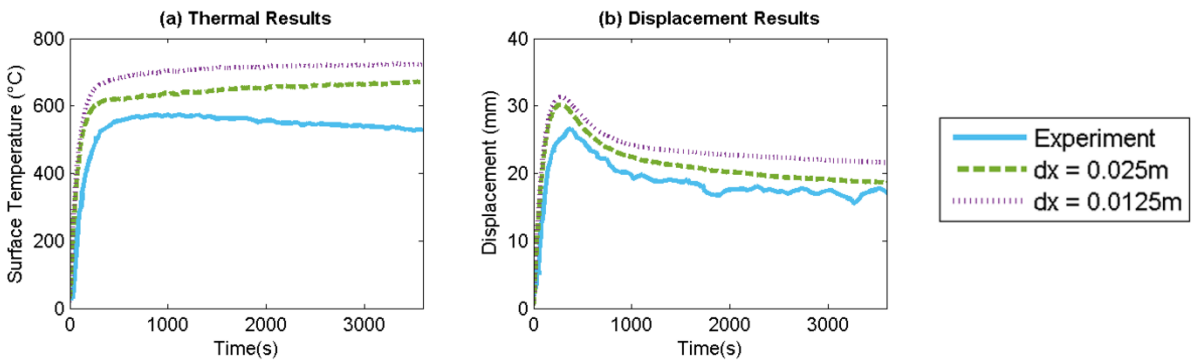

Figure 3.5 - Computational fluid dynamics mesh study

The CFD computational domain used in case 1 was 0.75 m x 0.45 m x 1.8 m and the computational domain used in case 2 was 3.0 m x 1.5 m x 2.0 m. The edges of the computational domain were modeled as 'open vents' in FDS, meaning a passive opening to the outside where ambient conditions exist [52]. It is important to the validity of CFD simulations that the open vents are modeled far enough away from the regions of interest as to not disrupt flow patterns. To validate the choice of the domain size used in this study, additional CFD analyses were run for case 1 and case 2 where the computational domain was extended by 0.5 m in five directions (+x, -x, +y, -y and +z) and compared to the original smaller domain size. The domain size of the extended boundary for case 1 was 1.75 m x 1.45 m x 2.3 m and the extended domain size for case 2 was 4.0 m x 2.5 m x 2.5 m. The results of the analysis of domain size are presented in Figure 3.6. Figure 3.6a presents the thermal results for case 1 recorded at the center of the front face of the column (closest to the fire) and 400 mm from the base. Figure 3.6b presents the thermal results for case 2, recorded at mid-span and mid-web of the beam. The figures show that increasing the computational domain does not significantly impact the results of this study.

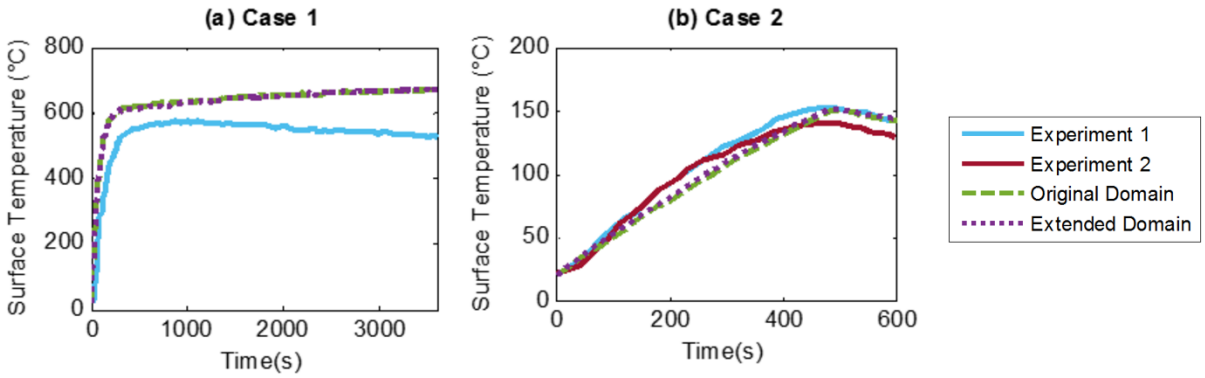

Figure 3.6 - CFD computational domain comparison

In this study, the relevant CFD data was output at every computational volume in the CFD code that contained a structural surface. This was done to completely capture the non-uniformity of the localized fire and create the fullest representation of the CFD fire model one could achieve in FE model. Smokeview images from the CFD analyses are shown for case 1 (Figure 3.7a) and case 2 (Figure 3.7b).

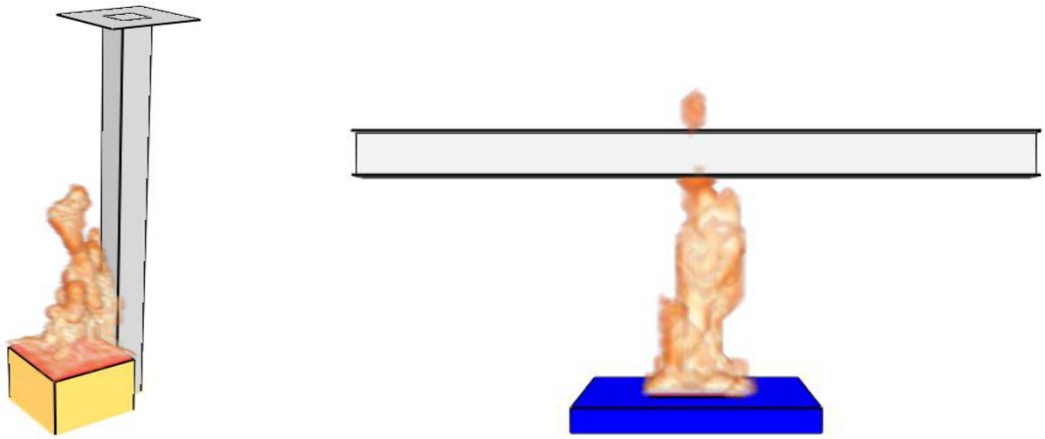

Figure 3.7 - CFD simulation of case 1 and 2, respectively

Finite element models were created for both cases using Abaqus. For case 1, a coupled temperature-displacement analysis was performed using the S4T element type. The S4T coupled temperature-displacement element is a 4-node general-purpose shell element with finite membrane strains and bilinear temperature in the shell surface. This element was chosen for this analysis

because it can be used in a coupled temperature-displacement model and the thin walls of the column could be properly modeled with a shell element. A mesh size of 0.01 m was used along the height and width of the column. For case 2, a heat transfer analysis was performed using the DS4 element type. The DS4 heat transfer element is a 4-node quadrilateral shell element. This element was chosen for this analysis because it can be used in a heat transfer model and the thin web and flange of the beam could be properly modeled with a shell element. A mesh size of 0.01 m was used along the height and length of the beam.

A FE mesh sensitivity study was conducted for case 1. Again, because of the similar nature of case 1 and case 2, and that the same element size was used for both cases, an additional mesh sensitivity study was not conducted for case 2. The results of the FE mesh sensitivity study are presented in Figure 3.8. An element size of dx = 0.01 m and dx = 0.005 m were tested and compared. Figure 3.8a presents the thermal results in the center of the front side of the column (closest to the fire) measured 400 mm from the base. Figure 3.8b presents the displacement results in the center of the front side of the column (closest to the fire) measured 1440 mm from the base. The figures show that reducing the element size does not significantly impact the results of this study.

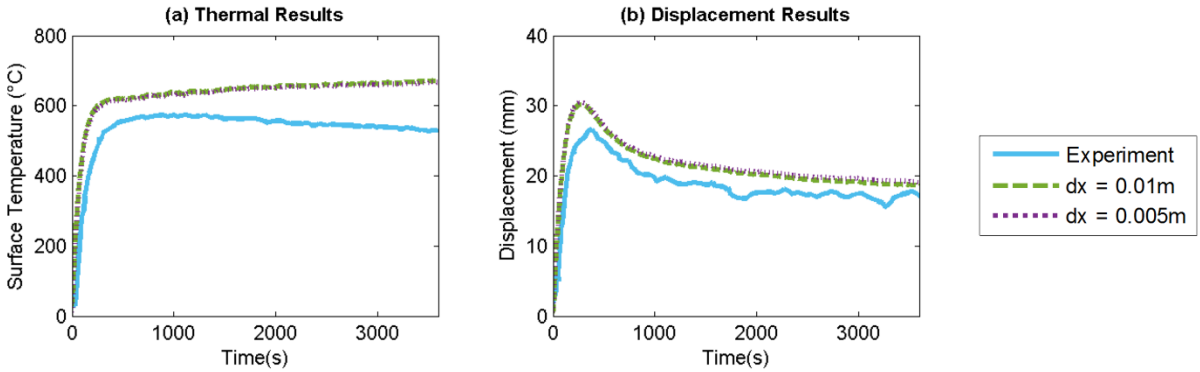

Figure 3.8 - Finite element mesh sensitivity study

In the mechanical model for case 1, the base of the column was fixed, and no mechanical loads were applied. For case 2, only a thermal analysis was performed. The user-subroutine DFLUX was used to apply the distributed non-uniform fluxes to the FE model. The thermal boundary conditions used for both cases are discussed in detail in the following sections.

3.4 Heat Transfer Principles

In typical structural fire engineering problems, heat is generated by a fire and is transferred to the structural surface through radiation and convection. Radiation refers to thermal energy that travels through space by electromagnetic waves. Convection is heat transfer due to the movement of molecules within a fluid such as air. Radiation and convection are independent terms, and when computing heat transfer to a surface, they must be considered separately [54]. A mixed boundary condition is the most common way to express the boundary condition in structural fire engineering application [44]. Eqn. 3.3 represents the total heat transfer to a surface with independent terms for radiative and convective heat transfer, where $\dot{q}^{"}_{tot}$ is the total net heat flux (W/m^2), $\dot{q}^{"}_{rad}$ is the net radiative heat flux and $\dot{q}^{"}_{con}$ is the convective heat flux [54].

$$\dot{q}^{"}_{tot} = \dot{q}^{"}_{rad} + \dot{q}^{"}_{conv} \quad [3.3]$$

Eqn. 3.4 defines the net radiation, where $\dot{q}^{"}_{abs}$ is the absorbed radiant heat (W/m^2) and $\dot{q}^{"}_{emi}$ is the emitted radiant heat (W/m^2).

$$\dot{q}^{"}_{rad} = \dot{q}^{"}_{abs} - \dot{q}^{"}_{emi} \quad [3.4]$$

Eqn. 3.5 defines the absorbed radiant heat where α is the absorptivity, G is the irradiation, ε is the surface emissivity, σ is the Stefan-Boltzmann constant (W/m^{2}K^4), T_r is the radiation temperature (K) and $\dot{q}^{"}_{inc}$ is the incident radiation (W/m^2). The radiation temperature is the equilibrium temperature that an object will obtain if subjected to only constant radiation (no

convection or conduction) [54]. Note that Eqn. 3.5 only holds true if $\alpha = \varepsilon$, which is true for a gray surface. All structural surfaces in this study were assumed to be gray surfaces, which is a standard assumption in the structural fire engineering field. A gray surface is a special case for when radiation exchange occurs between a small surface and a much larger surface (which is at a constant temperature) that completely surrounds the smaller surface. The surroundings could be a furnace or the walls of a room where the temperature of the surroundings are not equal to the temperature of the surface [55]. This equation shows that the absorbed radiation is dependent on the incident radiation [54].

$$\dot{q}''_{abs} = \alpha G = \varepsilon G = \varepsilon\sigma T_r^4 \equiv \varepsilon \dot{q}''_{inc} \quad [3.5]$$

Eqn. 3.6 defines emitted radiation where T_s is surface temperature (K). This equation shows that emitted radiation is governed by the surface temperature [54].

$$\dot{q}''_{emi} = \varepsilon\sigma T_s^4 \quad [3.6]$$

Eqn. 3.7 defines the convective heat transfer by convection, where h is the heat transfer coefficient (W/m^2-K) and T_g is gas temperature (K). This relationship shows that convective heat transfer is controlled by the temperature difference between gas temperature and surface temperature [52].

$$\dot{q}''_{conv} = h(T_g - T_s) \quad [3.7]$$

Eqns. 3.3-3.7 can be combined to create Eqn. 3.8, which represents total heat transfer or net heat flux to a surface [54].

$$\dot{q}''_{tot} = \varepsilon\left(\dot{q}''_{inc} - \sigma T_s^4\right) + h(T_g - T_s) \quad [3.8]$$

The adiabatic surface temperature (AST) is the temperature of a surface where heat is not absorbed or emitted, and it is a weighted average of the radiation temperature and the gas

temperature [44]. The weighting is dependent on the surface emissivity and the heat transfer coefficent. AST will be closer the the gas temperature for a high heat transfer coefficient and the AST will be closer to the radiation temperature for a low heat transfer coefficent [54]. AST is independent of surface temperature [44]. Eqn. 3.9 presents the defining relation for adiabatic surface temperature, where T_{AST} is the adiabatic surface temperature (K).

$$\varepsilon\left(\dot{q}''_{inc} - \sigma T_{AST}^4\right) + h\left(T_g - T_{AST}\right) = 0 \qquad [3.9]$$

Eqn. 3.10 represents the total heat transfer to a surface based on adiabatic surface temperature. The full derivation for this equation can be found in the literature [54].

$$\dot{q}''_{tot} = \varepsilon\sigma(T_{AST}^4 - T_s^4) + h(T_{AST} - T_s) \qquad [3.10]$$

Note that Eqns. 3.8 and 3.10 are theoretically equivalent to each other. Care should be taken when comparing Eqns. 3.8 and 3.10 using output data from FDS. These equations are equivalent to each other when the data used is measured at a specific point in time. FDS by default outputs time-averaged data.

3.5 Analysis of Solid Conduction Models

3.5.1 Solid Temperature Determined by FE analysis

Heat flux predicted by incident radiative heat flux and gas temperature is presented in Eqn. 3.8 and is the most traditional representation. It is also the most computationally expensive method considered in this study; it requires at least two spatially and temporally variable parameters from the CFD simulation to be transferred to the FE model, namely, the incident radiative heat flux (FDS DEVC = “Incident Heat Flux”) and gas temperature (FDS DEVC = “Gas Temperature”). To reduce the computational expense of determining the net heat flux, Eqn. 3.10 was developed [44] to calculate the net heat flux based on adiabatic surface temperature (AST). This method of

representing the net heat flux is computationally efficient because it only requires one variable parameter from the CFD code to be transferred to the FE analysis, in this case, adiabatic surface temperature (FDS DEVC = "Adiabatic Surface Temperature"). Note that because Eqns. 3.8 and 3.10 are theoretically equal, it follows that the results from calculating heat flux based on incident radiative heat flux and gas temperature or adiabatic surface temperature are also equal. This method uses the FE prediction of solid temperature (T_s) in Eqns. 3.8 and 3.10. This solid temperature model will be referred to as FEM in the results section of this paper.

3.5.2 Solid Temperature Determined by FDS

The heat flux predicted by the CFD code is also a computationally efficient approach for determining the net heat flux to a surface; at most, it relies on the inclusion of only one spatially and temporally varying parameter, net heat flux (FDS DEVC = "Net Heat Flux"). The CFD code used in this study, FDS [52], calculates the total net heat flux using Eqn. 3.8. It should be noted that this approach is not used in practice as it depends on the CFD simulation to predict surface temperature (T_s) which FDS was not designed to do. This heat flux (HF) assumption will be referred to as CFD in the results section of this paper.

3.6 Analysis of Heat Transfer Coefficient

The heat transfer coefficient is an important parameter used to calculate the convective heat flux as shown in Eqn. 3.7. As previously discussed, the literature recommends a variety of values for the heat transfer coefficient.

3.6.1 Heat Transfer Coefficient as 9 W/m^{2}K

This value is recommended for use by one study [45] for calculating the boundary condition of a coupled CFD-FE model of an isolated structural member subjected to a localized

fire. This approach for representing the heat transfer coefficient is computationally efficient because it is a constant value.

3.6.2 Heat Transfer Coefficient as 35 W/m^{2}K

The value of 35 W/m^{2}K is recommended by Eurocode [18] for use when a more detailed approach is unavailable. It is implemented by one study [42] for modeling a vehicle fire in a parking structure. This method is also computationally efficient because it employs a constant value.

3.6.3 Spatially and Temporally Varying Heat Transfer Coefficient

This approach requires using a non-constant value for the heat transfer coefficient calculated by the CFD analysis. The CFD code used in this study, FDS, determines the heat transfer coefficient based on the equation as follows.

$$h = \max\left[\mathrm{C}\left|T_g - T_s\right|^{\frac{1}{3}}, k\,\frac{k}{L}Nu\right] \qquad [3.11]$$

Where C is the empirical coefficient for natural convection, k is conductivity (W/m-K), L is characteristic lengh (m) and Nu is the Nusselt number [52].

Silva et al. [46] recommends the use of a variable heat transfer coefficient for a coupled CFD-FE model. Furthermore, Wickstrom [44] discourages the use of a constant heat transfer coefficent in fire protection engineering because the heat transfer coefficient can be highly dependent on gas temperature and surface temperature, which can vary significantly, especially localized fire scenarios. This method is the most computionally expensive approach to modeling the heat transfer coefficent because it requires the inclusion of an additional spatially and temporally variable parameter from the CFD simultaion.

3.7 Analysis of Surface Emissivity

The emissivity of a surface is defined as the ratio between the radiative heat absorbed by a surface to that absorbed by a blackbody surface. A blackbody is an idealized surface that absorbs all incident radiation. Emissivity is related to the calculation of the net radiative heat flux as shown in Eqns. 3.5 and 3.6. Both methods described below recommend using a constant value for the surface emissivity, therefore they both have the same computational expense.

3.7.1 Emissivity of Steel as 0.7

The Eurocode [18] suggests using a value of 0.7 for traditional calculations of steel exposed to fire.

3.7.2 Emissivity of Steel as 0.9

A value of 0.9 as the emissivity of steel is used by one study [43] for a CFD-FE model of a column subjected to a localized fire.

3.8 Results and Discussion

Figure 3.9a and Figure 3.9b visually display where the temperature measurements were recorded in relation to the fire for the following results for case 1 and 2 respectively.

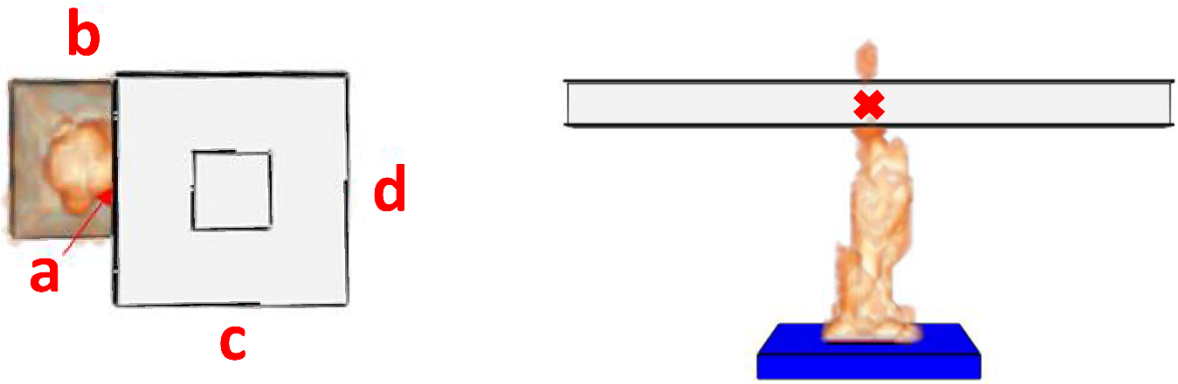

Figure 3.9 - Temperature measurement locations for case 1 and 2, respectively

3.8.1 Discussion of Solid Temperature Models

Eqns. 3.8 and 3.10 are theoretically equivalent to each other, and therefore the results from utilizing net heat flux calculated from incident radiative heat flux and gas temperature will be the same as the results from utilizing net heat flux calculated from adiabatic surface temperature. The results from both heat flux assumptions will be labeled as FEM in the results because they both use the FE prediction of surface temperature (T_s). The results when utilizing net heat flux calculated from the CFD code will be different because it relies on the CFD prediction of surface temperature (T_s). FDS, the CFD code used in this study, employs only a 1D conduction model, which will result in errors for the case of large thermal gradients that occur due to localized fires. To demonstrate the importance of using a 3D conduction model for coupled CFD-FE localized fire models, Figure 3.10a and Figure 3.10b display the spatially varying surface temperatures that occur through the center of the front surface of the column (closest to the fire) in case 1 at 3600 s (end of simulation time) and the center of the bottom flange of the beam in case 2 at 600 s (end of simulation time), respectively. Figure 3.10a shows that the front surface temperature of the column varies from approximately 466°C at the top of the column to over 680°C at 0.45 m measured from the base, which is approximately 0.2 m above the burner. Figure 4.10b shows the surface temperatures on the bottom flange of the beam vary from approximately 25°C at both ends to over 200°C in the center of the beam, which is located directly over the pool fire. Both cases demonstrate a range of temperatures of approximately 200°C on a single surface.

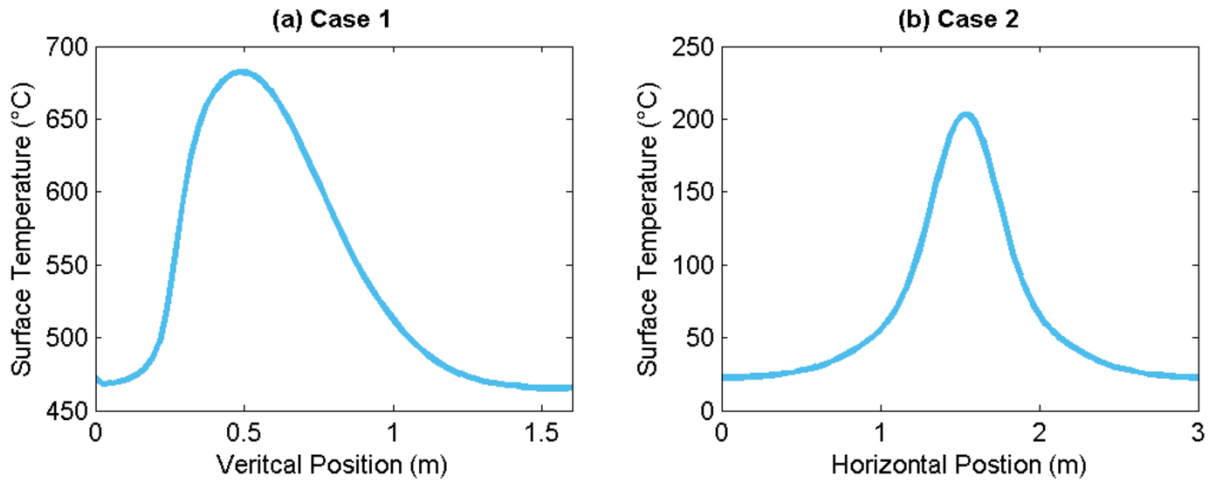

Figure 3.10 - Spatially varying temperature analysis

Figure 3.11 displays the temperature results for varying solid temperature models in case 1. Figure 3.11a displays the surface temperature results on the front surface (facing the fire) at 0.4 m, Figure 3.11b shows the temperature results for the corner of the column, in between the front and side surface, at 0.4 m. Figure 3.11c and Figure 3.11d display the temperature results for the side and back surface of the column, respectively, at 0.6 m. On the cross-section level, measurements for temperature on the front, side and back surface were recorded from the center of the respective column face. A surface emissivity of 0.9 and a variable heat transfer coefficient predicted by the CFD code were used for both cases in this section.

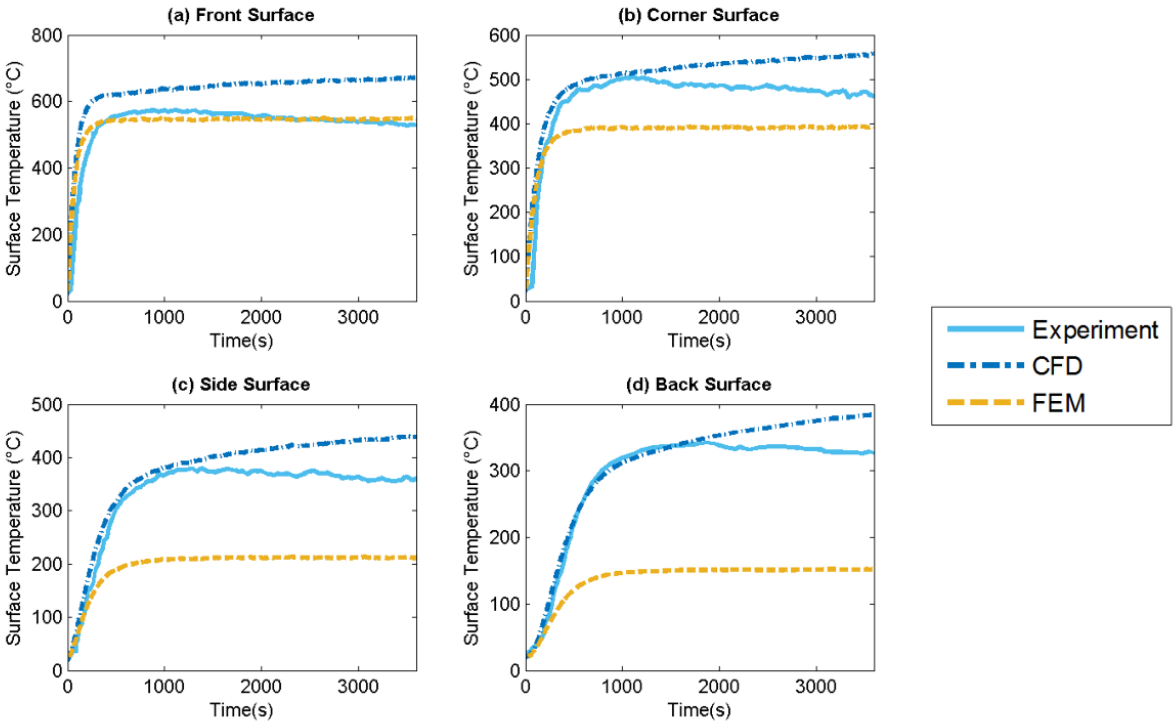

Figure 3.11 - Thermal results for case 1 based on varying solid temperature models

Figure 3.12 displays the surface temperature results for case 2 considering varying solid temperature predictions. Temperatures were recorded at mid-span and mid-web of the beam.

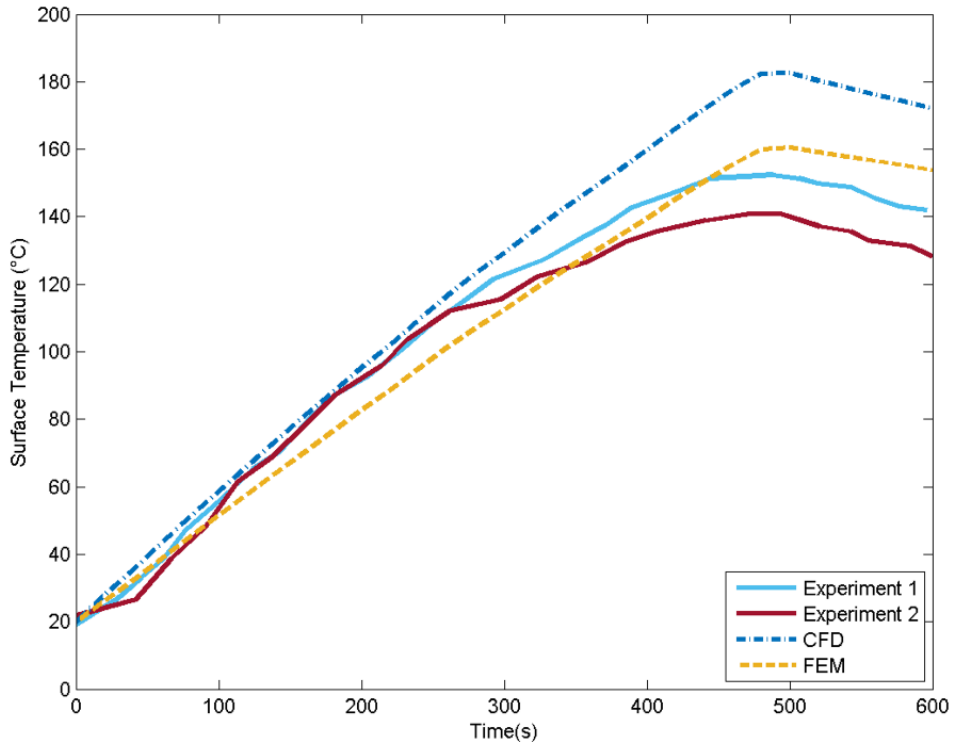

Figure 3.12 - Thermal results for case 2 based on varying solid temperature models

Figure 3.13 displays the lateral displacement results along the length of the column in case 1 considering the varying solid temperature predictions. Figures 3.13a, 3.13b, 3.13c, and 3.13d show the displacement results recorded at 1.44 m, 1.225 m, 0.925 m, and 0.775 m respectively along height of the column, measured from the base. On the cross-section level, measurements for displacement were recorded in the center of the front face of the column.

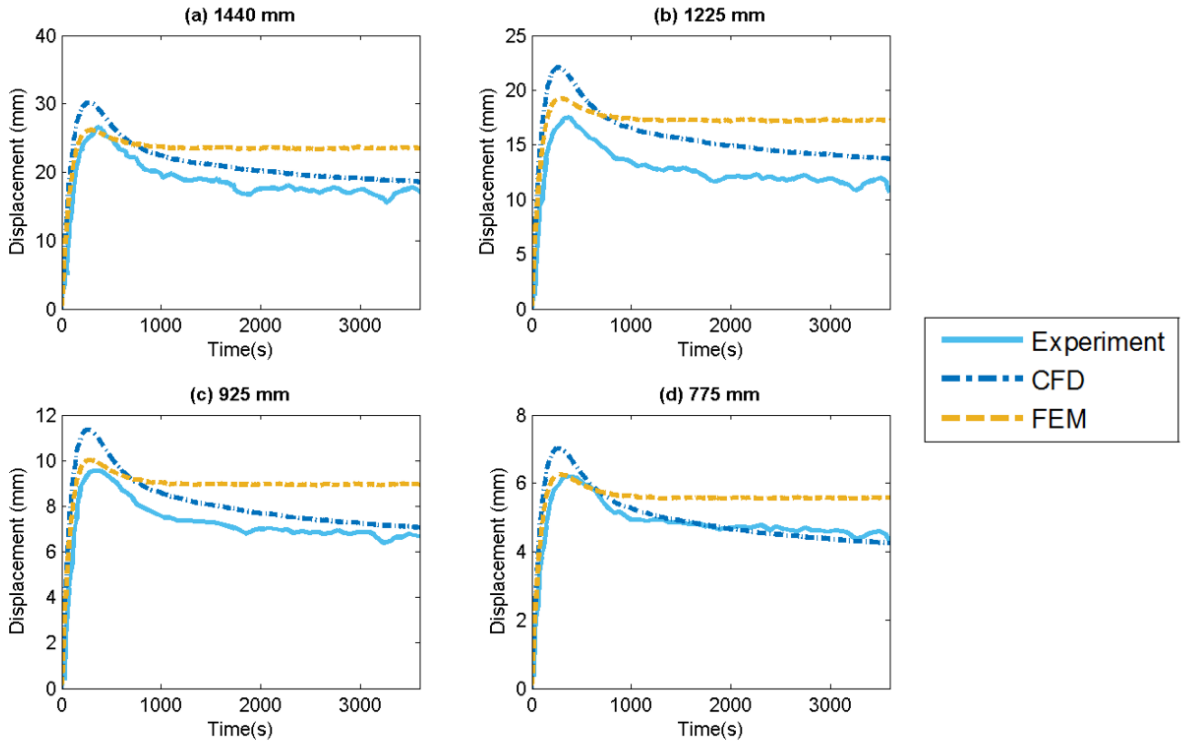

Figure 3.13 - Displacement results for case 1 based on varying solid temperature models

Generally, the thermal results presented in Figure 3.11 and Figure 3.12 demonstrate that using the CFD prediction of solid temperatures to calculate heat flux resulted in higher predicted temperatures than using the FEM prediction of solid temperatures. The thermal results for case 1 presented in Figure 3.11 show that the using the FEM solid temperature model resulted in a more accurate prediction of temperature on the front surface of the column but under-predicted the temperature on surfaces further from the flame. The CFD solid temperature model over-predicted the temperature on the front surface of the column, but more accurately predicted temperatures on all other surfaces of the column. The thermal results for case 2 presented in Figure 3.12 show that using the FEM calculation of solid temperature resulted in a more accurate prediction of surface temperature; the CFD calculation of solid temperature over-predicted the temperature in this case.

Figure 3.13 displays the displacement predictions for case 1. In the beginning of the simulation, the FEM solid temperature model more accurately predicts displacements but as the

simulation progressed, the CFD solid temperature model was a better prediction. At the end of the simulation, the FEM solid temperature model over-predicted the displacements.

The FEM solid temperature model is a more accurate representation of solid temperatures in a localized fire scenario and was able to better predict surface temperatures close to the flame. This model over-predicted the lateral displacements in case 1 but is recommended for use as a conservative measure by this study.

3.8.2 Comparison of Heat Transfer Coefficient

Figure 3.14 displays the temperature results for varying heat transfer coefficients in case 1. Figure 3.14a displays the surface temperature results on the front surface (facing the fire) at 0.4 m. Figure 3.14b shows the temperature results for the corner of the column, in between the front and side surface, at 0.4 m. Figure 3.14c and Figure 3.14d display the temperature results for the side and back surface of the column, respectively, at 0.6 m. On the cross-section level, measurements for temperature on the front, side and back surface were recorded from the center of the respective column face. A surface emissivity of 0.9 and surface temperature predicted by the CFD code were used for both cases in this section.

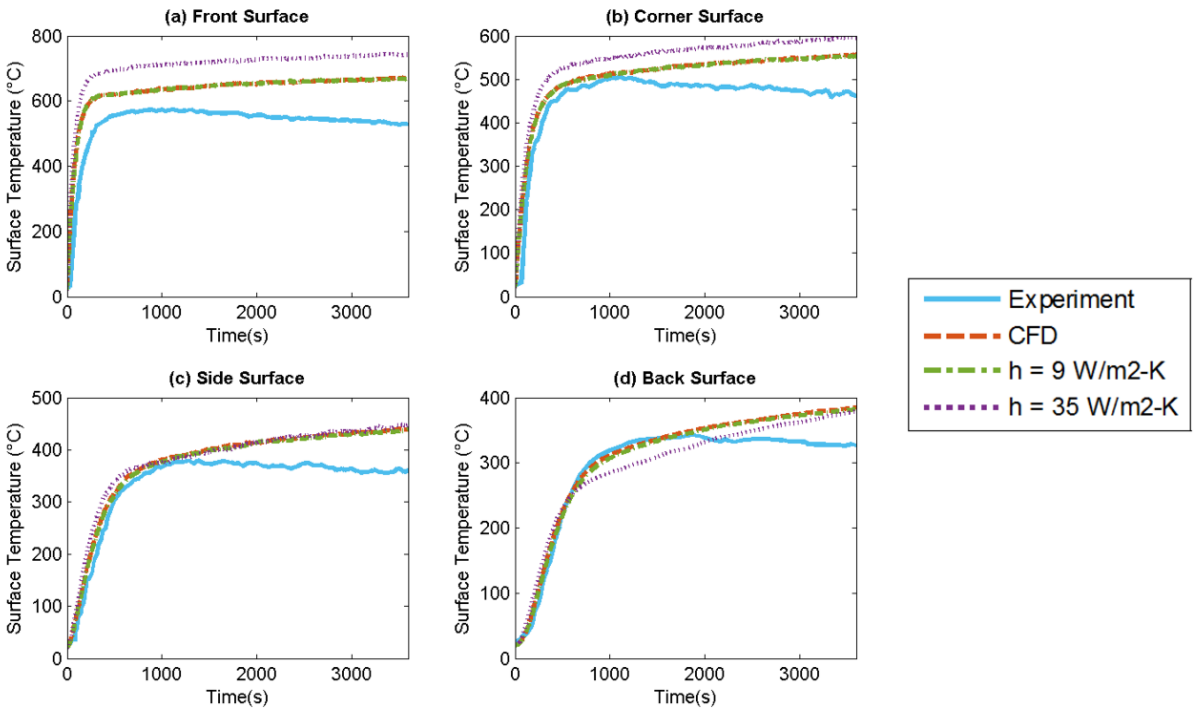

Figure 3.14 - Thermal results for case 1 based on varying heat transfer coefficient (h) assumptions

Figure 3.15 displays the surface temperature results for case 2 considering varying heat transfer coefficient assumptions. Temperatures were recorded at mid-span and mid-web of the beam.

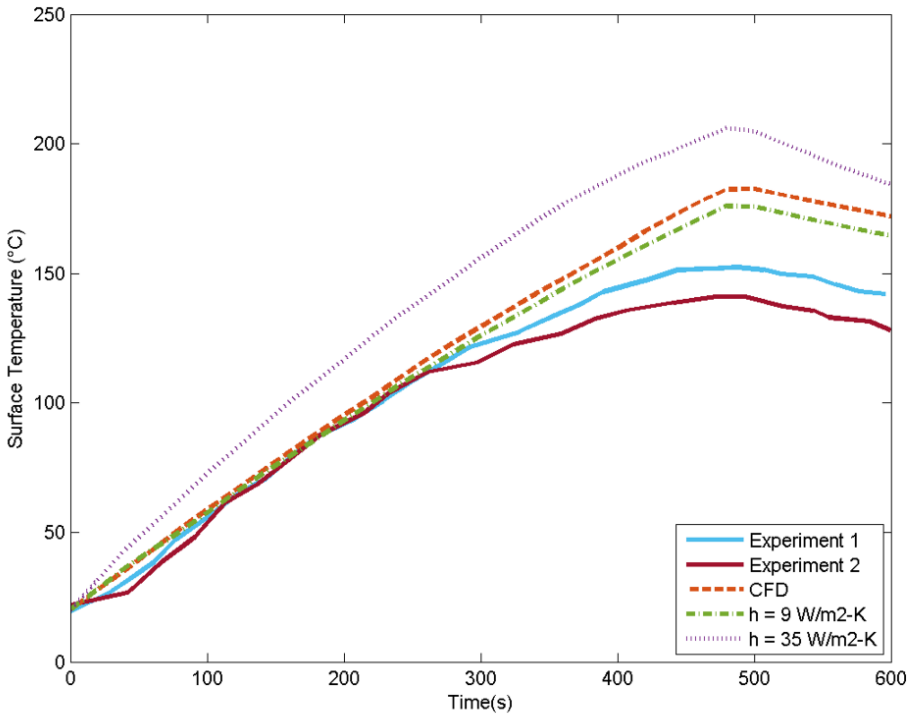

Figure 3.15 - Thermal results for case 2 based on varying heat transfer coefficient (h) assumptions

Figure 3.16 displays the lateral displacement results along the length of the column in case 1 considering the varying heat transfer coefficient assumptions. Figures 3.16a, 3.16b, 3.16c, and 3.16d show the displacement results recorded at 1.44 m, 1.225 m, 0.925 m, and 0.775 m respectively along height of the column, measured from the base. On the cross-section level, measurements for displacement were recorded in the center of the front face of the column.

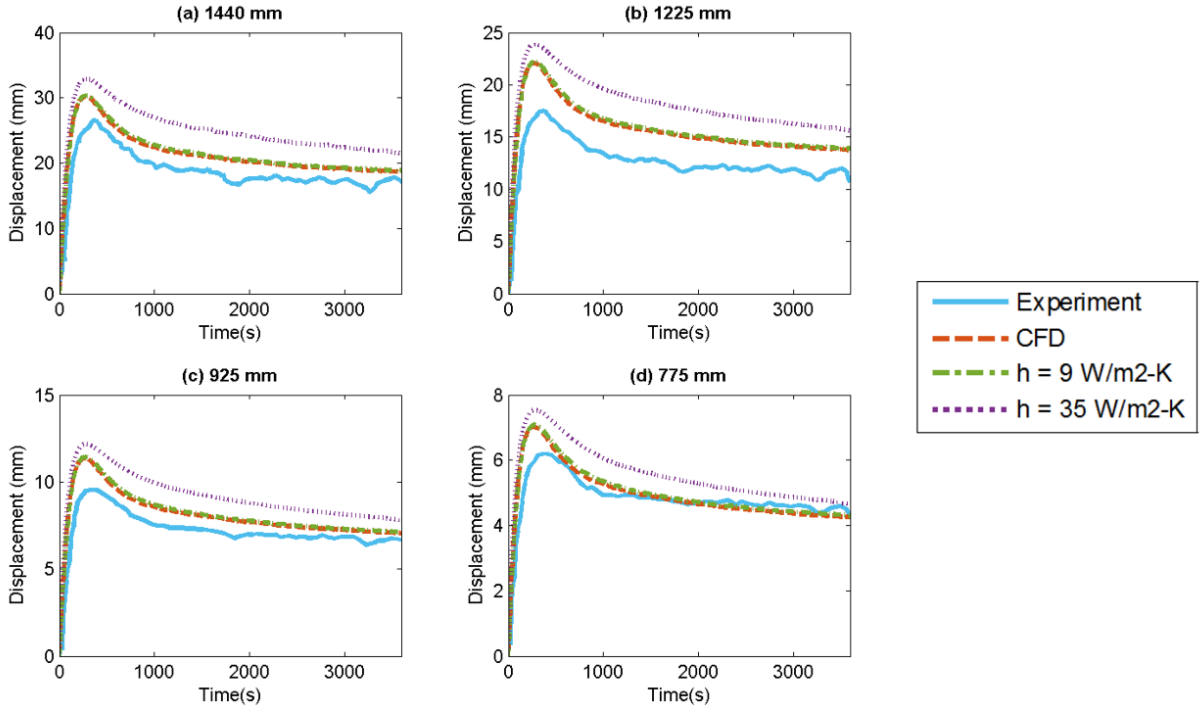

Figure 3.16 - Displacement results for case 1 based on varying heat transfer coefficient (h) assumptions

The thermal results for the different heat transfer coefficient assumptions show that the predicted temperatures can vary significantly based on the employed assumption. A heat transfer coefficient of 35 W/m^{2}K significantly over-predicted the temperatures of the beam in case 2 as seen in Figure 3.15. In case 1, a heat transfer coefficient of 35 W/m^{2}K over-predicted the temperatures on the front and corner surface of the column, accurately predicted the temperatures on the side surface and under-predicted temperatures on the back surface. Temperatures were over-predicted on the front and corner surfaces because these surfaces are closest to the fire where gas temperatures are the highest, so the convective heat transfer to these surfaces are heating the column, and a large heat transfer coefficient over-predicted this behavior. On the back surface, furthest from the fire, the gas temperatures are lower, and the convective heat transfer is working to cool the back surface which resulted in under-predicted temperatures when the convective heat

flux is weighted more heavily by a larger heat transfer coefficient. In case 1, assuming the heat transfer coefficient as equal to 9 W/m^2K resulted in slightly lower column temperatures than assuming a heat transfer coefficient predicted by the CFD code as seen in Figure 3.14. In case 2, there was an opposite effect on the thermal response. The heat transfer coefficient calculated by the CFD code resulted in slightly lower predicted temperatures than the temperatures predicted by a heat transfer coefficient of 9 W/m^2K, which can be seen in Figure 3.15.

The displacement results seen in Figure 3.16 show that a heat transfer coefficient of 9 W/m^2K predicted slightly higher displacements while a variable heat transfer coefficient from the CFD code predicted lower and more accurate displacements. A heat transfer coefficient of 35 W/m^2K significantly over-predicted the displacement results due to the artificially large temperature gradient it predicted within the cross-section of the column.

Figure 3.17a shows the heat transfer coefficient predicted by the CFD code along the height of the column for case 1 at 1600 s (half of the simulation time). Along the front surface of the column there are high levels of non-uniformity predicted, with a minimum heat transfer coefficient of 1.21 W/m^2K and a maximum heat transfer coefficient of 11.65 W/m^2K. Along the back surface of the column, there was non-uniformity as well, but to a smaller degree. The back surface had a minimum heat transfer coefficient of 2.75 W/m^2K and a maximum heat transfer coefficient of 7.93 W/m^2K. Figure 3.17b shows the heat transfer coefficient along the length of the beam predicted by the CFD code for case 2 at 300 s (half the simulation time). Along the bottom flange, high non-uniformity of the heat transfer coefficient can be seen. The minimum predicted heat transfer coefficient, located on the far edge of the beam is 1.44 W/m^2K, and the maximum predicted heat transfer coefficient, located where the flame in impinging on the bottom surface is 9.26 W/m^2K.

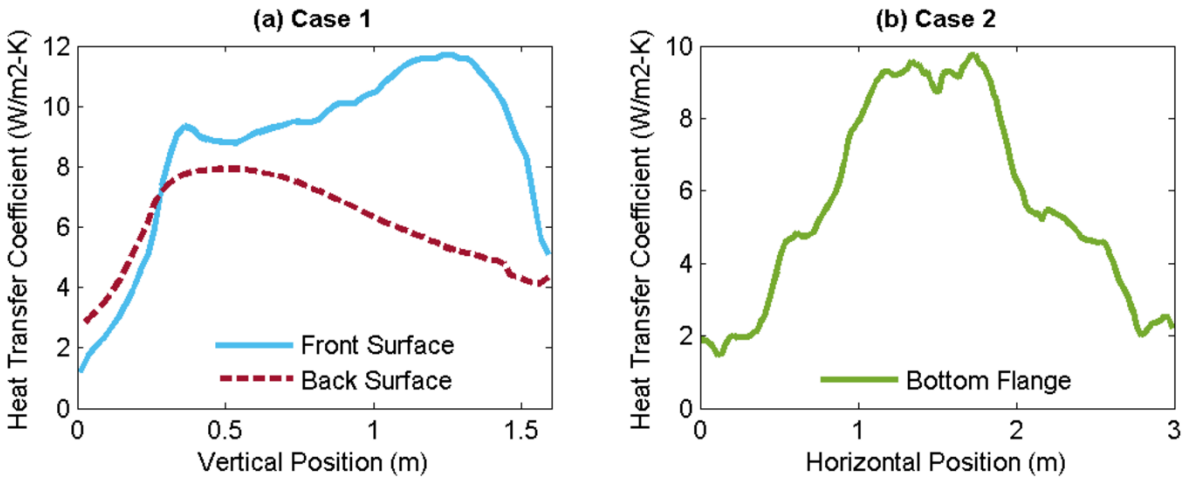

Figure 3.17 - Heat transfer coefficients predicted by the CFD code

These results signify that the heat transfer coefficient for localized fires cannot be accurately represented by a single constant value. Different localized fire scenarios will result in different values for the heat transfer coefficient. There can be significant variation in the heat transfer coefficient over the entire structural member. Therefore, a spatially and temporally variable heat transfer coefficient should be included in coupled CFD-FE analyses when possible. If using a variable heat transfer coefficient is not possible, based on the results of the cases studied here, a constant value of 9 W/m^{2}K should be used when modeling a localized fire on an isolated structural member.

3.8.3 Comparison of Surface Emissivity

Figure 3.18 displays the temperature results for varying emissivity assumptions in case 1. Figure 3.18a displays the surface temperature results on the front surface (facing the fire) at 0.4 m, Figure 3.18b shows the temperature results for the corner of the column, in between the front and side surface, at 0.4 m. Figure 3.18c and Figure 3.18d display the temperature results for the side and back surface of the column at 0.6 m, respectively. On the cross-section level, measurements for temperature on the front, side and back surface were recorded from the center of the respective

column face. A variable heat transfer coefficient and surface temperature predicted by the CFD code were used for both cases in this section.

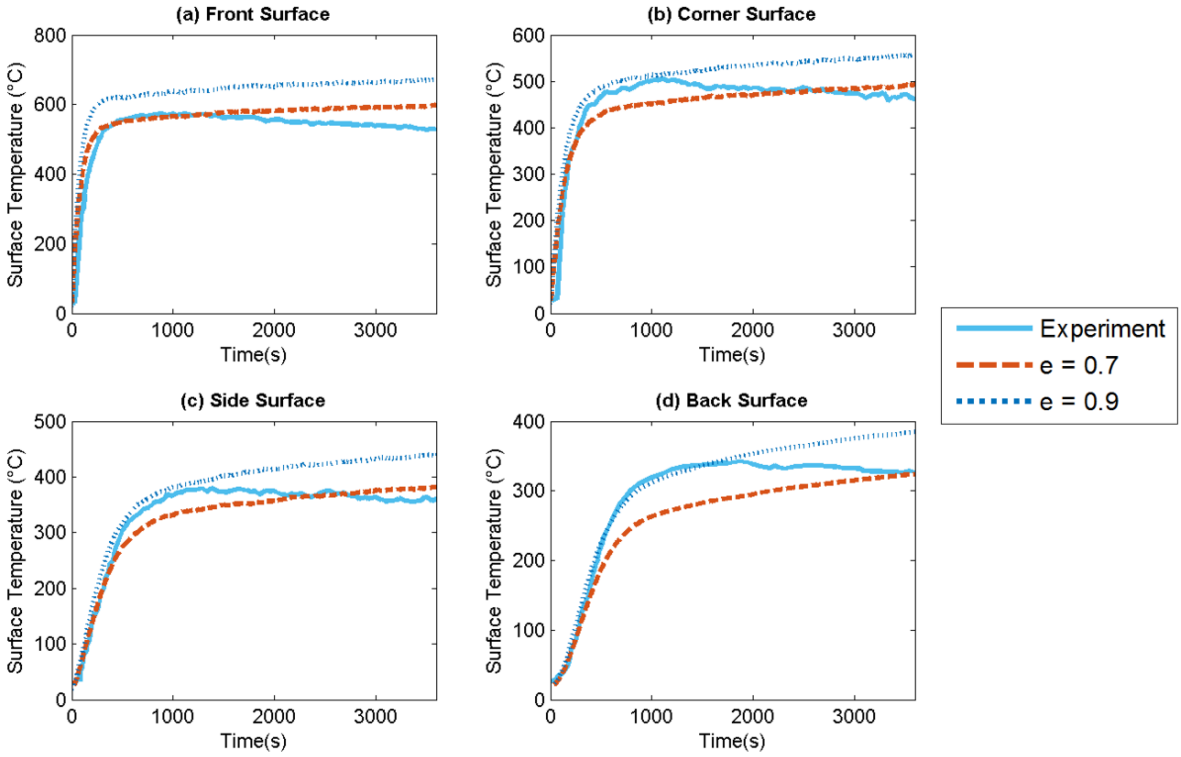

Figure 3.18 - Thermal results for case 1 based on varying emissivity (e) assumptions

Figure 3.19 displays the surface temperature results for case 2 considering varying surface emissivity assumptions. Temperatures were recorded at mid-span and mid-web of the beam.

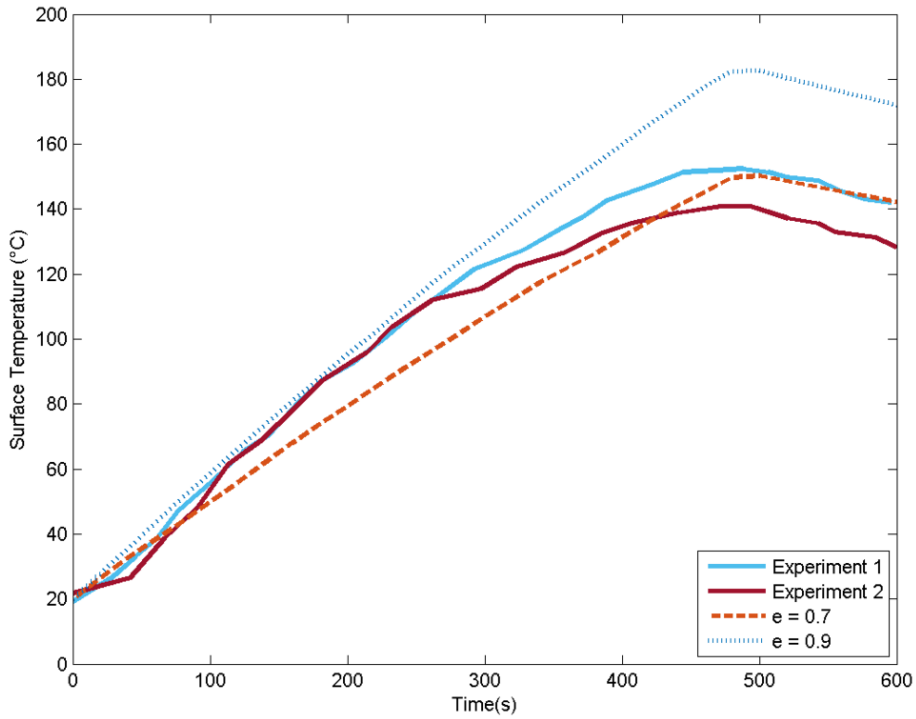

Figure 3.19 - Thermal results for case 2 based on varying emissivity (e) assumptions

Figure 3.20 displays the lateral displacement results along the length of the column in case 1 considering the various emissivity assumptions. Figures 3.20a, 3.20b, 3.20c, and 3.20d show the displacement results recorded at 1.44 m, 1.225 m, 0.925 m, and 0.775 m respectively along height of the column, measured from the base. On the cross-section level, measurements for displacement were recorded in the center of the front face of the column.

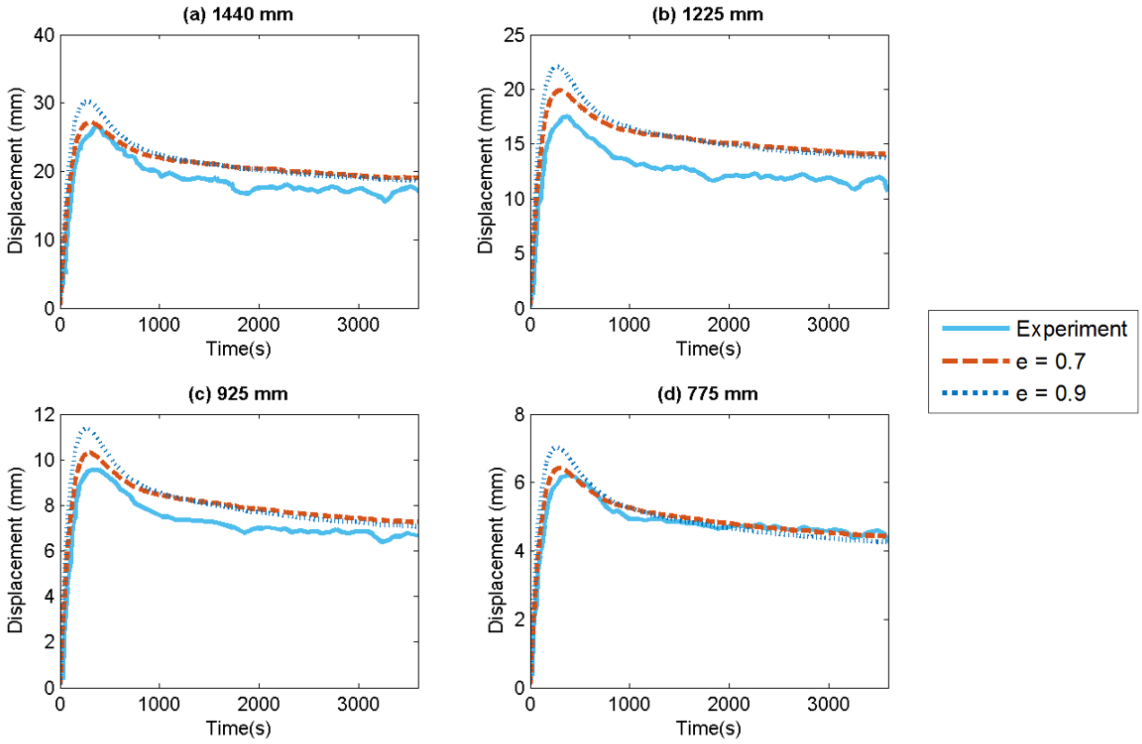

Figure 3.20 - Displacement results for case 1 based on varying emissivity (e) assumptions

In both cases, the higher emissivity value resulted in higher predicted surface temperatures as expected, shown in Figure 3.18 and 3.19. In case 1, an emissivity of 0.7, accurately predicted the temperatures on the front surface of the column but under-predicted temperatures on the back surface of the column, or the surface of the column farthest from the flame. For case 2, where the only recorded temperatures were close to the flame, the emissivity of 0.7 more accurately modeled the temperature.

The displacement results displayed in Figure 3.20 show that the emissivity of 0.7 resulted in similar displacement predictions as using an emissivity of 0.9. In the beginning of the simulation, an emissivity of 0.7 predicted lower displacements than an emissivity of 0.9 but as the simulation progressed an emissivity of 0.7 predicted slightly higher displacement values.

Both emissivity assumptions resulted in similar displacement predictions but an emissivity of 0.9 was able to more accurately predict the temperature of the column. Therefore, in this study, using an emissivity of 0.9 for localized fire scenarios is recommended as a conservative measure.

3.8.4 Comparison of Heat Transfer Coefficient and Surface Emissivity

Figure 3.21 presents a comprehensive representation of various boundary condition assumptions for case 2. Figure 3.21 displays the surface temperature results for case 2 considering varying heat transfer coefficient and surface emissivity assumptions. Temperatures were recorded at mid-span and mid-web of the beam.

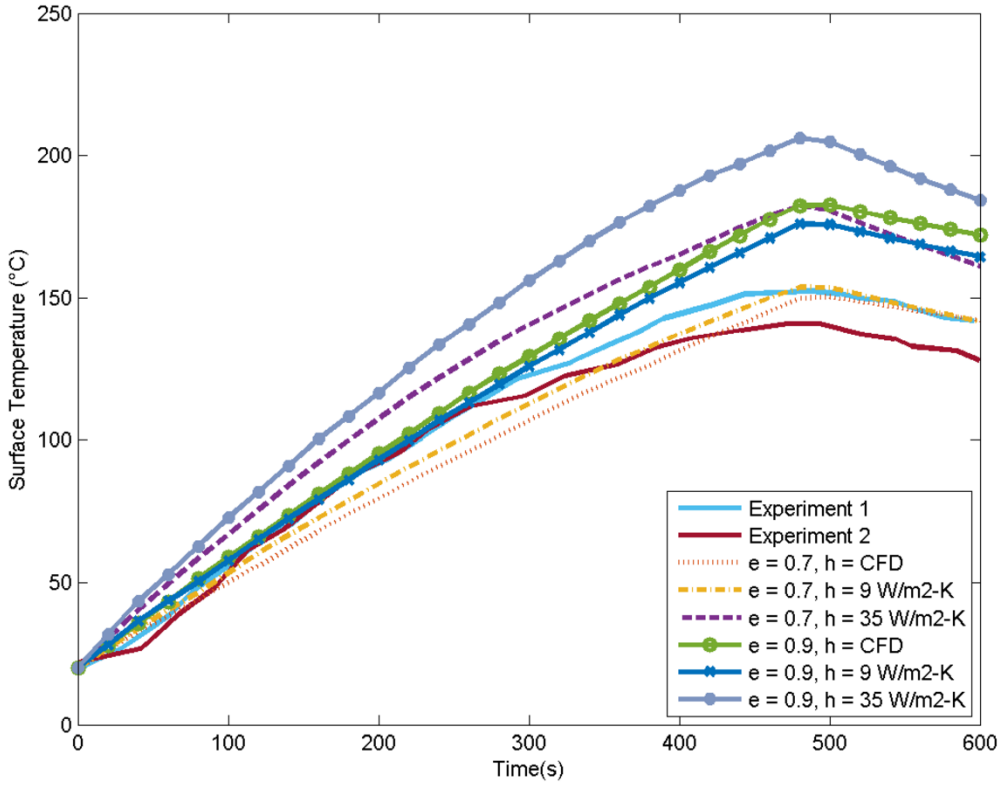

Figure 3.21 - Thermal results for case 2 based on varying heat transfer coefficient (h) and emissivity (e) assumptions

Figure 3.21 shows that an emissivity of 0.7 always predicted lower temperatures than the corresponding emissivity of 0.9 results, which is expected. The results for a heat transfer

coefficient predicted by the CFD code and a heat transfer coefficient equal to 9 W/m^{2}K, resulted in lower predicted temperatures than 35 W/m^{2}K regardless of the emissivity during the heating phase of beam. The heating phase of the beam ends at approximately 492 seconds after the fuel burns out. During the cooling phase, the temperature prediction for an emissivity of 0.7 and a heat transfer coefficient equal to 35 W/m^{2}K cools at a faster rate (due to the increased magnitude of convection) and the simulation ends with this boundary condition assumption resulting in a slightly lower temperature than predicted by assuming an emissivity of 0.9 and a heat transfer coefficient predicted by the CFD code or equal to 9 W/m^{2}K. Overall, a modeling assumption of surface emissivity equal to 0.7 and a heat transfer coefficient predicted by the CFD code resulted in the lowest predicted temperatures while a modeling assumption of surface emissivity equal to 0.9 and a heat transfer coefficient equal to 35 W/m^{2}K resulted in the highest predicted surface temperatures.

3.9 Conclusions

This study considered the effect of varying solid heat transfer models, heat transfer coefficients and surface emissivities on the mechanical and thermal response of structural members subjected to a localized fire modeled using a coupled CFD-FE model. The results are summarized in Table 4.1. The "X" in the tables denotes either the most accurate or computationally efficient choice for each category (solid temperature model, emissivity, etc.). The recommendations made by this study valued accuracy over computational expense. The main conclusions are:

- The use of a net heat flux boundary condition calculated using an FEM prediction of surface temperature.

- The heat transfer coefficient for a localized fire scenario cannot be accurately represented by a constant value. The heat transfer coefficient can vary significantly over the structural member and therefore, when possible, a spatially and temporally varying heat transfer coefficient determined by the CFD code should be used.
- A surface emissivity value of 0.9 should be used for localized fire scenarios of steel structures modeled using a coupled CFD-FE approach.

Table 3.1 Comparison of boundary condition parameters

	BC Assumption	**Accuracy**	**Computational Expense**
Solid Temperature Model	FE solid temperature	X	X
	CFD solid temperature		X
Heat Transfer Coefficient	9 W/m^2-K		X
	CFD	X	
Emissivity	0.7		X
	0.9	X	X

The recommendations presented by this study are limited to one-way coupled CFD-FE analyses of localized fires on an isolated steel structural member. The recommendations from this study are only based on the two cases shown and should therefore be extrapolated with care. Possible future work includes investigating if this approach is accurate and computationally efficient for other structural fire problems, such as larger structural systems, concrete and composite systems, combustible assemblies, or a hybrid localized – traveling fire.

Chapter 4 Modeling Fire Spread in Large Compartments using a Transient Flux-Time Product Model for Ignition

4.1 Introduction

This chapter aims to formulate a realistic design fire for large compartments, which will aid structural fire engineers in their endeavor to provide safe, economic, sustainable, and modern structural fire designs. The novel fire spread model outlined in this chapter realistically models fire progression by considering fire spread from object to object through use of an improved flux-time product ignition model. Burning objects (e.g., workstations) are simulated as equivalent burners to increase computational efficiency. When an object is predicted to ignite, it burns with a heat release rate measured for the object by experimental fire tests. Heat and mass transfer is simulated in CFD, which allows the realistic capturing of fire dynamics.

To formulate a CFD fire model that employs realistic fire progression, a model to predict the ignition of an object within the compartment needs to be included. Implementing a critical ignition temperature is one method of predicting ignition (i.e., when an object reaches its critical ignition temperature it is assumed to ignite), but this method would require the heat transfer between the fire and the objects in the compartment to be modeled. This would significantly increase computational expense. Additionally, FDS uses a 1-D conduction model that produces unreliable predictions of the surface temperature in solids [40]. Instead, using a flux-time product ignition model was explored in the study because it does not require the modeling of the physical objects in the CFD simulation. The flux-time product model defines a minimum heat flux-time

product exposure for an object, that when reached, means the object has ignited. There have been different variations proposed of the flux-time product ignition model, which are presented below.

The original flux-time product model was developed by Smith and Satija [56]. This method calculates an object's total flux-time product exposure as a summation of its flux-time product exposure at each time step. At each time step, the flux-time product is calculated by subtracting the object's self-propagating flux (i.e., the flux at which a flame will propagate from a point of flame impingement) from the average incident flux over the time increment. This value is then raised to the power of an empirical constant and multiplied by the length of the time step. The minimum flux-time product exposure required for ignition is calculated by subtracting the object's self-propagating flux from the average incident flux and then multiplying this value by the time-to-ignition.

Implementation of this method requires experimental data that are not readily available for most materials, such as the self-propagating flux. In addition, to determine the minimum flux-time product for ignition the authors [56] recommend using experimental data from four or five different constant heat flux exposures. Therefore, the minimum flux-time product used in [56] is based on constant heat flux exposure and is not theoretically accurate when considering the time-varying heat flux exposure that objects experience during a real fire event. The method also ignores thermal thickness, which impacts ignition.

Mikkola and Wichman [57] sought to develop a fundamental theory to correlate heat flux and time-to-ignition experimental data. The equation determined by the study was based on a solution to the one-dimensional heat equation. The solutions for both thermally thick solids and thermally thin solids were determined. For thermally thick solids, time-to-ignition was related to heat flux squared through density, specific heat, conductivity and the square of the ignition

temperature. For thermally thin solids, time-to-ignition was related to heat flux through density, specific heat, thickness and ignition temperature.

Mikkola and Wichman [57] presented a theoretical method for correlating time to ignition and heat flux that did not rely on experimental data and considered the thermal thickness. But these solutions were derived using a constant heat flux assumption and therefore cannot be used to relate time-to-ignition and heat flux during a fire event where heat flux will vary with time.

A modified flux-time product model was developed by Shields et al. [58]. The authors obtained a linear relationship for the incident flux and the reciprocal of the nth power of time-to-ignition. By plotting the relationship between incident heat flux and the nth power of time-to-ignition, values for the flux-time product and the critical irradiance can be obtained. The critical irradiance is defined by the intercept on the incident heat flux axis, and the slope of the line is used to determine FTP. Therefore, similar to the method developed by Smith and Satija [56], experimental data for different heat exposures was needed for each material to create this plot. This method improves on the original method though by considering thermal thickness. The inverse of the flux-time product index is set equal to approximately 2 for thermally thick materials, 3/2 for thermally intermediate materials and 1 for thermally thin materials. However, similar to the method by References [56], [57], this method is based on an assumption of constant heat flux exposure and is therefore unable to accurately predict ignition for an object exposed to time-varying heat flux.

In summary, the main drawbacks to the previously developed FTP method are (1) they do not consider time varying heat flux exposure that objects would experience during a fire event, and (2) they rely on experimental data to determine the minimum FTP for ignition that may not be available for all materials. To address these issues, the chapter proposes a new framework for fire

spread that includes an improved flux-time product ignition model for use in a computational fire spread model. The fire model is described in detail in the following sections.

4.2 Framework for Fire Spread Model

In the proposed fire spread model for large compartments, the fire dynamics will be modeled using the CFD code, Fire Dynamics Simulator (FDS), developed by the National Institute of Standards and Technology (NIST) [40]. The entire compartment is modeled using FDS, which allows the user to specify exact fuel load distributions, ventilation conditions, compartment geometry, and compartment linings. The fuel load of the fire is modeled as standard office furniture, such as couches, desks, workstations, and bookcases. Burning objects are simulated as equivalent burners with prescribed heat release rate curves that follow experimental measurements. Using the equivalent burner idealization instead of modeling the real objects in the fire simulation results in significant computational savings without sacrificing accuracy. In the proposed fire spread model, the simulation begins with the assumed ignition of a single object. When a second object is predicted to ignite, the equivalent burner for the second object turns on and follows the heat release rate curve of that object as measured experimentally. Ignition is predicted using an improved flux-time product ignition model that appears in section 4.3.

There is an empirical basis for the equivalent burner assumption. In these simulations, the type of fluid flow that occurs beneath the ceiling is referred to as a “ceiling jet”. Ceiling jet flow is caused by the rising of hot combustion gases, which results in a hot and rapidly moving gas layer beneath the ceiling. Alpert [25] presents correlations to identify ceiling jet gas temperatures. These correlations determine the gas temperature based on the heat release of the fire, the height of the compartment, and the radial distance from the center of the fire. All of these parameters are represented and maintained in our equivalent burner assumption. In order to validate the equivalent

burner assumption used in this fire spread model, two simulations of burning single-seat couches were performed in FDS. In couch simulation 1, the physical couch is explicitly modeled. The couch foam is modeled as polyurethane, covered with polypropylene fabric. There is a small propane burner placed above the seat of the couch that causes the couch to ignite. As the couch is burning, the physical material of the couch is consumed and burns away. This simulation is shown in Figure 4.1a. In couch simulation 2, only a single burner is modeled. The heat release rate of the burner follows the heat release rate of couch simulation 1. The soot yield of the burner was set equal to the soot yield of polyurethane, 0.131 [39]. This simulation is shown in Figure 4.1b.

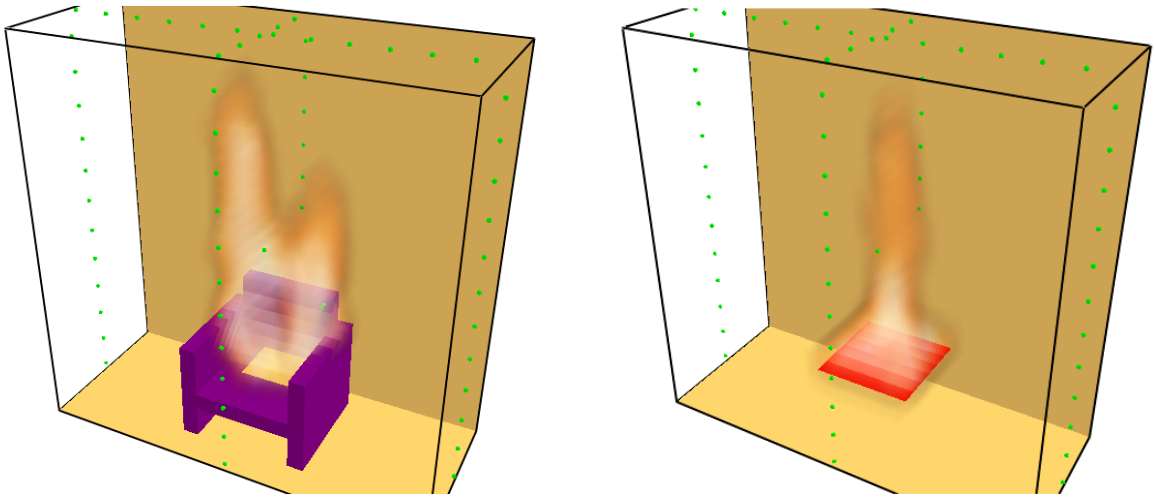

Figure 4.1 - Couch and equivalent burner CFD simulations, respectively

The couch simulations were modeled to test if the equivalent burner assumption could be used to accurately model burning objects. To determine if this assumption is valid, adiabatic surface temperature (AST) and heat transfer coefficient (HTC) results at the ceiling were compared between both simulations. Specifically, these metrics were used because adiabatic surface temperature and heat transfer coefficient values from the CFD simulation are used to define the

boundary condition in the structural model and therefore must be accurate in order to correctly model the structural response, as determined by [12].

The results for adiabatic surface temperature at the ceiling of both simulations are compared below. Figure 4.2a compares AST along the length of ceiling and Figure 4.2b compares AST along the width of the ceiling.

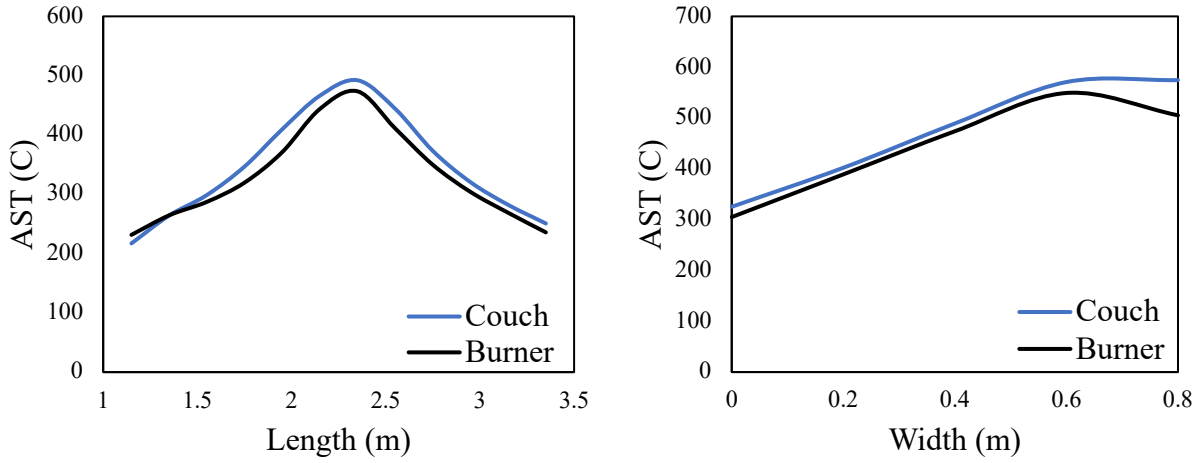

Figure 4.2 - AST results along the length and width of the ceiling, respectively

The comparison shown in Figure 4.2a and 4.2b shows close agreement of the predicted AST values when the couch is physically modeled in the CFD simulation and when the couch is modeled as an equivalent burner. From this comparison, it can be concluded that the equivalent burner assumption produces accurate AST results at the ceiling.

The results for heat transfer coefficient at the ceiling of both simulations are compared below. Figure 4.3a compares HTC along the length of ceiling and Figure 4.3b compares HTC along the width of the ceiling.

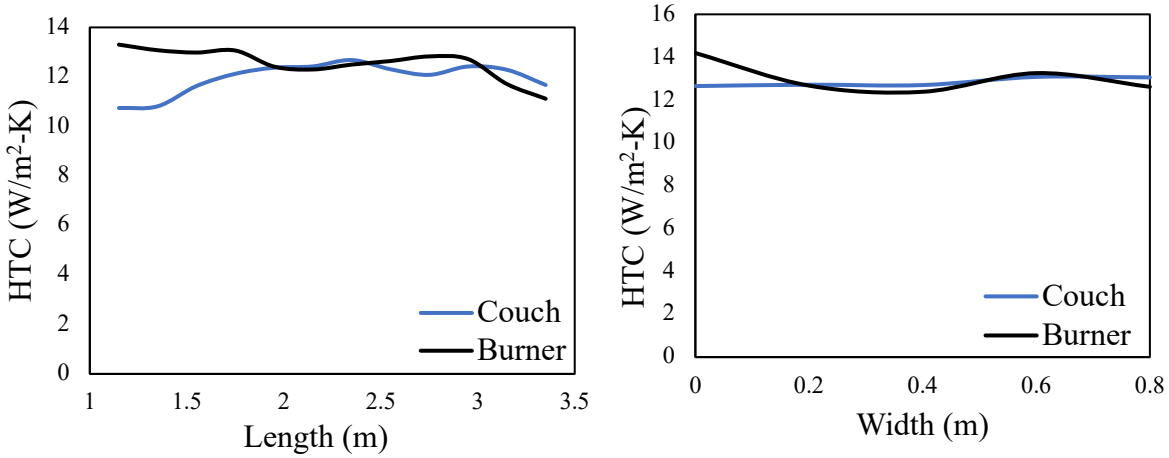

Figure 4.3 - HTC coefficient results along the length and width of the ceiling, respectively

The comparison shown in Figure 4.3a and 4.3b again shows close agreement of the predicted HTC values when the couch is physically modeled in the CFD simulation and when the couch is modeled as an equivalent burner. From this comparison, it can be concluded that the equivalent burner assumption produces accurate HTC results at the ceiling.

Couch simulation 1 and couch simulation 2 were run for equal simulation time, but couch simulation 1 completed in a wall clock time of approximately 42 minutes while couch simulation 2 completed in a wall clock time of approximately 33 minutes. Therefore, couch simulation 2 reflected an approximate 21 percent decrease in computational cost, which is significant when the fire spread simulations are scaled up to include an entire office floor.

4.3 Transient Flux-Time Product Ignition Model

The derivation for the proposed flux-time product ignition model begins with the one-dimensional heat conduction equation.

$$\frac{\partial^2 T}{\partial x^2} = \frac{1}{\alpha}\frac{\partial T}{\partial t} \qquad [4.1]$$

Where T = temperature, x = position, t = time, and α = thermal diffusivity.

A unit heat flux at the boundary is imposed, i.e.,

$$q(0,t) = q \quad [4.2]$$

Where q = heat flux.

Heat flux can be represented as

$$q = -k\frac{\partial T}{\partial x} \quad [4.3]$$

Where k = thermal conductivity.

The boundary condition at the heated surface is determined by combining Eqn. [4.2] and Eqn. [4.3], i.e.,

$$\frac{\partial T}{\partial x}(0,t) = -\frac{q}{k} \quad [4.4]$$

The object is assumed to have uniform temperature initially. An initial temperature of zero will be used in this derivation for simplicity. In practice, this means the temperature solution from this problem will represent a temperature difference between the initial temperature and final temperature. Using the assumption of an initial temperature equal to zero, we can define the remaining initial and boundary conditions, i.e.,

$$T(x,t) = T(0,0) = 0 \quad [4.5]$$

$$T(x,t) = T(\infty,t) = 0 \quad [4.6]$$

Eqn. [4.5] states that at the start of the analysis, the surface temperature of the object is zero. Eqn. [4.6] states that at an infinite depth of the solid, at any time, the temperature of the solid has not been affected by the applied heat flux, which is suitable for a thermally thick solid.

Eqn. [4.1] can be re-written as

$$\frac{\partial T}{\partial t} = \alpha\frac{\partial^2 T}{\partial x^2} \quad [4.7]$$

Using LaPlace transforms,

$$L_t\left\{\frac{\partial T}{\partial t}\right\} = L_t\left\{\frac{\partial^2 T}{\partial x^2}\right\} \quad [4.8]$$

Setting $\bar{T} = L(T)$, Eqn. [4.8] can be written as

$$p * L\{T\} - T[x,0] = \alpha\frac{\partial^2 T}{\partial x^2} \quad [4.9]$$

where p is defined by the equation,

$$L\{f(U)\} = \int_0^\infty e^{-pU} f(U)dU \quad [4.10]$$

or

$$p\bar{T} = \alpha\frac{\partial^2 T}{\partial x^2} \quad [4.11]$$

Eqn. [4.11] can be rewritten as

$$\frac{\partial^2 T}{\partial x^2} = \frac{1}{\alpha}p\bar{T} \quad [4.12]$$

Using the operator method of solution [59] on Eqn. [4.12],

$$\left(D^2 - \frac{p}{\alpha}\right)\bar{T} = 0 \quad [4.13]$$

$$m^2 = \frac{p}{\alpha};\ m = \pm\sqrt{\frac{p}{\alpha}} \quad [4.14]$$

Therefore,

$$\bar{T} = C_1 e^{\sqrt{\frac{p}{\alpha}}x} + C_2 e^{-\sqrt{\frac{p}{\alpha}}x} \quad [4.15]$$

The constants of integration (C_1 and C_2) need to be evaluated. In order to do this, the LaPlace transform of the boundary condition needs to be taken. The LaPlace transform of Eqn. [4.6] is

$$\bar{T}(\infty, t) = L\{0\} = 0 \quad [4.16]$$

Then, the boundary condition is applied to Eqn. [4.15] as x approaches infinity, i.e.,

$$\bar{T} = 0 = C_1 e^{\sqrt{\frac{p}{\alpha}}x} + C_2 e^{-\sqrt{\frac{p}{\alpha}}x} \quad [4.17]$$

with

$$\lim_{x\to\infty} C_1 e^{\sqrt{\frac{p}{\alpha}}x} = \infty \quad [4.18]$$

$$\lim_{x\to\infty} C_2 e^{-\sqrt{\frac{p}{\alpha}}x} = 0 \quad [4.19]$$

For Eqn. [4.17] to hold true, C_1 must be equal zero.

Eqn. [4.15] then becomes

$$\bar{T} = C_2 e^{-\sqrt{\frac{p}{\alpha}}x} \quad [4.20]$$

Eqn. [4.4] can be used to solve for the second integration constant. The LaPlace transform of Eqn. [4.4] is

$$\frac{\partial \bar{T}}{\partial x}(0,t) = -\frac{q}{k * p} \quad [4.21]$$

The derivative of Eqn. [4.20] with respect to x is

$$\frac{\partial \bar{T}}{\partial x} = C_2 \left(-\sqrt{\frac{p}{\alpha}}\right) e^{-\sqrt{\frac{p}{\alpha}}x} \quad [4.22]$$

Applying the boundary condition represented by Eqn. [4.7] to Eqn. [4.22] yields

$$\frac{\partial \bar{T}}{\partial x}(0,t) = C_2 \left(-\sqrt{\frac{p}{\alpha}}\right) \quad [4.23]$$

Eqns. [4.21] and [4.23] are both expressions for $\frac{\partial \bar{T}}{\partial x}$ at $x = 0$ and can be set equal, which gives

$$-\frac{q}{k * p} = -C_2 \left(\sqrt{\frac{p}{\alpha}}\right) \quad [4.24]$$

Solving for C_2 yields

$$C_2 = \frac{q}{kp}\sqrt{\frac{\alpha}{p}} \quad [4.25]$$

Substituting C_2 into Eqn. [4.20] gives

$$\bar{T} = \frac{q}{kp}\sqrt{\frac{\alpha}{p}}\, e^{-\sqrt{\frac{p}{\alpha}}x} \quad [4.26]$$

The inverse LaPlace transform of Eqn. [4.26] is

$$L_t^{-1}\{\bar{T}\} = L_t^{-1}\left\{\frac{q\sqrt{\alpha}}{k} * \frac{e^{-\sqrt{\frac{p}{\alpha}}x}}{p\sqrt{p}}\right\} = \frac{q\sqrt{\alpha}}{k}\, L_t^{-1}\left\{\frac{e^{-\sqrt{\frac{p}{\alpha}}x}}{\sqrt{p}} * \frac{1}{p}\right\} \quad [4.27]$$

The Convolution Theorem [60] needs to be used to continue solving for the inverse LaPlace transform on this equation. The Convolution Theorem equation is as follows

$$L^{-1}\{f_1(p)f_2(p)\} = F_1(t) * F_2(t) = \int_0^t F_1(\lambda)F_2(t-\lambda)d\lambda \quad [4.28]$$

In this case,

$$f_1(p) = \frac{e^{-\sqrt{\frac{p}{\alpha}}x}}{\sqrt{p}} \xrightarrow{yields} F_1(t) = \frac{1}{\sqrt{\pi t}} e^{\frac{-x^2}{4\alpha t}} \quad [4.29]$$

$$f_2(p) = \frac{1}{p} \xrightarrow{yields} F_2(t) = 1 \quad [4.30]$$

Eqn. [4.27] now becomes,

$$T = \frac{q\sqrt{\alpha}}{k\sqrt{\pi}}\int_0^t \frac{e^{\frac{-x^2}{4\alpha\lambda}}}{\sqrt{\lambda}}d\lambda \quad [4.31]$$

Integrating Eqn. [4.31] gives

$$T(x,t) = \frac{q}{k}\left[\sqrt{x^2}erf\left(\frac{\sqrt{x^2}}{2\sqrt{\alpha t}}\right) + \frac{2\sqrt{\alpha t}}{\sqrt{\pi}\, e^{\frac{x^2}{4\alpha t}}} - x\right] \quad [4.32]$$

In order to obtain an equation for the surface temperature, x is set equal to zero, which gives

$$T(t) = \frac{2q}{k}\sqrt{\frac{\alpha t}{\pi}} \quad [4.33]$$

Eqn. [4.33] represents the surface temperature of a thermally thick solid when exposed to a unit heat flux (q). To expand this equation to include a time-varying heat flux, Duhamel's Integral is used. Duhamel's theorem is represented by the equation below.

$$T(x,t) = \int_0^t U(x, t-\gamma)\frac{dF}{d\gamma}d\gamma \quad [4.34]$$

Where $U(x,t)$ = fundamental solution (Eqn. [4.33] in this case), F = forcing function and γ = variable of integration.

The forcing function represents the time-varying heat flux. In this case, the forcing function is a step-wise function, i.e., the heat flux is assumed to be constant over the duration of the time step, and then jumps to a new value for the next time step and so on. The general equation for Duhamel's integral considering a piecewise forcing function has been derived [61] and is presented below.

$$T(x,t) = \Delta F_0 U(x,t) + \sum_{i=1}^{M}[\Delta F_i U(x, t - t_{i-1})] \quad [4.35]$$

Where ΔF_i = change in heat flux between time steps.

Substituting the fundamental solution, Eqn. [4.33], into Eqn. [4.35] yields

$$T(t) = \Delta F_0 \left(\frac{2}{k} \sqrt{\frac{\alpha t}{\pi}} \right) + \sum_{i=1}^{M} \left[\Delta F_i \left(\frac{2}{k} \sqrt{\frac{\alpha (t - t_{i-1})}{\pi}} \right) \right] \quad [4.36]$$

In order to formulate an equation for flux-time product exposure, the heat flux (ΔF_i) and time variables are isolated on the left-hand side of the equation, and the temperature is set equal to ignition temperature. This gives the following equation for FTP for thermally thick fuels.

$$FTP_{thick\ fuels} = \Delta F_0 \sqrt{t} + \sum_{i=1}^{M} \Delta F_i \sqrt{(t - t_{i-1})} = \frac{k}{2} \sqrt{\frac{\pi}{\alpha}} (T_{ig} - T_0) \quad [4.37]$$

The right-hand side of Eqn. [4.37] are all material constants, which means the threshold FTP value is constant. Ignition temperature, conductivity, and thermal diffusivity are well-documented for most materials. Therefore, this method does not require experimental data to implement.

A similar procedure was followed to determine the threshold FTP values for thermally thin fuels. Substituting the fundamental solution for thermally thin fuels into Eqn. [4.35] gives an expression for temperature in thin fuels subjected to a varying heat flux, i.e.,

$$T(t) = \Delta F_0 \left(\frac{t}{\rho c \tau} \right) + \sum_{i=0}^{M} \left[\Delta F_i \left(\frac{t - t_{i-1}}{\rho c \tau} \right) \right] \quad [4.38]$$

Isolating the heat flux and time variables on the left-hand side of the equation and setting temperature equal to ignition temperature yields the equation for FTP for thin fuels, i.e.,

$$FTP_{thin\ fuels} = \Delta F_o t + \sum_{i=0}^{M} \Delta F_i (t - t_{i-1}) = (\rho c \tau)(T_{ig} - T_0) \quad [4.39]$$

As with the equation for FTP in thick fuels, the right-hand side of Eqn. [4.39] contains all material constants, meaning the threshold FTP value is constant. Like the FTP equation for thick

fuels, the FTP equation for thin fuels uses well-documented material properties and does not require experimental data to implement.

The flux-time product method proposed here builds on prior work to account for ignition from a time-varying heat flux boundary condition. In order to show the importance of including the time-varying heat flux boundary condition, a comparison of ignition predictions considering time-varying heat flux versus constant heat flux is presented.

4.4 Ignition Predictions for Time-Varying Heat Flux

In the simulations presented below, the object is modeled as thermally-thick wood, with density = 450 kg/m^3, specific heat = 1.2 kJ/kg/K, thermal conductivity = 0.13 W/m/K, and ignition temperature = 360°C [62]. The FTP exposure that considers time-varying heat flux is calculated according to Eqn. [4.37]. The FTP exposure that assumes constant heat flux is calculated according to Reference [57].

The first comparison is for a forcing function where the heat flux level is at 0 kW/m^2 initially, then in the first time step the heat flux increases to 150 kW/m^2 and remains at that level for 300s before decreasing to 50 kW/m^2 for the duration of the simulation, which concludes at 500s. The forcing function is shown graphically in Figure 4.4a and the corresponding surface temperature of the object is shown in Figure 4.4b. Figures 4.4c and 4.4d graph the FTP exposure of the object and the limiting FTP required for ignition as calculated by the time-varying heat flux method and the constant heat flux method, respectively.

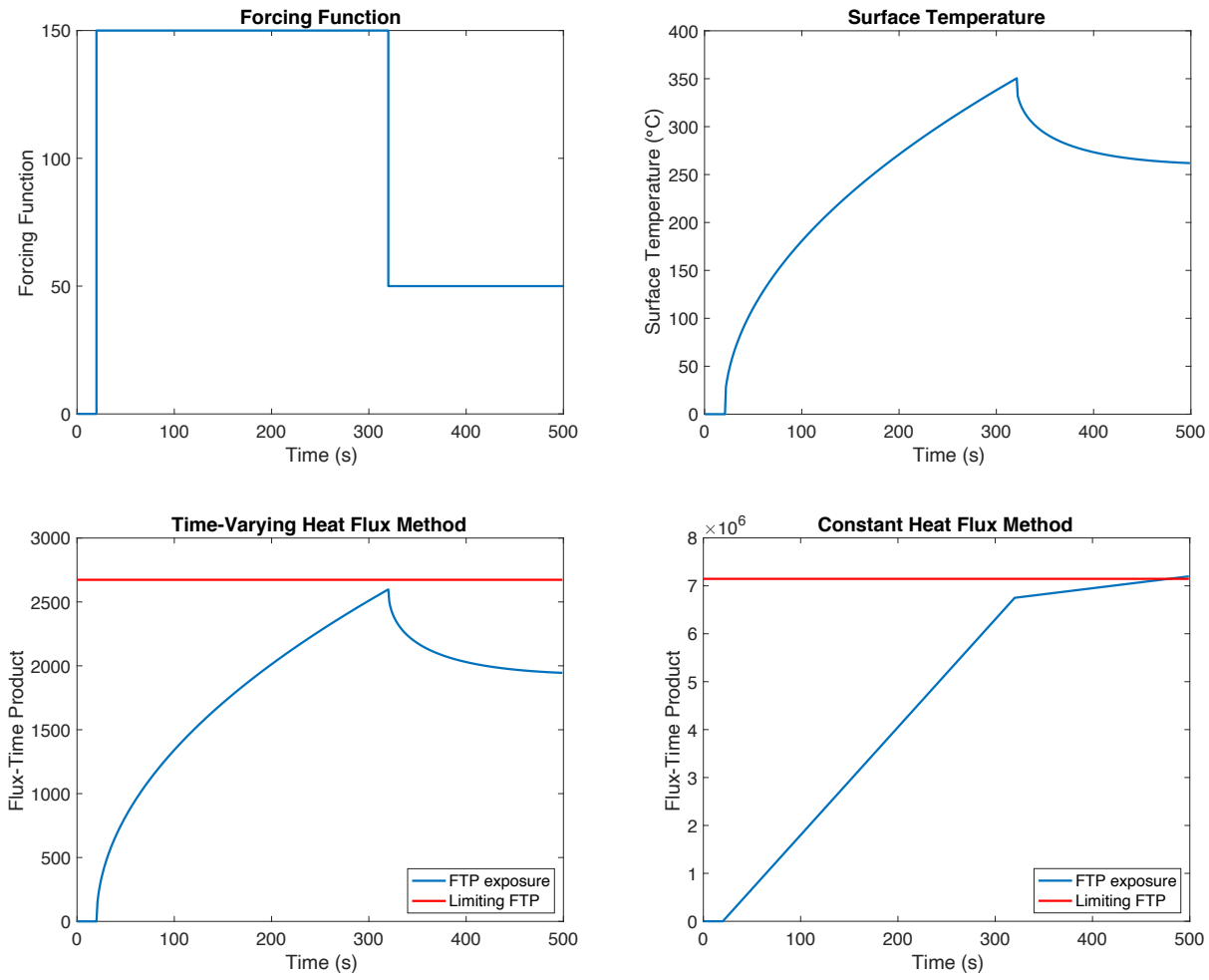

Figure 4.4 - FTP method comparison for case 1

Under this forcing function, the FTP method that considers time-varying heat flux (i.e., Eqn. [4.47]) predicted the object would not ignite when subjected to this forcing function. As shown in Figure 4.4c, the FTP exposure never exceeds the limiting FTP using this method. The FTP method that assumes constant heat flux predicted that the object would ignite at 479 s when the surface temperature of the object was 262.98 °C, which is significantly lower than the ignition temperature of the material. Thus, the constant heat flux method erroneously predicts ignition in a case where the solid should not ignite.

Next, consider a forcing function where the heat flux level at each time step is oscillating. In this example, the heat flux is set to 0 kW/m^2 initially, and then oscillates between heat flux

values of 10 and 300 kW/m^2 for the duration of the simulation which concludes at 360 s. The forcing function is shown graphically in Figure 4.5a and the corresponding surface temperature of the object is shown in Figure 4.5b. Figures 4.5c and 4.5d graph the FTP exposure of the object and the limiting FTP required for ignition as calculated by the time-varying heat flux method and the constant heat flux method, respectively.

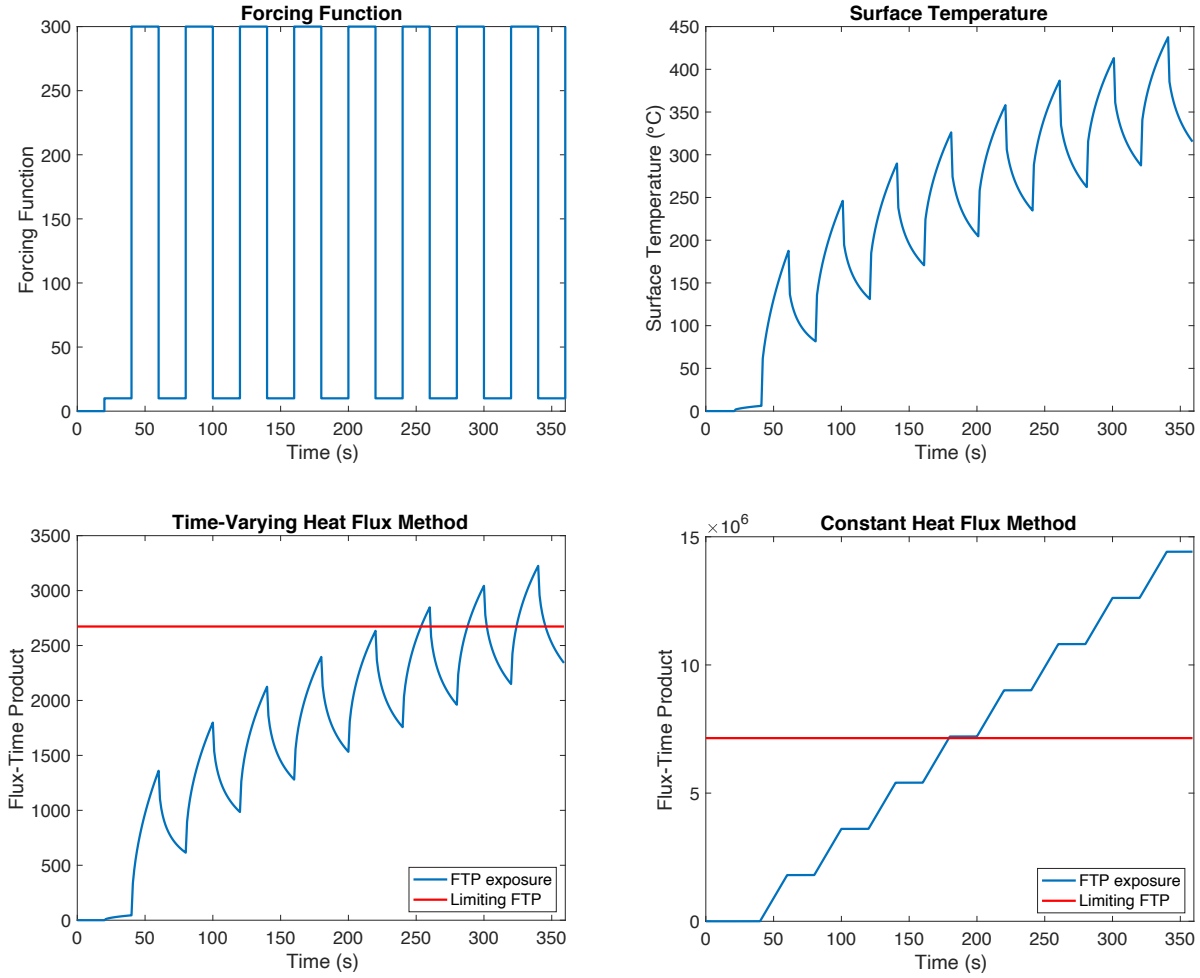

Figure 4.5 - FTP method comparison for case 2

Under this forcing function, the FTP method that assumes constant heat flux predicted that the object would ignite at 180 s when the surface temperature of the object was 322.72 °C, which is again significantly lower than the ignition temperature of the material. The FTP method that considers time-varying heat flux (Eqn. [4.37]) predicted ignition at 254 s when the surface

temperature of the object was 361.66 °C, which was the first time step during which the surface temperature of the object had exceeded the ignition temperature of the material.

The constant heat flux method produces inaccurate predictions of ignition under time-varying heat flux exposure. This occurs because the equation used to calculate the flux-time product exposure of the object at a given time step does not have the ability to adjust to changes in heat flux. The flux-time product exposure for the object can only increase resulting in premature predictions of ignition.

The predictions from these simulations show the importance of considering the time-varying heat flux when determining ignition during a fire event. The method developed in this section has the ability to adapt to changing heat flux values and give an accurate prediction of ignition. It also relies only on well-documented material data for ease of implementation into a computational fire spread model.

4.5 Validation of the Fire Spread Model Against NIST Workstation Tests

To validate the accuracy of the ignition and fire spread model developed in this paper, a comparison to a fire spread experiment was performed. NIST [2] studied fire spread between three computer workstations composed of a desk, fabric-lined partitions, a chair, carpeting, cabinets and a computer. The experiment was performed in a steel-framed compartment lined with calcium silicate board. The approximate dimensions of the compartment were 3 m x 7 m x 4 m. The fire was initiated by igniting a 1 m x 2 m pan filled with heptane, which was placed next to workstation 1. The fire progressed from workstation 1 to workstation 2, and then finally to workstation 3. There were ventilation openings located in the west side of the compartment. The floor plan of experiment is shown in Figure 4.6.

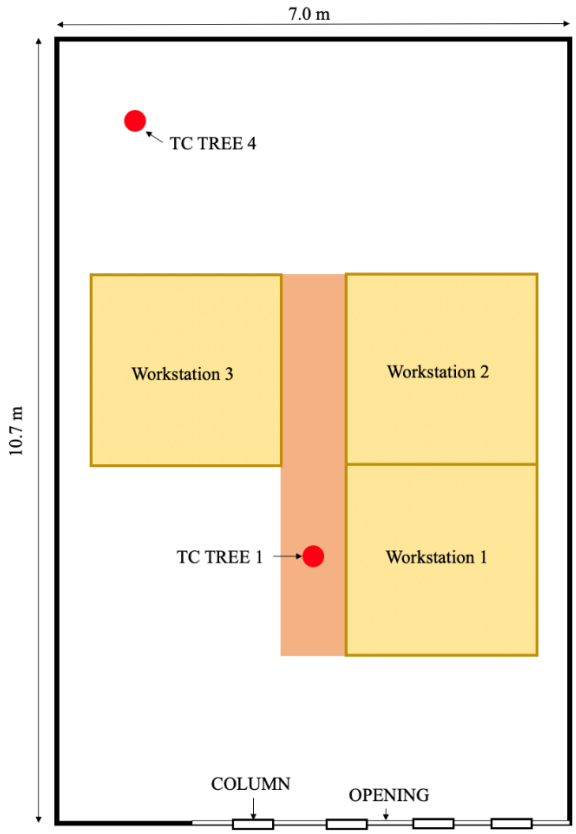

Figure 4.6 - Floorplan of NIST's fire spread experiment [2]

An FDS simulation of this fire spread experiment was performed, where the entire compartment was modeled. The workstations and carpet panels were modeled as equivalent burners with the heat release rate determined by available experimental data [63], [64]. Fire spread through the workstations and carpet was modeled according to the proposed time-varying flux-time product model.

NIST [63] performed fire tests of the single workstations used in the fire spread experiment and recorded the heat release rate. The workstations were ignited by placing a 1 m x 2 m pan filled with heptane next to the workstation and igniting it to produce a 2 MW fire for a duration of 10 minutes which was chosen to simulate an adjacent workstation. During these experiments, the first parts of the workstation to ignite were the piles of paper placed in the workstations, so therefore the material properties of paper were used to determine the minimum FTP required for ignition

(conductivity = 0.05 W/m-K, specific heat = 1.37 kJ/kg-K, thickness = 5 cm, ignition temperature = 230°C). The burner was assigned the soot yield of wood, 0.015 [39], because the mass fraction of the workstation is mainly wood. The heat release rate curve for the workstation is presented in Figure 4.7.

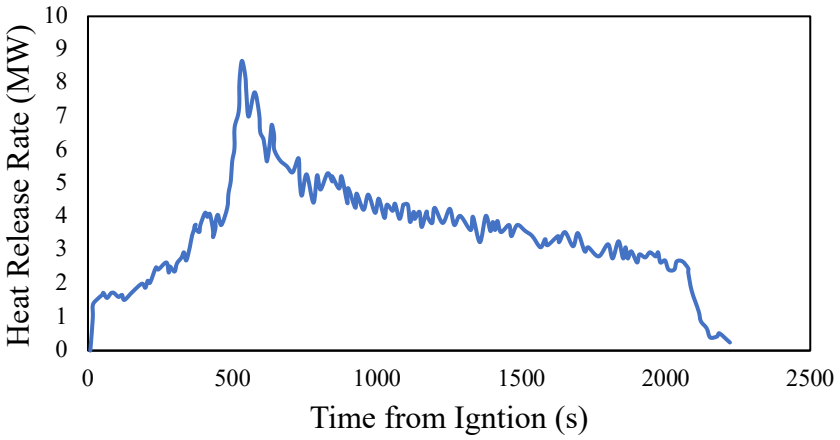

Figure 4.7 - Heat release rate of workstation [63]

The heat release rate of nylon carpet was experimentally recorded [64] and shown in Figure 4.8. In the simulation, nylon carpet was assumed to have density = 750 kg/m^3, conductivity = 0.16 W/m-K, specific heat = 4.5 kJ/kg-K and ignition temperature = 290°C [2]. The burner was assigned the soot yield of nylon, 0.075 [39].

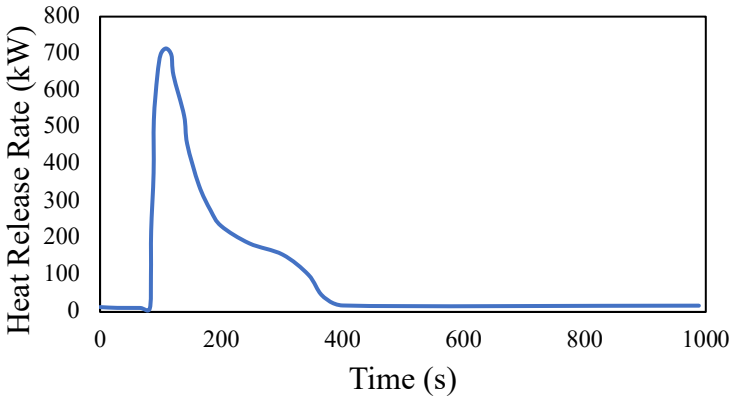

Figure 4.8 - Heat release rate of nylon carpet [64]

The FDS simulation modeled the three equivalent burners for the workstations, the fire pan, and the equivalent burners for the carpet tiles. Carpeting was included in the passageway between workstations 1, 2 and 3, as shown in Figure 4.6. In addition, the thermophysical properties of calcium silicate for the wall and ceiling lining were modeled (density = 737 kg/m^3, conductivity = 0.12 W/m-K, specific heat = 1.2 kJ/kg-K [2]). Note that the material properties for calcium silicate were the only material properties included in the simulation. The material properties of the workstation and the carpet were only used to predict ignition using the FTP model described in section 4.4.2. The ventilation was modeled in the west wall as shown in Figure 4.6 and the computational domain was extended 3 m beyond the west wall to include the flames flowing outside the compartment in the simulation. The dimensions computational domain were X: -3.0 m to 10.7 m, Y: 0.0 m to 7.0 m and Z: 0.0 m to 3.4 m. The mesh size for the simulation was 0.1 m and the number of radiation angles used was 500.

The heat release rate results, gas temperature and time to ignition results from the experiment and the FDS simulation were compared to validate the fire spread model. The experiment was repeated twice and both results are included in the following figures.

Figure 4.9 compares the heat release rate of the experiment (Test 1 and Test 2) and the FDS simulation.

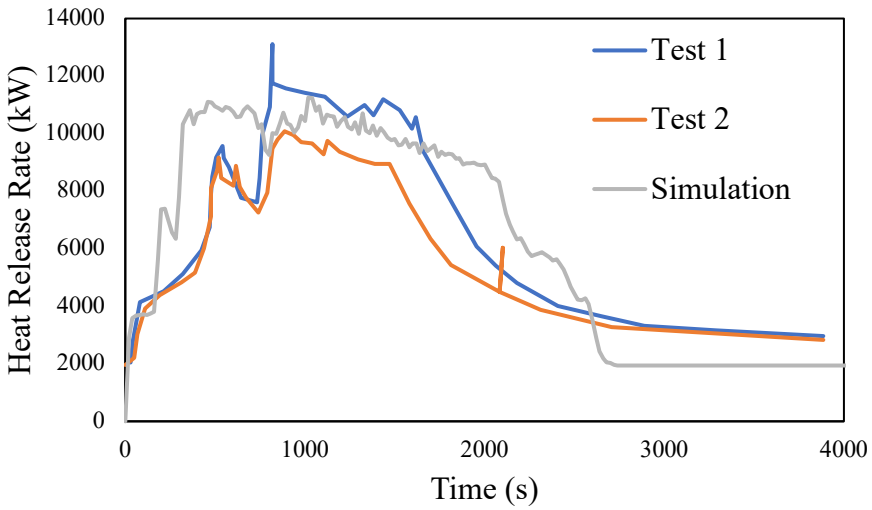

Figure 4.9 - Heat release rate comparison

The heat release rate of the experimental tests and the simulation are generally in agreement. The simulation accurately predicts the peak heat release rate although it over-predicts the heat release rate early in the simulation and then under-predicts the heat release rate near the end of the simulation.

Figures 4.10a-d compare the gas temperature for Tree 1 at various locations below the ceiling. Tree 1 is located outside the opening of workstation 1, and the exact location can be observed in the experimental layout provided in Figure 4.6.

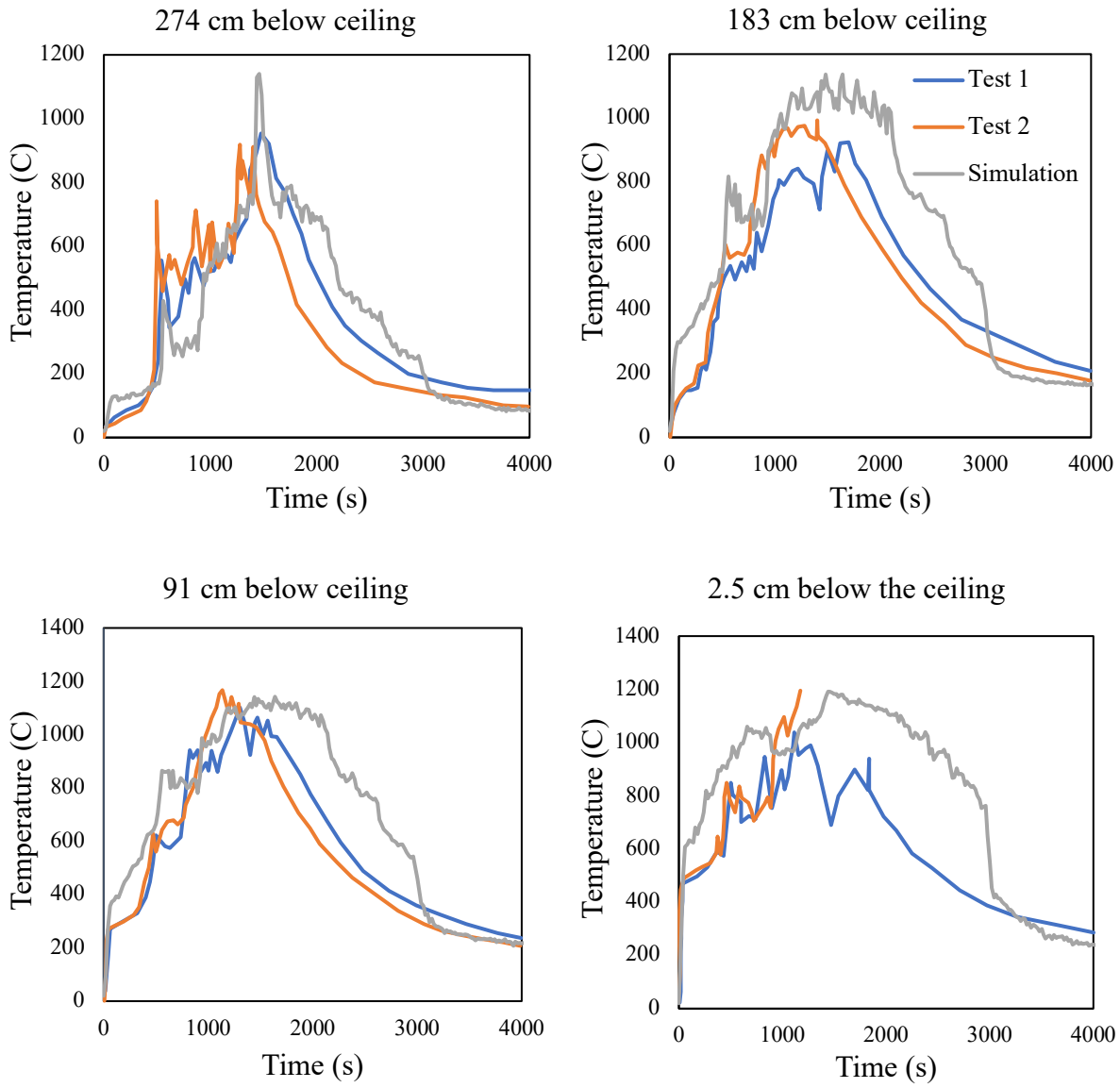

Figure 4.10 - Gas temperatures recorded at Tree 1

The gas temperatures recorded at Tree 1 between the experimental tests and the simulation are also generally in agreement. The time of peak gas temperatures is predicted accurately, and the magnitude is slightly higher in the simulations than in the actual tests. This is an acceptable result because it indicates that the simulation results in a conservative prediction.

Figures 4.11a-d compare the gas temperature for Tree 4 at various locations below the ceiling. Tree 4 is in the northeast corner of the compartment, and the exact location can be observed in the experimental layout provided in Figure 4.6.

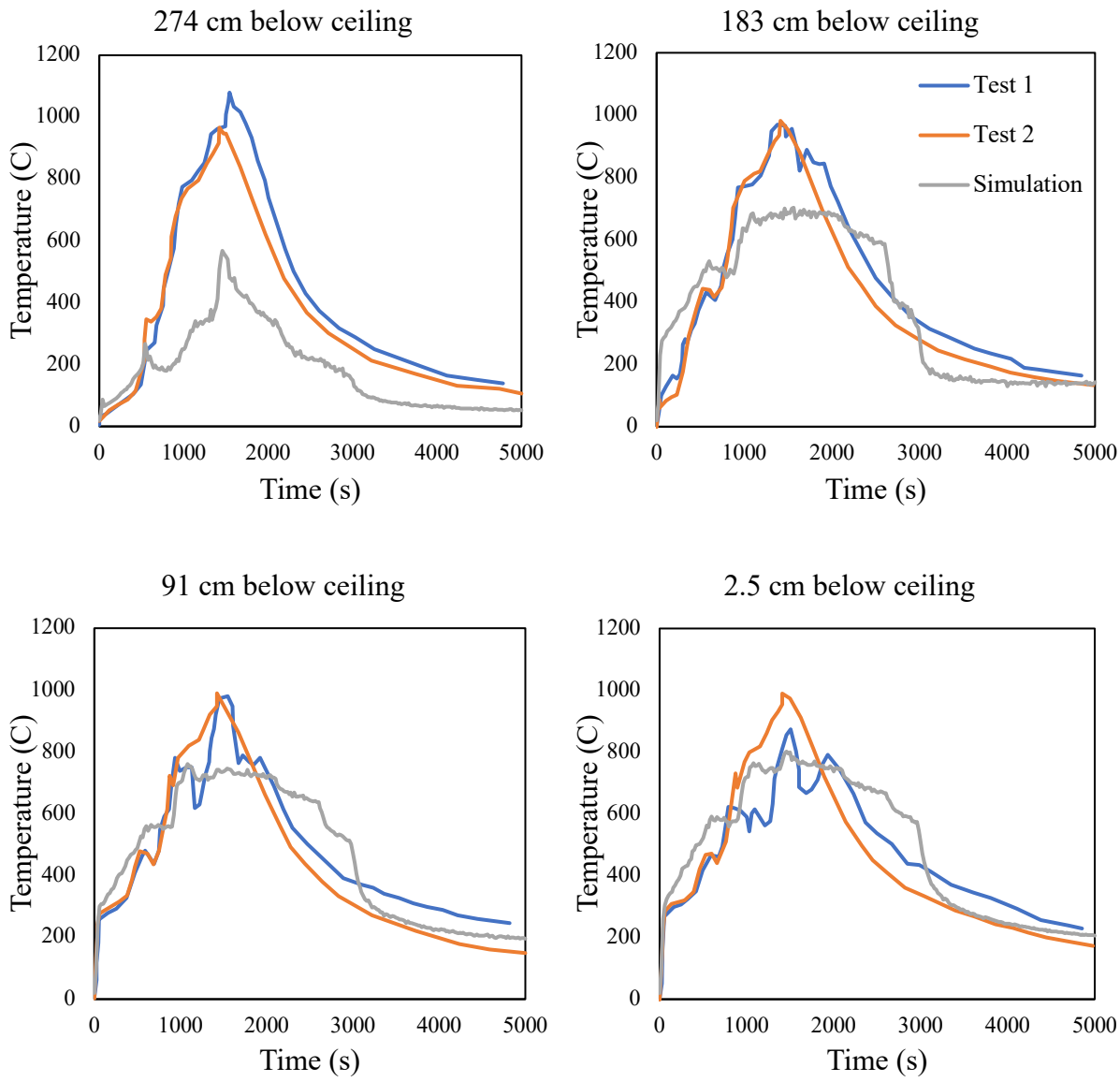

Figure 4.11 - Gas temperatures recorded at Tree 4

The gas temperatures between the experimental tests and the simulation are also generally in agreement. The time of peak gas temperatures is predicted accurately, although magnitude is under-predicted, in some instances significantly under-predicted, for example, at the thermocouple

located 274 cm below the ceiling. This could be caused by the fact that in the experiment, the actual workstations are represented, which have an elevation ranging from 0-1.2 m. In comparison, the burner can only be placed at a discrete elevation, in this case 0.7 m, which is the height of the desk. Therefore, the thermocouple in Figure 4.11a is located below the burner which could result in incorrect gas temperature predictions. Because the gas temperatures at the ceiling is the data that will transferred from the CFD model to the structural model, it is most important that this data is in good agreement with the experiments. The magnitude for the peak gas temperature recorded at 2.5 cm below the ceiling is in good agreement with the experimental tests and therefore the results from the simulation are considered acceptable.

The NIST experiment [2] began with the ignition of a fire pan adjacent to workstation 1. In test 1, the top of workstation 2 was obscured at 450 s and the video showed flames beginning to spread along one of the partition walls at 539 s. In test 2, video shows the ignition of one of the corners of workstation 2 occurring at 500 s. In our simulation, the ignition of workstation 2 occurred at 420 s. The ignition of workstation 3 in test 1 occurred between 555 s - 599 s, when the southwest corner of the workstation ignited. During test 2, at 534 s one of the partition walls of workstation 3 ignited. Our simulation predicted the ignition of workstation 3 at 520 s. The time to ignition predictions in our simulation are a close estimate of the actual time to ignition recorded for the workstations in the experimental tests. Ignition times for the experimental tests [2] and the simulation presented in this paper are compiled in Table 4.1 for clarity.

Table 4.1 - Ignition times

Ignition Time	Test 1	Test 2	Simulation
Workstation 2	~539s	500s	420s
Workstation 3	555-599s	534s	520s

4.6 Conclusions

The framework for a novel fire spread model for large compartments was presented and validated in this paper. The proposed fire spread model uses computational fluid dynamics to accurately model the fire dynamics as well as offering flexibility in regard to fuel load distribution, compartment characteristics, and ventilation conditions. The equivalent burner assumption used in the model was based on Alpert's findings and was validated here, showing that similar adiabatic surface temperature and heat transfer coefficient measurements were obtained at the ceiling, which is important to accurately predict the structural response.

In addition, a new flux-time product ignition model was presented for use with the fire spread model for large compartments to realistically model the fire progression. The flux-time product ignition model improves upon previous variations by only requiring well-documented material properties for implementation and including the capability to accurately predict ignition when an object is exposed to time-varying heat flux, which is the case in any fire event.

The fire spread model and the flux-time product ignition model were validated against workstation fire spread experiments conducted by NIST [2]. The simulated fire resulted in an accurate prediction of the heat release rate of the compartment, gas temperatures at the ceiling of the compartment, and time to ignition of the workstations.

The method presented in this paper presents an important path forward for simulating structural response under traveling fires. In particular, the methodology allows for patterns of burning to be simulated in a way that is more realistic than the simplified models that have been used up to this point. This will allow engineers to study structural response under more realistic traveling fire exposures to determine if there are aspects of the structural response that are not captured by simplified models.

Chapter 5 Parametric Fire Spread Study for Large Compartments

5.1 Introduction and Background

In order to address the limitations to existing design fire models, I developed a fire spread model for large compartments using a transient flux-time product model for ignition. The proposed fire spread model uses computational fluid dynamics to accurately model the fire dynamics as well as offering flexibility in regard to fuel load distribution, compartment characteristics, and ventilation conditions. In addition, a new transient flux-time product model for ignition realistically models the fire progression. The flux-time product ignition model improves upon previous variations by only requiring well-documented material properties for implementation and including the capability to accurately predict ignition when an object is exposed to time-varying heat flux, which is the case in any fire event. This method presents an important path forward for simulating structural response under traveling fires. In particular, the methodology allows for patterns of burning to be simulated in a way that is more realistic than the simplified models that have been used up to this point. This will allow engineers to study structural response under more realistic traveling fire exposures to determine if there are aspects of the structural response that are not captured by simplified models.

In this study, the fire spread model for large compartments with a transient flux-time product method for ignition is used to improve understanding of the nature of traveling fires. A parametric study is conducted where conditions of the fire are varied, such as the fire origin, ventilation conditions, heat release rate of the workstations, and fuel load density, to determine a

realistic range of gas temperatures and burning durations that a floor system may experience during a fire event. The goal of this work is to help inform designers regarding the range of the conditions that a structure may experience under fire exposure. Additionally, the range of gas temperature results and burning durations predicted in the parametric study of the fire spread model will be compared to that predicted by an existing fire model, the traveling fire model (TFM), to determine if a realistic range of fire exposures is represented in the current design models.

5.2 Fire Spread Model with Transient Flux-Time Product Framework

In the proposed fire spread model, the fire dynamics are modeled using the CFD code, Fire Dynamics Simulator (FDS), developed by the National Institute of Standards and Technology (NIST) [40]. The advantage to modeling the fire using computational fluid mechanics is that the user can specify the exact fuel load distributions, ventilation conditions, compartment geometry, and compartment linings, and the CFD model can provide an accurate representation of the fire dynamics. The fuel load of the fire is modeled as standard office furniture, such as couches, desks, workstations, and bookcases. Burning objects are simulated as equivalent burners with prescribed heat release rate curves that follow experimental measurements. Using the equivalent burner idealization instead of modeling the real objects in the fire simulation results in significant computational savings without sacrificing accuracy. In the proposed fire spread model, the simulation begins with the assumed ignition of an object. When a second object is predicted to ignite, the equivalent burner for the second object turns on and follows the heat release rate curve of that object as measured experimentally. Ignition is predicted using a transient flux-time product ignition model. The full derivation of the transient flux-time product ignition model and validation of the equivalent burner assumption can be found in Chapter 4.

5.2.1 Transient Flux-Time Product Ignition Model

To formulate a design fire that employs realistic fire progression, a model to predict the ignition of an object within the compartment needs to be included. Implementing a critical ignition temperature is one method of predicting ignition (i.e., when an object reaches its critical ignition temperature it is assumed to ignite), but this method would require the heat transfer between the fire and the objects in the compartment to be modeled. This would significantly increase computational expense. Additionally, FDS uses a 1D conduction model that produces unreliable predictions of the surface temperature in solids [40]. Instead, using a flux-time product ignition model was explored in the study because it does not require the modeling of the physical objects in the CFD simulation. The flux-time product model defines a minimum heat flux-time product exposure for an object that, when reached, means the object has ignited.

The transient flux-time product ignition method was derived from the 1D heat conduction equation. Duhamel's integral was used to consider the time-varying boundary conditions of the problem (in this case, transient heat flux). The equations for the transient flux-time product method for thermally-thick fuels (Eqn. 5.1) and thermally-thin fuels (Eqn. 5.2) are presented below. The left side of the equation represents the flux-time product exposure the object is subjected to at each time step. The right side of the equation represents the limiting flux-time time product needed for ignition. Therefore, if the left side of the equation exceeds the value of the right side, then the object has been ignited.

$$\mathrm{FTP}_{\text{thick fuels}}\colon\ \Delta F_0\sqrt{t} + \sum_{i=1}^{M} \Delta F_i \sqrt{(t - t_{i-1})} \ = \ \frac{k}{2}\sqrt{\frac{\pi}{\alpha}}(T_{ig} - \ T_0) \qquad [5.1]$$

$$\mathrm{FTP}_{\text{thin fuels}}\colon\ \Delta F_o t + \sum_{i=0}^{M} \Delta F_i (t - \ t_{i-1}) = (\rho c \tau)(T_{ig} - T_0) \qquad [5.2]$$

In Eqns. (5.1)-(5.2), ΔF is the forcing function, t is time, k is conductivity, α is thermal diffusivity, T_{ig} is the ignition temperature, T_0 is the initial temperature, ρ is density, c is specific heat, and τ is thickness.

The transient flux-time product ignition model explicitly considers the time-varying heat flux exposure that object experience during a fire. It can also be easily implemented into a computational model because it only requires well-documented material properties for implementation.

5.3 Parametric Study Methodology

5.3.1 Case Study Structure

The case study structure is a steel-framed building with a composite slab and exterior moment resisting frames to resist lateral loads. The design is presented by Agarwal and Varma [65] and adheres to current building codes and design specifications, such as the International Building Code [66], Minimum Design Loads for buildings and other Structures (ASCE-7) [67], Specification for Structural Steel Buildings (AISC-360) [68], and AISC Steel Design Guide 19 [69]. Each story of the building is 3.65 m (12 feet) tall, and the rectangular floor plan has 5 bays spanning the east-west (E-W) direction and 3 bays spanning the north-south (N-S) direction. The length of each bay is 7.62 m (25 feet).

The composite floor system includes a 65 mm (2.5 in.) thick lightweight concrete slab on a 75 mm (3.5 in.) deep ribbed deck. The slab included no additional reinforcement in accordance with US design codes. Only a single-story scenario is examined in this study and the fifth story of the building designed by Agarwal and Varma was modeled [65]. The primary interior gravity beams in the floorplan are W18x35 and the secondary interior gravity beams are W12x19. The E-W perimeter MRF beams are W18x60 and the N-S perimeter MRF beams are W21x93. The gravity

columns are W12x58, the E-W perimeter MRF columns are W14x99 (except corners) and the N-S perimeter MRF columns are W14x109 (including corners).

All members of the floorplan were designed to have at least one hour of fire resistance rating (FRR) in accordance with the International Building Code [66]. Design listings from Underwriters Laboratory (UL) [70] were used to design the passive fire protection. The fire protection design used CAFCO 300, a cementitious-based spray-applied fire resistive material (SFRM) applied to the beams and columns. This product has a thermal conductivity of 0.078 W/m-K, specific heat of 1200 J/kg-K and a density of 240 kg/m^3 at ambient temperature [71]. For a one-hour fire resistance rating, the W12x19 beam required 15 mm (9/16 in.) of fire protection, the W18x35 beam required 13 mm (1/2 in.) of fire protection and the W12x58 columns required 15 mm (9/16 in.) of fire protection. No additional fire protection was added to the steel deck of the composite floor system because the slab thickness was found to be adequate to provide a Fire Resistance Rating of 1 hour.

5.3.2 Fire Exposure

A parametric study is undertaken to characterize and improve understanding of the nature of traveling fires. One goal of developing this fire spread model was to determine the range of thermal environments large compartments may experience during a fire event. To that aim, a parametric study was carried out with varying thermal properties.

The thermal properties varied are the ignition location, ventilation conditions, the heat release rate of the workstations, and the fuel load density of the compartment. The ignition locations considered are the center, corner and perimeter of the floorplan. The opening factors considered were 0.04, 0.145, and 0.25. These values were chosen to represent the lowest and highest possible opening factors for a compartment [72]. The heat release rate of the workstations

was varied from a 0% increase of the experimental data to a 10% increase of the experimental data. This was done to reflect uncertainty in the contents and materials in the workstations. The experimental heat release rate used in this study is from NIST's fire tests of a generic workstation [63]. In this study, the researchers also tested the heat release rate of a typical World Trade Center workstation and found a 10% increase in the maximum heat release rate when compared to the that of the generic workstation. The fuel load density of the compartment was varied from 385 MJ/m^2 to 696 MJ/m^2 to represent a range of possible fuel load densities. For reference, NFPA 557 [73] recommends an average content fuel load density of 600 MJ/m^2 (with standard deviation of 500 MJ/m^2) for office buildings. Eurocode [18] recommends a fuel load density of 570 MJ/m^2 which is the 80th percentile design value for office buildings.

Table 5.1 summarizes the simulations that run for the parametric study and presents their naming convention. The letters in the beginning of the name indicate the ignition location of the fire. The first number refers to the opening factor (i.e., the number 1 indicates a low opening factor, and the number 3 indicates a high opening factor). The second and third number refer to the heat release rate and the fuel load density, respectively.

Table 5.1 - Naming convention for parametric study

Name	Ignition Location	Opening Factor	HRR	Fuel Load Density
cen111	center	0.04	+0%	385 MJ/m^2
cen131	center	0.04	+10%	385 MJ/m^2
cen221	center	0.145	+5%	385 MJ/m^2
cen311	center	0.25	+0%	385 MJ/m^2
cen331	center	0.25	+10%	385 MJ/m^2
cen132	center	0.04	+10%	696 MJ/m^2

cen332	center	0.25	+10%	696 MJ/m^2
corn111	corner	0.04	+0%	385 MJ/m^2
corn131	corner	0.04	+10%	385 MJ/m^2
corn221	corner	0.145	+5%	385 MJ/m^2
corn311	corner	0.25	+0%	385 MJ/m^2
corn331	corner	0.25	+10%	385 MJ/m^2
corn132	corner	0.04	+10%	696 MJ/m^2
corn332	corner	0.25	+10%	696 MJ/m^2
perim111	perimeter	0.04	+0%	385 MJ/m^2
perim131	perimeter	0.04	+10%	385 MJ/m^2
perim221	perimeter	0.145	+5%	385 MJ/m^2
perim311	perimeter	0.25	+0%	385 MJ/m^2
perim331	perimeter	0.25	+10%	385 MJ/m^2

5.3.3 Computational Fluid Dynamics Simulations

A CFD model of the compartment fire was created using Fire Dynamics Simulator version 6.7.4 [40] with a 0.15 x 0.15 x 0.15 m mesh. The number of radiation angles was set to 500. The fuel of the fire was considered to be the workstations and carpet present in the floorplan. The layout of the workstations for the fuel load density of 385 MJ/m^2 and 696 MJ/m^2 respectively, are presented in Figure 5.1a and Figure 5.1b. In both setups, the entire floor is covered in carpeting. Each blue square in the layout represents one workstation.

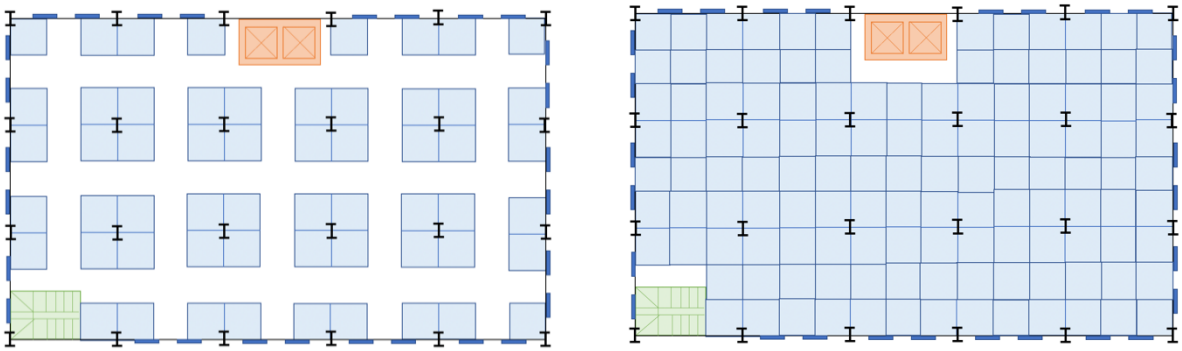

Figure 5.1 - Layout for fuel load density 385 MJ/m2 and 696 MJ/m2, respectively

The simulations began with the assumed ignition of four workstations in the ignition location. The initial ignited workstations are indicated in red for the center ignition scenario, purple for the corner ignition scenario, and green for the perimeter ignition scenario in Figure 5.2.

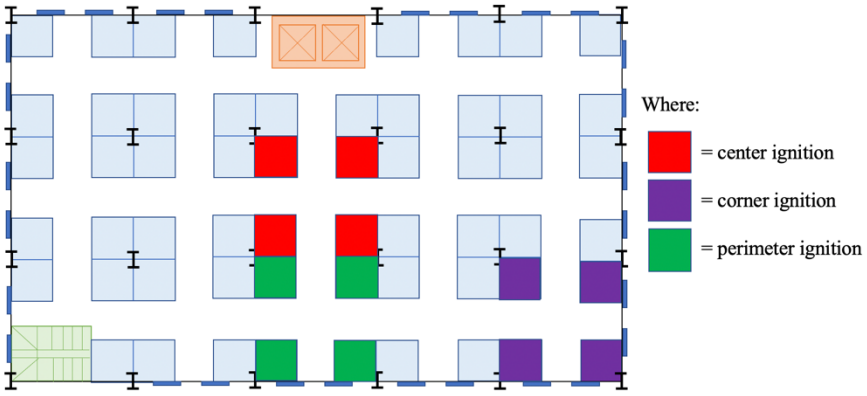

Figure 5.2 - Initial ignition configuration

NIST [63] performed fire tests of single workstations and recorded the heat release rate. During these experiments, the first parts of the workstation to ignite were the piles of paper placed in the workstations, so therefore the material properties of paper were used to determine the minimum FTP required for ignition (conductivity = 0.05 W/m-K, specific heat = 1.37 kJ/kg-K, thickness = 5 cm, ignition temperature = 230°C). The burner representing the workstation was assigned the soot yield of wood, 0.015 [39], because the mass fraction of the workstation is mainly wood. The heat release rate curve for the workstation is presented in Figure 5.3.

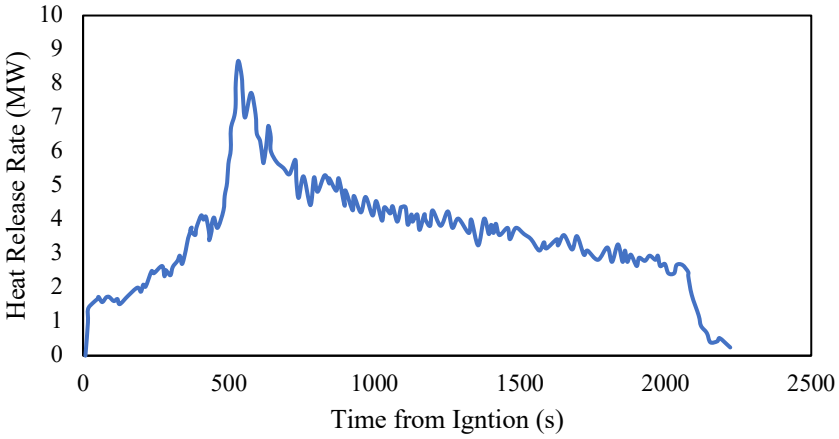

Figure 5.3 - Heat release rate of workstation [63]

The heat release rate of nylon carpet was experimentally recorded [64] and shown in Figure 5.4. In the simulation, nylon carpet was assumed to have density = 750 kg/m^3, conductivity = 0.16 W/m-K, specific heat = 4.5 kJ/kg-K and ignition temperature = 290°C [2]. The burner representing the carpet was assigned the soot yield of nylon, 0.075 [39].

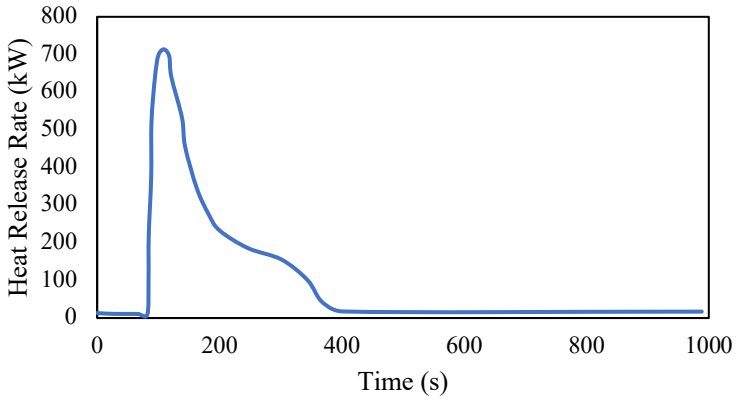

Figure 5.4 - Heat release rate of nylon carpet [64]

5.3.4 Finite Element Simulations

Thermal analyses of the interior gravity beams are included in this study. 2D thermal analyses are conducted using Abaqus/CAE 2019. The element type used is DC2D4. The temperature-dependent Eurocode [18] models for conductivity and specific heat of steel were input

into the FE model. Spatial [50] and temporal [51] homogenization algorithms were used to overcome differences in the space and time scale used in the CFD and FE analyses. Adiabatic surface temperature data from the CFD simulation were used to calculate the thermal boundary condition in the FE model as recommended by Chapter 3. The heat transfer coefficient was set to 35 W/m^2-K as recommend by Eurocode [18] for natural fire exposure.

A sensitivity study was carried out to determine the correct mesh size for the thermal analyses. The results of the sensitivity study are presented in Figure 5.5. Ultimately, the size of the mesh was limited by maintaining a 2:1 aspect ratio and a mesh size of 0.0125 m was used.

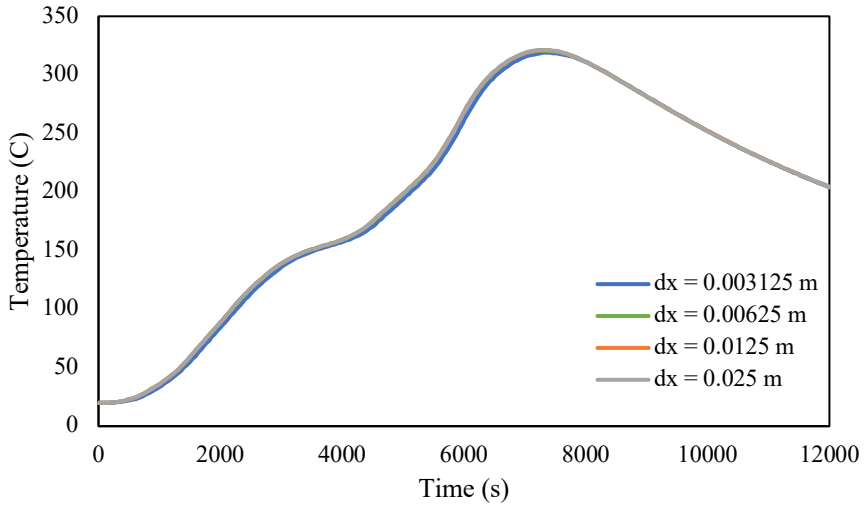

Figure 5.5 - Sensitivity study for FE analyses

5.4 Results

5.4.1 Ignition Location

Three different ignition locations were considered in this study. Ignition of the fire began with the assumed ignition of four workstations in either the center, corner or perimeter of the compartment.

In the center ignition simulations, the fire spread radially outward from the center of the floorplan where the fire initially began. The fire spread through the workstations for the cen331 case is presented below in Figure 5.6 by highlighting four separate time steps. The blue squares represent a workstation that has not yet ignited, the red squares represent workstations that are actively burning, and the black squares represent workstations that have burnt out (i.e., are no longer actively burning).

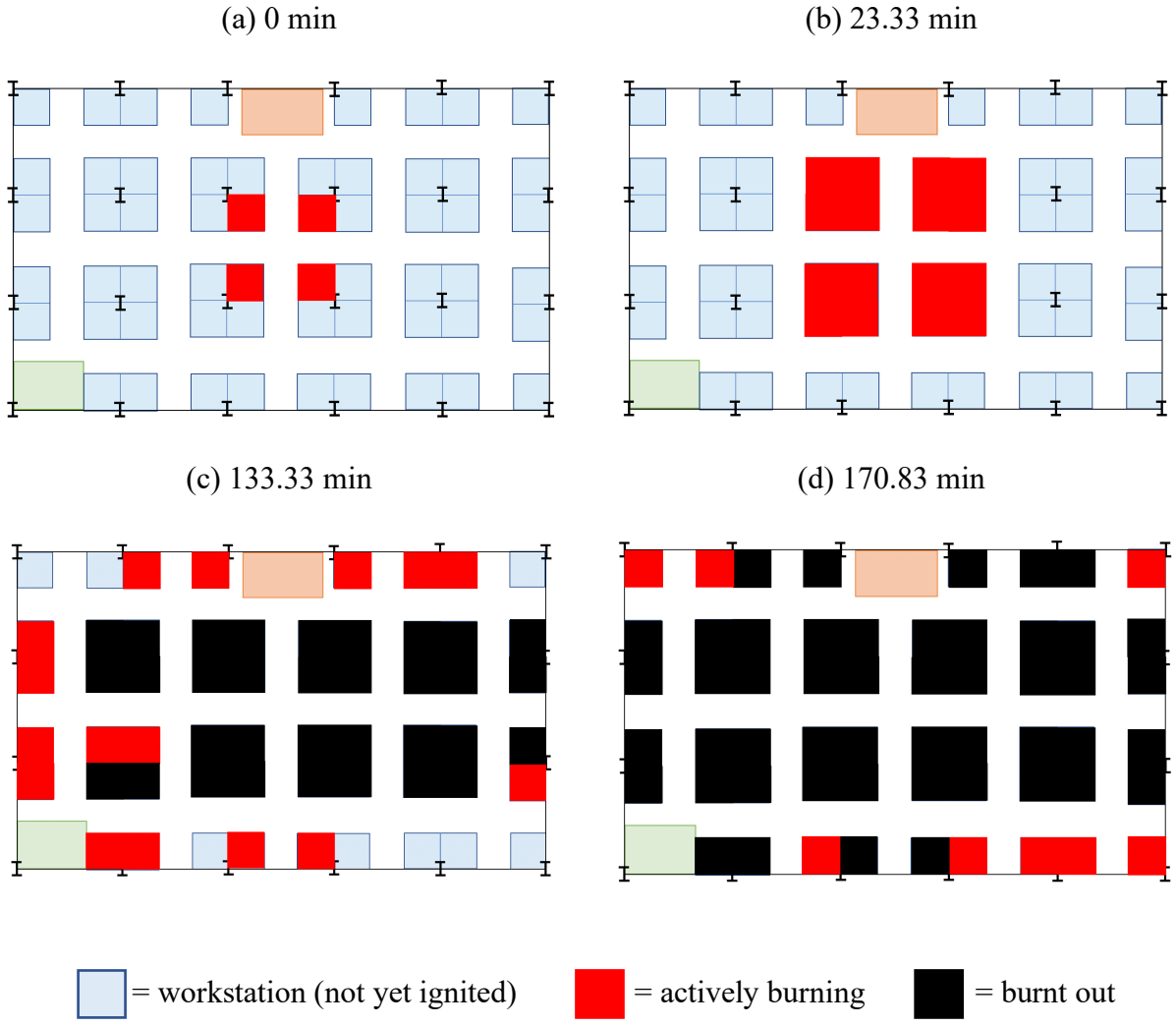

Figure 5.6 - Fire spread for cen331 simulation

In the corner ignition simulations, the fire began in the southeast corner of the floorplan. After ignition, the fire spread outward to the north and to the west. The fire spread for the corn331

simulation is presented below in Figure 5.7 by highlighting four separate time steps. The blue squares represent a workstation that has not yet ignited, the red squares represent workstations that are actively burning, and the black squares represent workstations that have burnt out (i.e., are no longer actively burning).

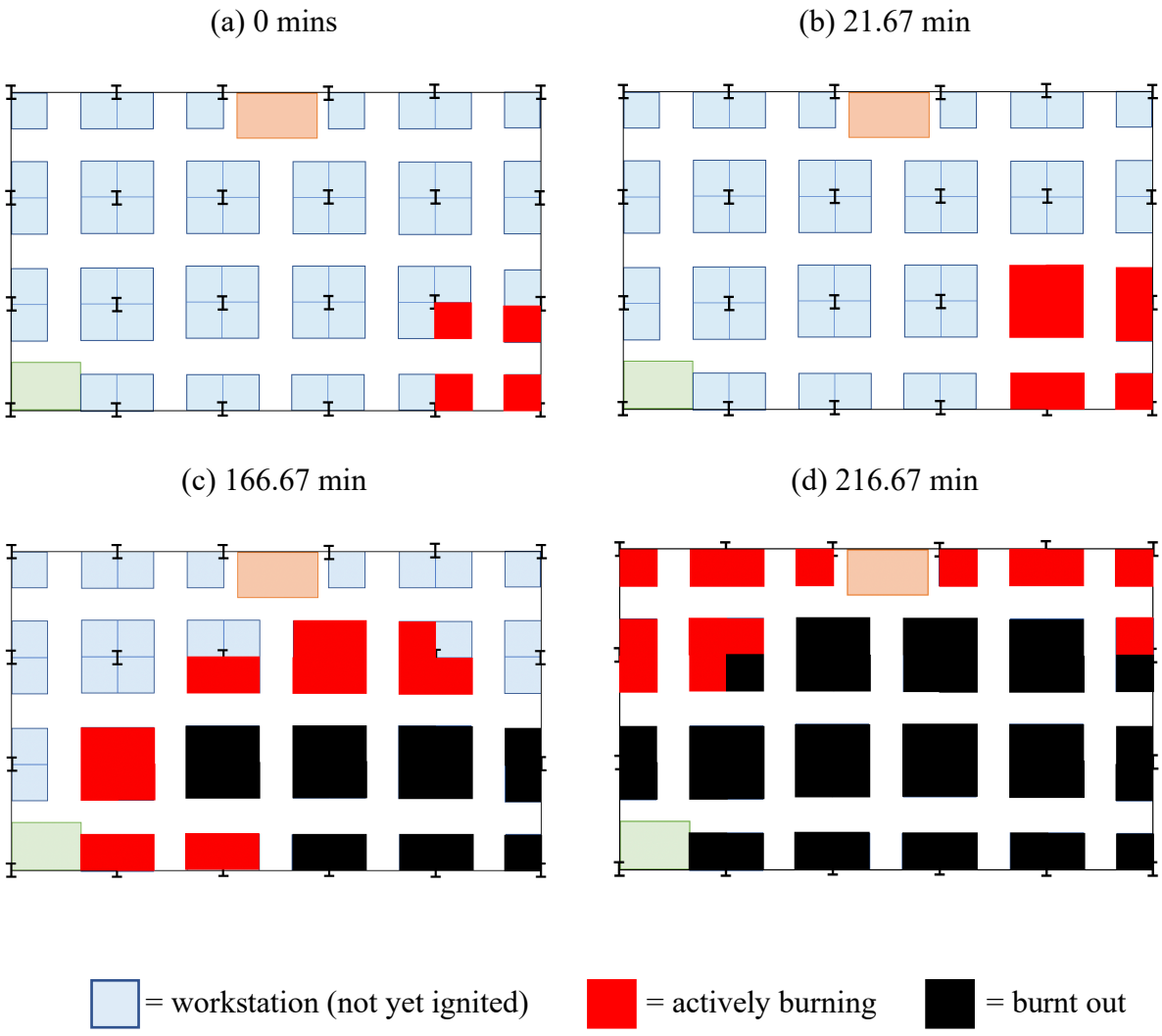

Figure 5.7 - Fire spread for corn331 simulation

In the perimeter ignition simulations, the fire began in the center of the south side of the floorplan. After ignition, the fire spread outward to the north, east and west. The fire spread for the perim331 simulation is presented below in Figure 5.8 by highlighting four separate time steps. The blue squares represent a workstation that has not yet ignited, the red squares represent

workstations that are actively burning, and the black squares represent workstations that have burnt out (i.e., are no longer actively burning).

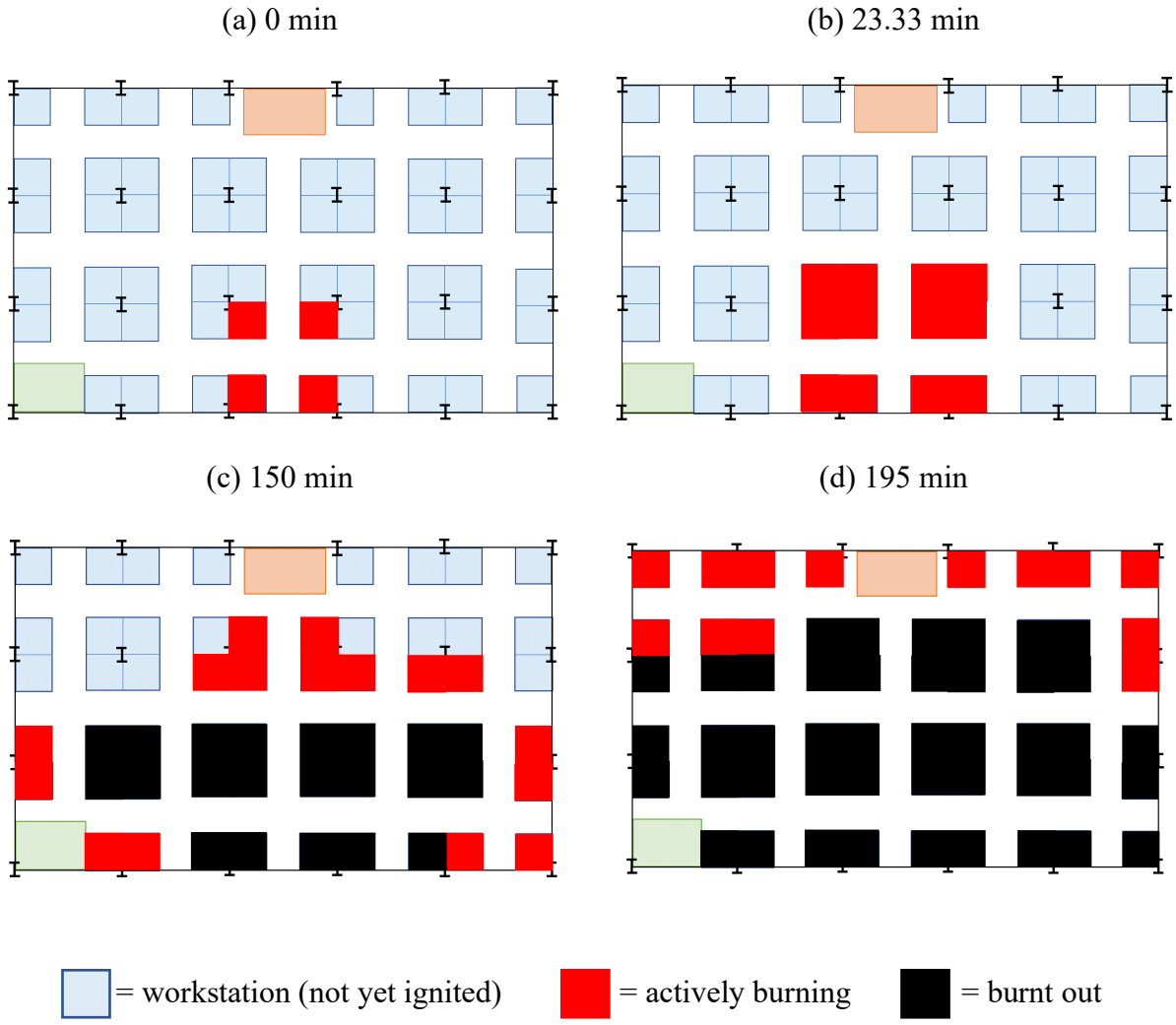

Figure 5.8 - Fire spread for perim331 simulation

The fastest fire spread occurred for the center ignition models and the slowest fire spread occurred for the corner ignition models. This is expected because the fire could spread initially in four directions for the center ignition model, and in only two directions for the corner ignition model. The perimeter ignition model could initially spread in three directions.

5.4.2 Ventilation Conditions and Flashover

The parametric study considered three different ventilation conditions in the compartment. The opening factors considered were 0.04, 0.145, and 0.25. These values were chosen to represent the lowest and highest possible opening factors for a compartment.

In this section, the effect of the ventilation conditions on beam temperature and fire duration is shown for all ignition locations. The heat release rate and the fuel load density are kept constant. The beam temperatures presented are recorded in the center of the bottom flange of an interior girder at the location indicated in Figure 5.9.

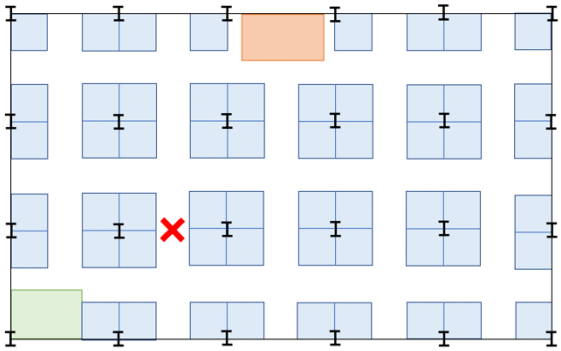

Figure 5.9 - Location of beam temperature measurement

Figure 5.10 presents the results for the center ignition location. As shown in the figure, the low ventilation model (opening factor = 0.04) resulted in significantly higher beam temperatures than the high ventilation model (opening factor = 0.25). The peak beam temperature at the measured location for the cen131 and the cen331 simulation is 365 °C and 192 °C, respectively. Therefore, decreasing the ventilation of the compartment increased the maximum beam temperature by 90%.

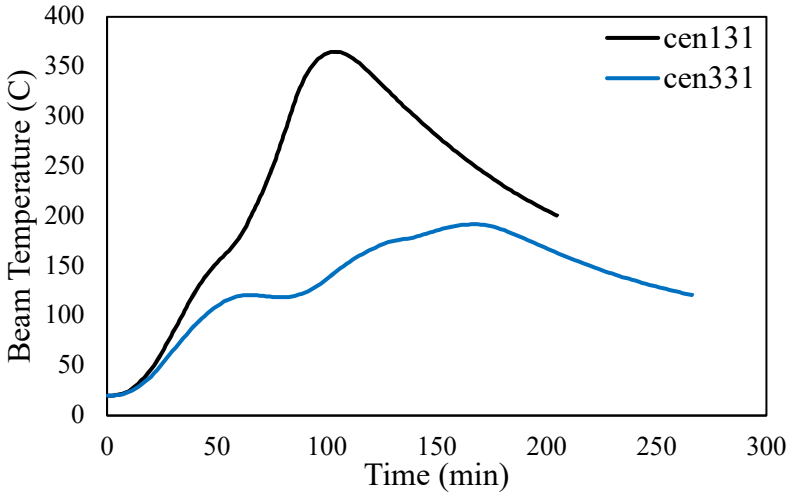

Figure 5.10 - Effect of ventilation condition of center ignition models

Figure 5.11 presents the results for the corner ignition location. As shown in the figure, the low ventilation model (opening factor = 0.04) again resulted in significantly higher beam temperatures than the high ventilation model (opening factor = 0.25). The peak beam temperature at the measured location for the corn131 and the corn331 simulation is 415 °C and 213 °C respectively. Therefore, decreasing the ventilation of the compartment increased the maximum beam temperature by 95%.

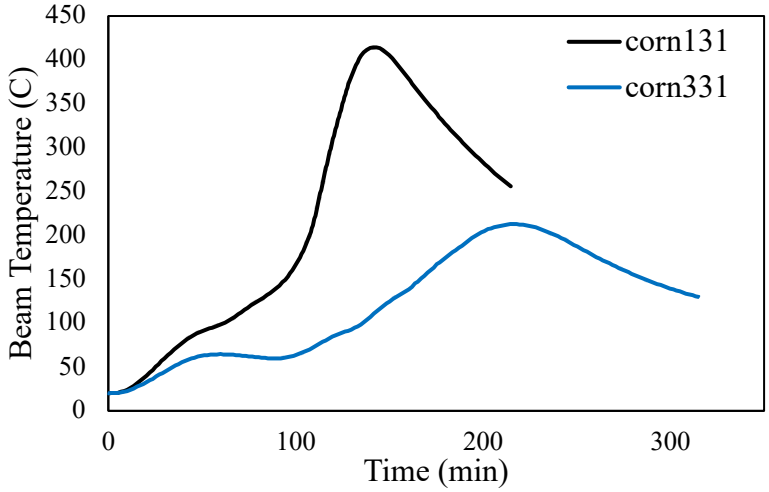

Figure 5.11 - Effect of ventilation condition on corner ignition models

Figure 5.12 presents the results for the perimeter ignition location. As expected, the low ventilation model (opening factor = 0.04) resulted in significantly higher beam temperatures than the high ventilation model (opening factor = 0.25). The peak beam temperature at the measured location for the corn131 and the corn331 simulation is 342 °C and 191 °C respectively. Therefore, decreasing the ventilation of the compartment increased the maximum beam temperature by 79%.

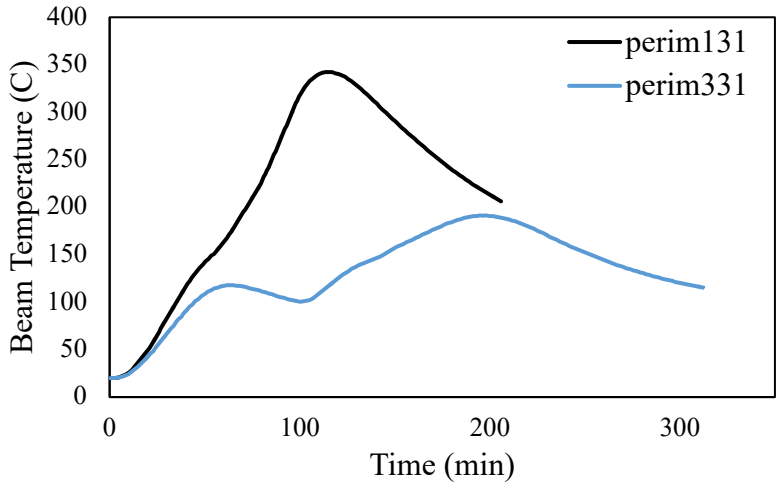

Figure 5.12 - Effect of ventilation condition on perimeter ignition models

Table 5.2 presents the effect of the ventilation condition on fire duration and on the spread rate of the fire along the length of the floorplan. The spread rate for the cen131 and the cen331 simulations are 0.338 m/min and 0.183 m/min, respectively. Therefore, decreasing the ventilation of the compartment increased the spread rate by 85% for the center ignition model. The spread rate for the corn131 and the corn331 simulations are 0.245 m/min and 0.152 m/min, respectively. This translates to a 61% increase in the fire spread rate when the ventilation condition is reduced for the corner ignition model. Lastly, the spread rate for the perim131 and the perim331 simulations is 0.300 m/min and 0.164 m/min, respectively. This represents an 83% increase in the fire spread rate when the ventilation condition is decreased for the perimeter ignition model.

Table 5.2 - Effect of ventilation condition on fire spread rate

Simulation	Fire Duration (min)	Spread Rate (m/min)
cen131	113	0.338
cen331	208	0.183
corn131	155	0.245
corn331	251	0.152
perim131	127	0.300
perim331	232	0.164

For all ignition locations, the low ventilation condition resulted in significantly increased beam temperatures and fire spread rates when compared to the higher ventilation condition. This can be explained by the onset of flashover in the low ventilation compartment. Flashover causes the objects in a compartment to ignite simultaneously, which can result in high structural temperatures and rapid fire spread rates. Flashover is defined by upper layer gas temperatures that exceeds 600 °C or heat flux at the floor level that exceeds 20 kW/m^2. For example, in the cen131 simulation, from 3580 s to 4340 s, the average gas temperature at the ceiling exceeded 600 °C, indicated that flashover may have occurred. Similar trends were seen in the low ventilation compartments for the corner and perimeter ignition cases.

5.4.3 Heat Release Rate of the Workstations

The parametric study considered three different heat release rates of the workstations: a 0%, 5% and 10% increase from the experimental data. This was done to reflect uncertainty in the contents and materials in the workstations.

In this section, the effect of the heat release rate of the workstations on beam temperature and fire duration is shown for all ignition locations. The ventilation conditions and the fuel load density are kept constant. The beam temperatures presented are recorded in the center of the bottom flange of an interior girder at the location indicated in Figure 5.9.

Figure 5.13 presents the effect of the heat release rate on the center ignition model. As shown in the figure, the higher heat release rate of the workstations (+10% of experimental data) resulted in higher beam temperatures than the lower heat release rate of workstations (+0% experimental data). The peak beam temperature at the measured location for the cen111 and the cen131 simulation is 321 °C and 365 °C respectively. Therefore, increasing the heat release rate of the workstations increased the maximum beam temperature by 14%.

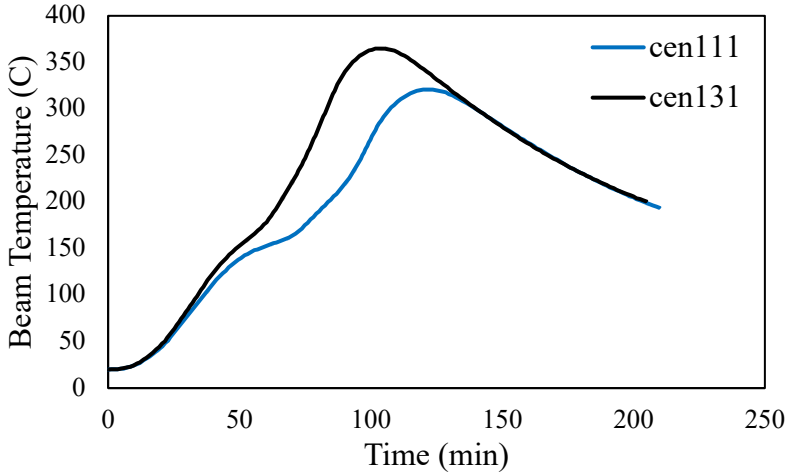

Figure 5.13 - Effect of heat release rate on center ignition models

Figure 5.14 presents the effect of the heat release rate on the corner ignition model. This figure shows the higher heat release rate of the workstations (+10% of experimental data) resulted in higher beam temperatures than the lower heat release rate of workstations (+0% experimental data). The peak beam temperature at the measured location for the corn111 and the corn131

simulation is 363 °C and 415 °C respectively. Therefore, increasing the heat release rate of the workstations increased the maximum beam temperature by 14%.

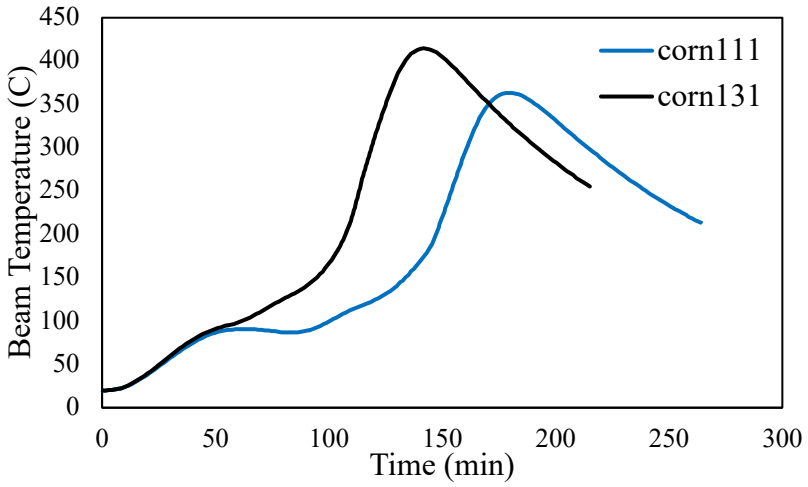

Figure 5.14 - Effect of heat release rate on corner ignition models

Figure 5.15 presents the effect of the heat release rate on the perimeter ignition model. As shown in the figure, the higher heat release rate of the workstations (+10% of experimental data) resulted in higher beam temperatures than the lower heat release rate of workstations (+0% experimental data). The peak beam temperature at the measured location for the perim111 and the perim131 simulation is 297 °C and 342 °C respectively. Therefore, increasing the heat release rate of the workstations increased the maximum beam temperature by 15%.

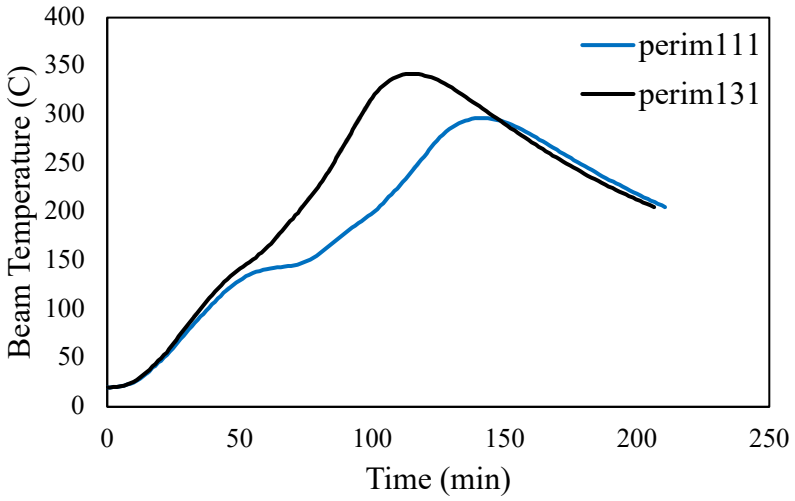

Figure 5.15 - Effect of heat release rate on perimeter ignition models

Table 5.3 presents the effect of the heat release rate of the workstations on the duration of the fire and on the spread rate of the fire along the length of the floorplan. The spread rate for the cen111 and the cen131 simulation is 0.293 m/min and 0.338 m/min, respectively. Therefore, increasing the heat release rate of the workstation by 10% increased the spread rate by 15% for the center ignition model. The spread rate for the corn111 and the corn131 simulation is 0.198 m/min and 0.245 m/min, respectively. This translates to a 24% increase in the fire spread rate when the heat release rate of the workstation is increased for the corner ignition model. Lastly, the spread rate for the perim111 and the perim131 simulations is 0.252 m/min and 0.300 m/min, respectively. This represents an 19% increase in the fire spread rate when the ventilation condition is decreased for the perimeter ignition model. For all models, increasing the heat release rate of the workstations resulted in an increased fire spread rate.

Table 5.3 - Effect of heat release rate on fire spread rates

Simulation	Fire Duration (min)	Spread Rate (m/min)
cen111	130	0.293
cen131	113	0.338
corn111	192	0.198
corn131	155	0.245
perim111	151	0.252
perim131	127	0.300

Increasing the heat release rate of the workstations by 10% caused the peak beam temperatures to increase approximately 15% on average, and the spread rate of the fire to increase by approximately 20% on average for all ignition locations studied. The average increase in the peak beam temperatures and the fire spread rate was larger than the increase in the heat release of the workstation in all cases studied.

5.4.4 Fuel Load Density

The parametric study considered two different fuel load densities in the compartment. The fuel load density of the compartment was varied from 385 MJ/m^2 to 696 MJ/m^2 to represent a range of possibilities. The compartment design with a lower fuel load density represents a typical furniture layout and is presented in Figure 5.1a. The higher fuel load density case is meant to represent a worst-case scenario and the layout is presented in Figure 5.1b.

In this section, the effect of increasing the fuel load density on beam temperature and fire duration is shown for the center and corner ignition locations considering both high and low ventilation conditions. The heat release rate of the workstations is kept constant. The beam

temperatures presented are recorded in the center of the bottom flange of an interior girder at the location indicated in Figure 5.9.

Figure 5.16 presents the effect of the fuel load density for the center ignition model with low ventilation. As shown in the figure, the higher fuel load density (696 MJ/m^2) resulted in significantly higher temperatures than the lower fuel load density (385 MJ/m^2). The peak beam temperature at the measured location for the cen131 and the cen132 simulation is 365 °C and 619 °C, respectively. Therefore, increasing the fuel load density of the compartment increased the maximum beam temperature by 70%. It should be noted here that beam temperatures exceeding 500 °C are considered to be structurally significant and may indicate failure of the beam in the cen132 simulation.

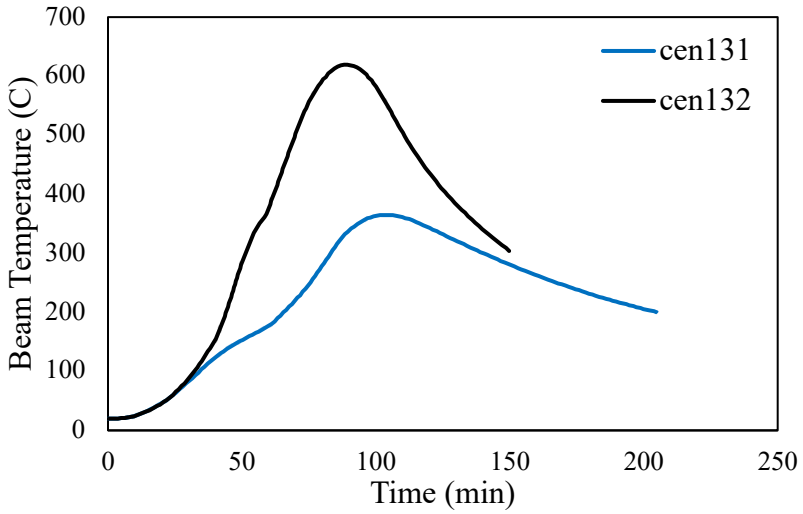

Figure 5.16 - Effect of heat release rate on center ignition and low ventilation model

Figure 5.17 presents the effect of the fuel load density for the corner ignition model with low ventilation. As shown in the figure, the higher fuel load density (696 MJ/m^2) resulted in significantly higher temperatures than the lower fuel load density (385 MJ/m^2). The peak beam temperature at the measured location for the cen131 and the cen132 simulation is 415 °C and 797 °C, respectively. Therefore, increasing the fuel load density of the compartment increased the

maximum beam temperature by 92%. Again, it should be noted here that structural temperatures exceeding 500 °C are considered to be structurally significant and may indicate failure of the beam in the corn132 simulation.

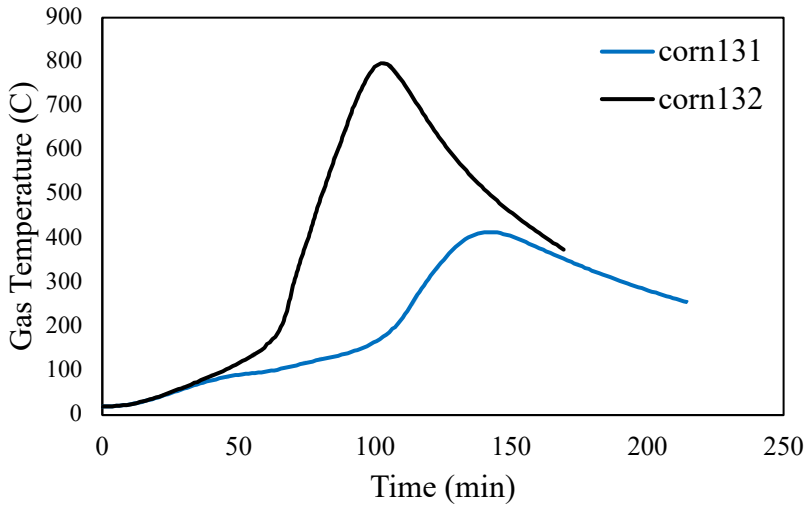

Figure 5.17 - Effect of fuel load density on center ignition and low ventilation model

Figure 5.18 presents the effect of the fuel load density for the center ignition model with high ventilation. As shown in the figure, the higher fuel load density (696 MJ/m^2) resulted in significantly higher temperatures than the lower fuel load density (385 MJ/m^2). The peak beam temperature at the measured location for the cen331 and the cen332 simulation is 192 °C and 381 °C, respectively. Therefore, increasing the fuel load density of the compartment increased the maximum beam temperature by 98%.

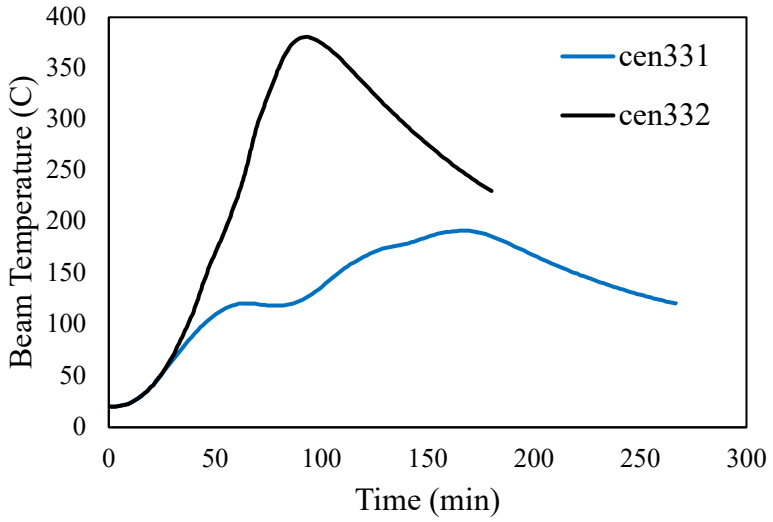

Figure 5.18 - Effect of fuel load density on center ignition and high ventilation model

Figure 5.19 presents the effect of the fuel load density for the corner ignition model with high ventilation. As shown in the figure, the higher fuel load density (696 MJ/m^2) resulted in significantly higher temperatures than the lower fuel load density (385 MJ/m^2). The peak beam temperature at the measured location for the corn331 and the corn332 simulation is 213 °C and 453 °C, respectively. Therefore, increasing the fuel load density of the compartment increased the maximum beam temperature by 113%.

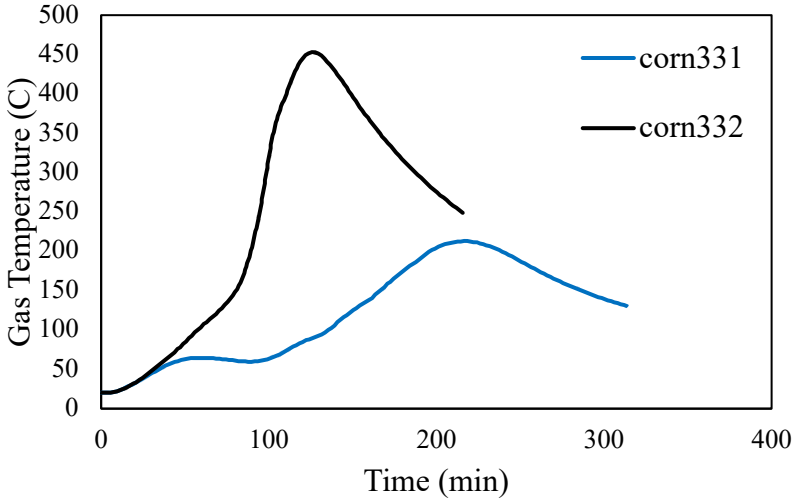

Figure 5.19 - Effect of fuel load density on center ignition and high ventilation model

Table 5.4 presents the effect of the fuel load density on the duration of the fire and on the spread rate of the fire along the length of the floorplan. The spread rate for the cen131 and cen132 simulations are 0.338 m/min and 0.420 m/min respectively. This reflects a 24% increase in the fire spread for the higher fuel load density. The spread rate for the cen331 and cen332 simulations are 0.183 m/min and 0.317 m/min respectively, representing a 73% increase in the spread rate as a result of the increased fuel load density. The spread rate for the corn131 and corn132 simulations are 0.245 m/min and 0.348 m/min, respectively. Therefore, increasing the fuel load density caused the spread rate of the fire to increase 42% for this simulation. The spread rate for the corn331 and corn332 simulations were 0.152 m/min and 0.243 m/min, respectively. This reflects a 60% increase in the fire spread rate when considering the increased fuel load density. For all models, the increased fuel load density resulted in an increased fire spread rate.

Table 5.4 - Effect of fuel load density on fire spread rates

Simulation	Fire Duration (min)	Spread Rate (m/min)
cen131	113	0.338
cen132	91	0.420
cen331	208	0.183
cen332	120	0.317
corn131	155	0.245
corn132	109	0.348
corn331	251	0.152
corn332	157	0.243

Increasing the fuel load density resulted in a more extreme thermal environment in the compartment for all simulations studied, as expected. The increased fuel load density had a significant impact and resulted in higher beam temperatures and increased fire spread rates. The two cases studied in this section with low ventilation conditions and high fuel load density (cen132 and corn132) experienced structurally significant heating that may indicate failure.

5.4.5 Gas Temperature

The gas temperatures at the ceiling of the compartment were analyzed to show how the spread of fire affected the thermal environment. The gas temperatures are presented along the length of one of the interior girders in the compartment at the location indicated by the red line in Figure 5.20.

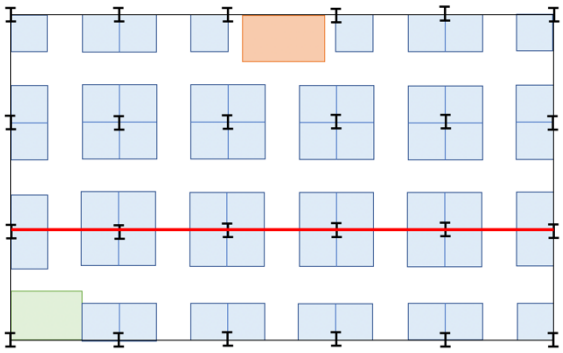

Figure 5.20 - Location of gas temperature measurements

Figure 5.21 presents the gas temperature results for the corn131 simulation. At 560 s, the maximum gas temperature is 995 °C and the minimum temperature is 225 °C, resulting in a 700 °C temperature exposure differential along the girder. At 7020 s, the maximum gas temperature is 1003 °C and the minimum temperature is 397 °C, resulting a temperature differential of 606 °C along the girder.

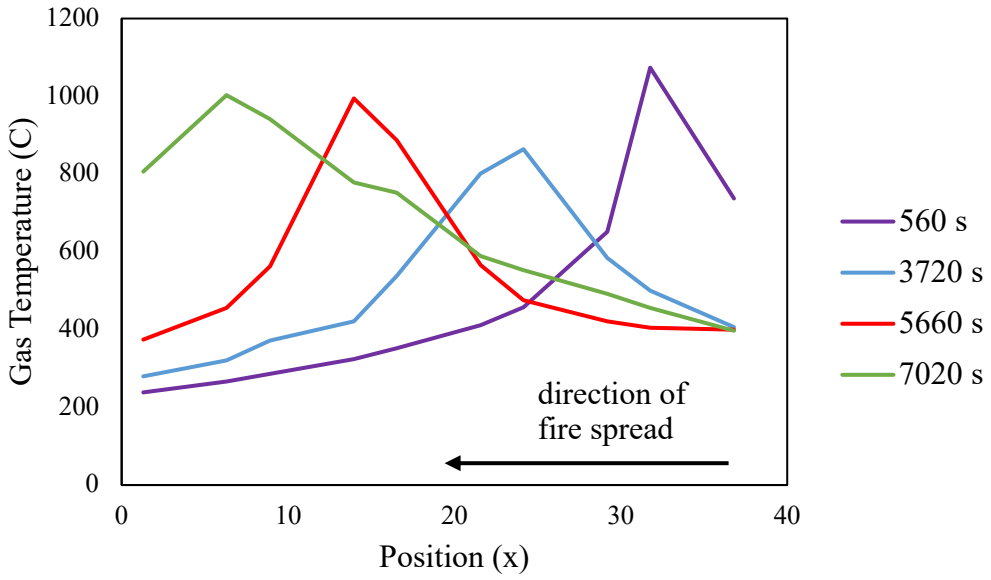

Figure 5.21 - Gas temperature results for the corn131 simulation

Figure 5.22 presents the gas temperature results for the corn331 simulation. At 540 s, the maximum gas temperature is 930 °C and the minimum temperature is 158 °C, resulting in a 772 °C temperature exposure differential along the beam. At 9540 s, the maximum gas temperature is 746 °C and the minimum temperature is 213 °C, resulting a temperature differential of 533 °C along the beam.

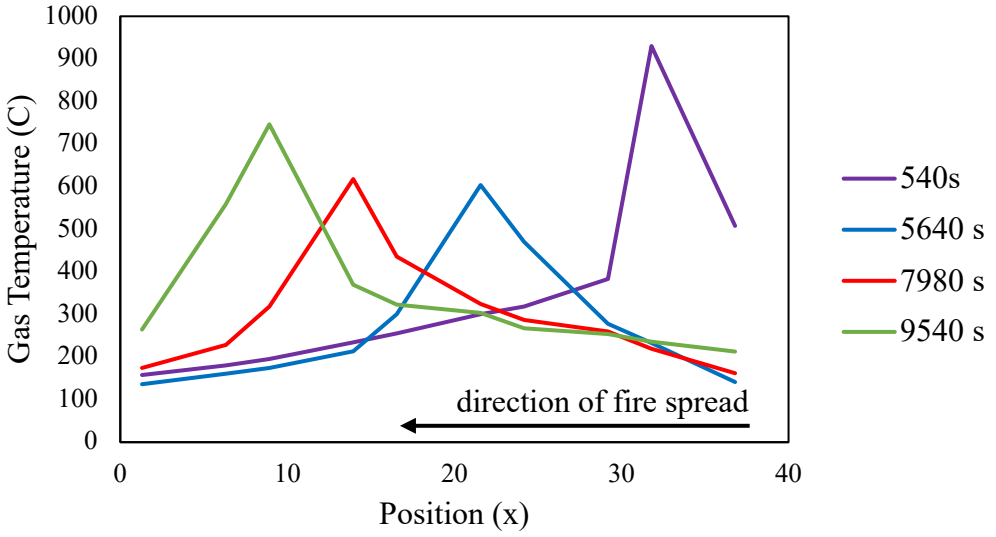

Figure 5.22 - Gas temperature results for the corn331 simulation

Figure 5.23 presents the gas temperature results for the corn132 simulation. At 1500 s, the maximum gas temperature is 913 °C and the minimum temperature is 309 °C, resulting in a 604 °C temperature exposure differential along the beam. At 4120 s, the maximum gas temperature is 942 °C and the minimum temperature is 635 °C, resulting a temperature differential of 307 °C along the beam.

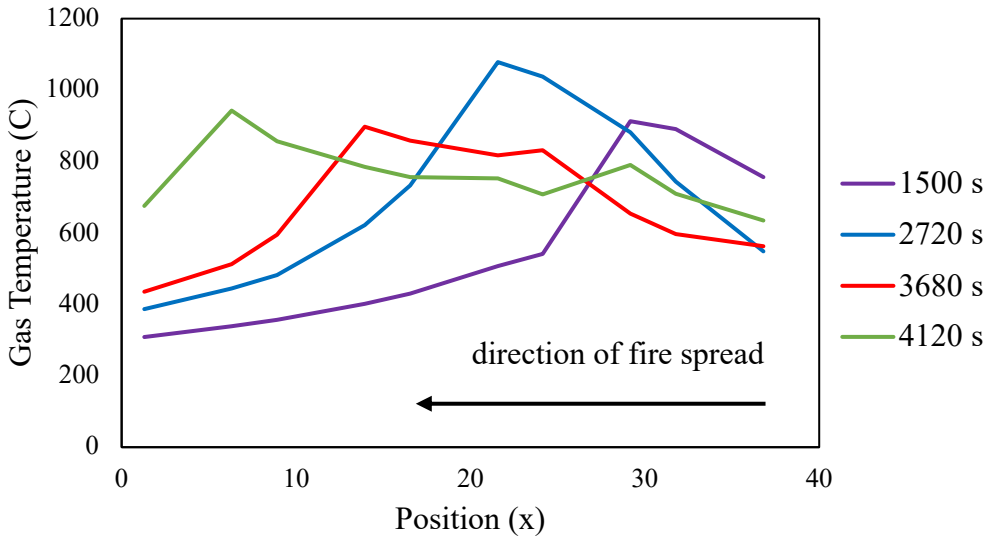

Figure 5.23 - Gas temperature results for the corn132 simulation

Figure 5.24 presents the gas temperature results for the corn332 simulation. At 1200 s, the maximum gas temperature is 930 °C and the minimum temperature is 229 °C, resulting in a 674 °C temperature exposure differential along the beam. At 5920 s, the maximum gas temperature is 1031 °C and the minimum temperature is 354 °C, resulting a temperature differential of 677 °C along the beam.

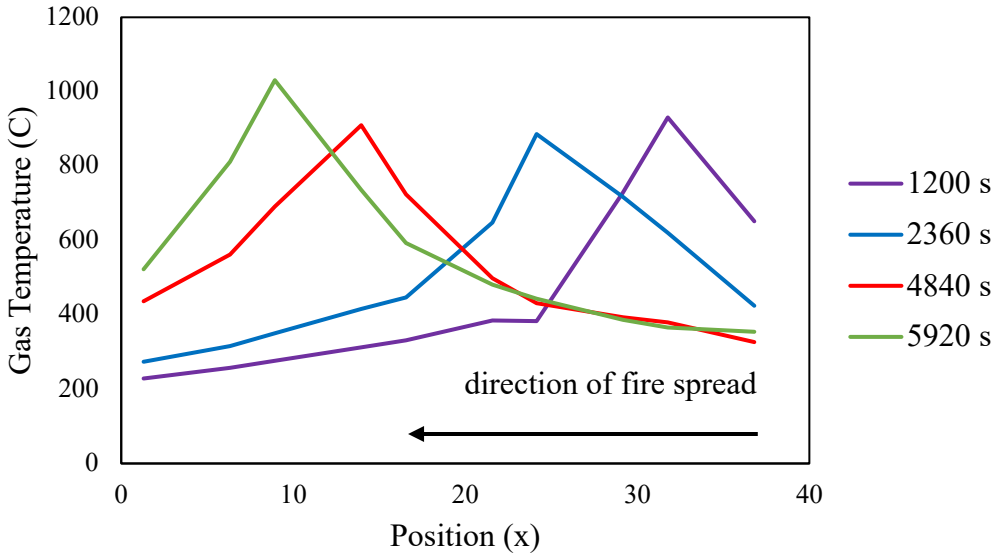

Figure 5.24 - Gas temperature results for the corn332 simulation

Figure 5.25 presents the gas temperature results for the cen131 simulation. At 1200 s, the maximum gas temperature is 1100 °C and the minimum temperature is 311 °C, resulting in a 789 °C temperature exposure differential along the beam. At 4140 s, the maximum gas temperature is 1086 °C and the minimum temperature is 575 °C, resulting a temperature differential of 511 °C along the beam.

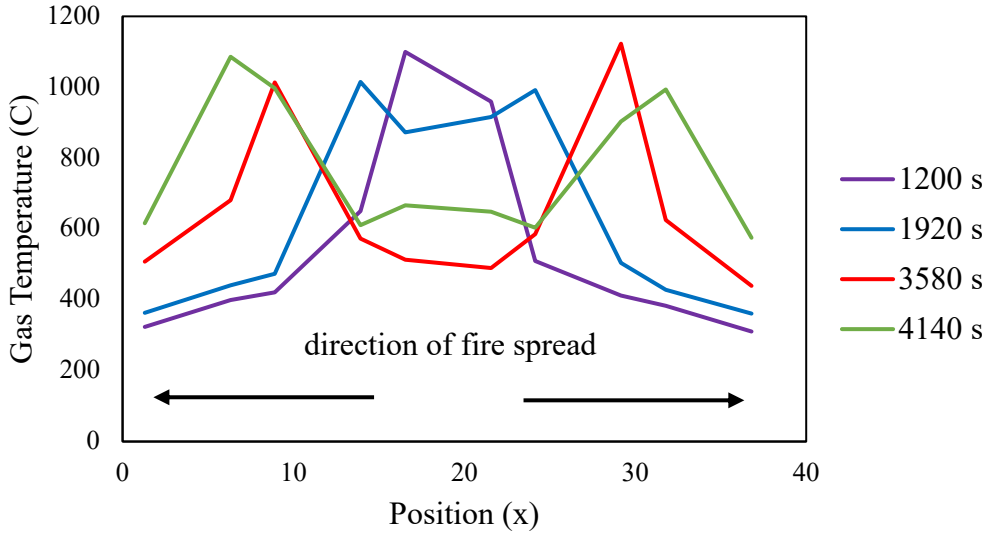

Figure 5.25 - Gas temperature results for the cen131 simulation

Figure 5.26 presents the gas temperature results for the cen331 simulation. At 1160 s, the maximum gas temperature is 700 °C and the minimum temperature is 202 °C, resulting in a 499 °C temperature exposure differential along the beam. At 5820 s, the maximum gas temperature is 765 °C and the minimum temperature is 250 °C, resulting a temperature differential of 515 °C along the beam.

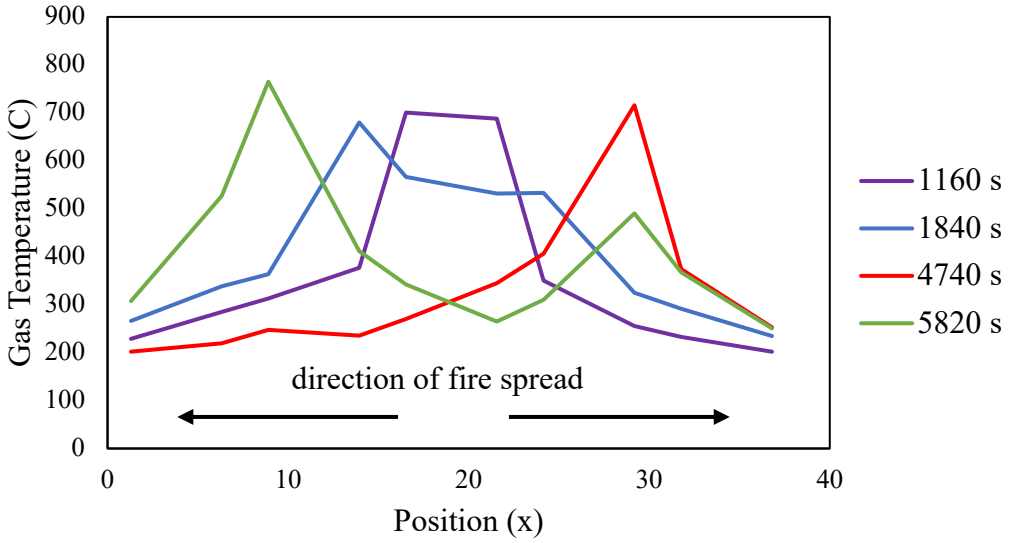

Figure 5.26 - Gas temperature results for the cen331 simulation

Figure 5.27 presents the gas temperature results for the cen132 simulation. At 1260 s, the maximum gas temperature is 1091 °C and the minimum temperature is 205 °C, resulting in a 886 °C temperature exposure differential along the beam. At 3080 s, the maximum gas temperature is 972 °C and the minimum temperature is 405 °C, resulting a temperature differential of 567 °C along the beam.

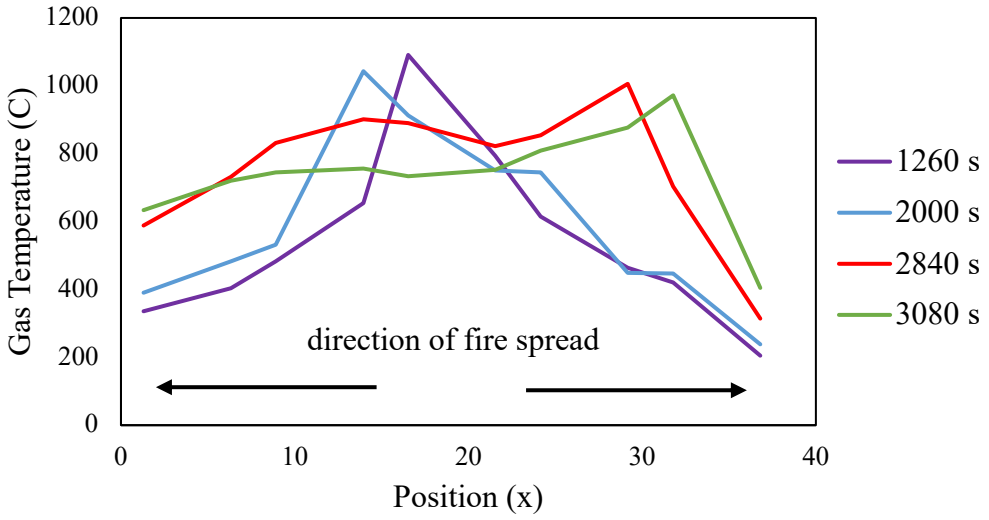

Figure 5.27 - Gas temperature results for the cen132 simulation

Figure 5.28 presents the gas temperature results for the cen332 simulation. At 2480 s, the maximum gas temperature is 824 °C and the minimum temperature is 354 °C, resulting in a 470 °C temperature exposure differential along the beam. At 4000 s, the maximum gas temperature is 970 °C and the minimum temperature is 551 °C, resulting a temperature differential of 419 °C along the beam.

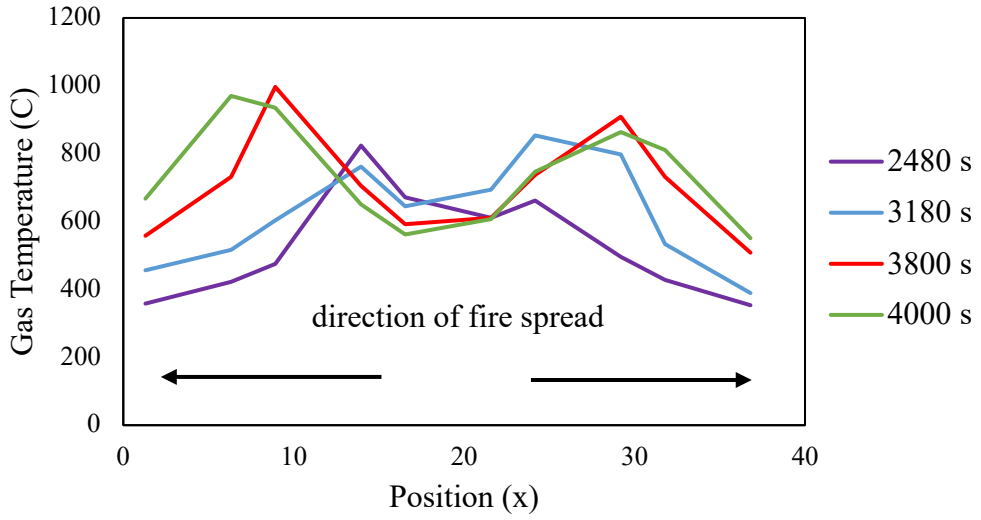

Figure 5.28 - Gas temperature results for the cen332 simulation

Generally, as the fire progressed, the temperature gradient in the thermal exposure of the beam decreased, with the exception of the corn332 and the cen331 simulations. The figures also demonstrated that in the corner ignition scenario, the fire spread in one direction along the length of the compartment and in the center ignition scenario, the fire spread in two directions along the length of the compartment. For the corner ignition simulations, at the beginning of fire spread, the corn331 simulation had the largest temperature gradient of 772 °C, and the corn132 simulation had the smallest temperature gradient of 604 °C. At the end of fire spread, the corn332 simulation had the largest temperature gradient of 677 °C, and the corn132 simulation had the smallest temperature gradient of 307 °C. For the center ignition simulations, at the beginning of fire spread, the cen132 simulation had the largest temperature gradient of 886 °C and the cen332 simulation has the cen332 simulation had the smallest temperature gradient of 470 °C. At the end of fire spread, the cen132 simulation had the largest temperature gradient of 567 °C, and the cen332 simulation had the smallest temperature gradient of 419 °C.

5.5 Comparison to the Traveling Fire Model (TFM)

5.5.1 Gas Temperatures

In the traveling fire model (TFM), the thermal field is divided into two distinct regions, the near field and the far field [1] [23]. The near field represents the portion of the compartment that is actively burning and where structural members are exposed to direct flame contact. The far field represents the rest of the compartment, which is being heating by hot convective gases. TFM assumes gas temperatures in the near field are uniformly 1200 °C, which is meant to represent a worst-case scenario [74]. The far-field gas temperatures are represented by Alpert's ceiling jet correlation [25]. The traveling fire model has been criticized for assuming simplistic fire dynamics, one-dimensional fire spread, and the used of Alpert's ceiling jet correlation has been questioned because it does not consider an accumulated smoke layer.

The fire spread model for large compartments models detailed fire dynamics through the use of computational fluid mechanics and the transient flux-time product model to accurately predict fire progression. It also includes an accumulated smoke layer. In this section, the fire spread model for large compartments and the traveling fire model will be compared to assess its accuracy in modeling the thermal environment for large compartments during a fire event.

Figure 5.29 presents the gas temperature variation along the length of an interior girder at the beginning of the fire as modeled by TFM and compared to the corn131, corn331, corn132, and corn332 simulations. The location of the presented gas temperatures is shown in Figure 5.20. As shown in Figure 5.29, TFM predicts higher gas temperatures along the entire length of the interior girder than the fire spread model for large compartments. In the early stages of the fire, this shows that TFM provides a conservative model of the gas temperatures in the near field and the far field.

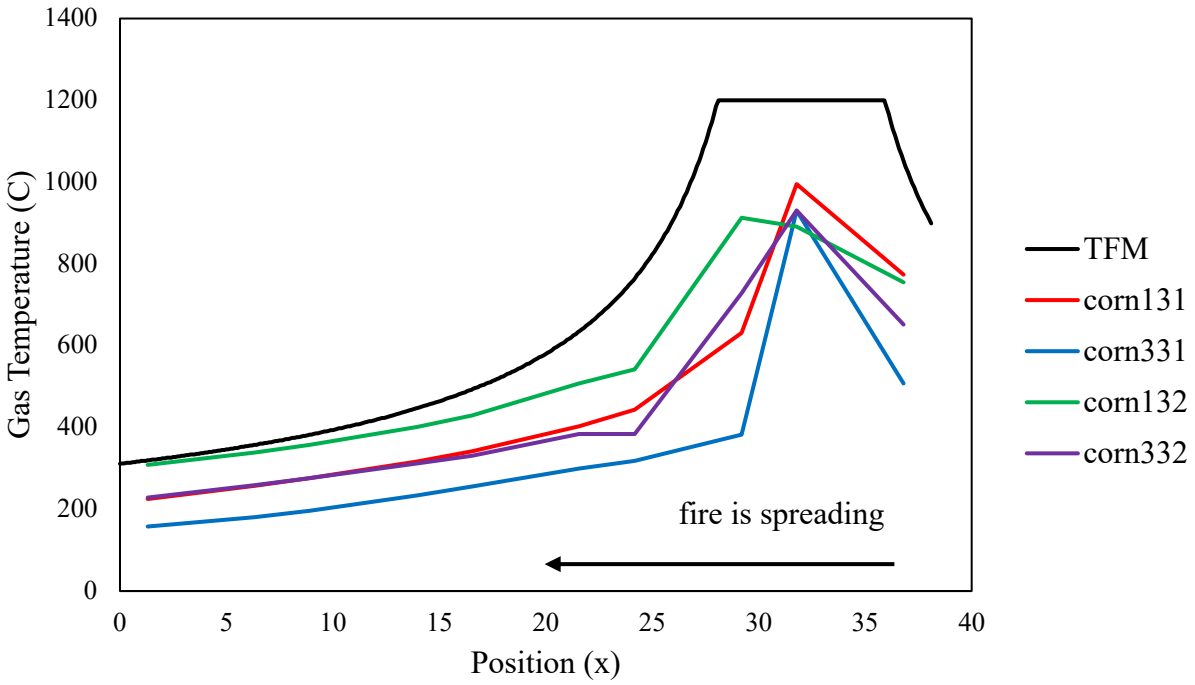

Figure 5.29 - Gas temperature comparison at the beginning of fire spread (length of compartment)

Figure 5.30 presents the gas temperature variation along the length of one interior girder line at the end of the fire as modeled by TFM and compared to the corn131, corn331, corn132, and corn332 simulations. The location of the presented gas temperatures is shown in Figure 5.20. As shown in Figure 5.30, in the near field TFM predicts higher gas temperatures than the fire spread model for large compartments, but in the far field, it underpredicts the gas temperatures when compared to the corn131, and the corn132 models. Both of these simulations model low ventilation conditions. This shows that during the later stages of a fire, TFM may not be a conservative model for gas temperatures in low ventilation compartments. It should be noted that TFM is intended to model fuel-controlled fires not ventilation-controlled fires.

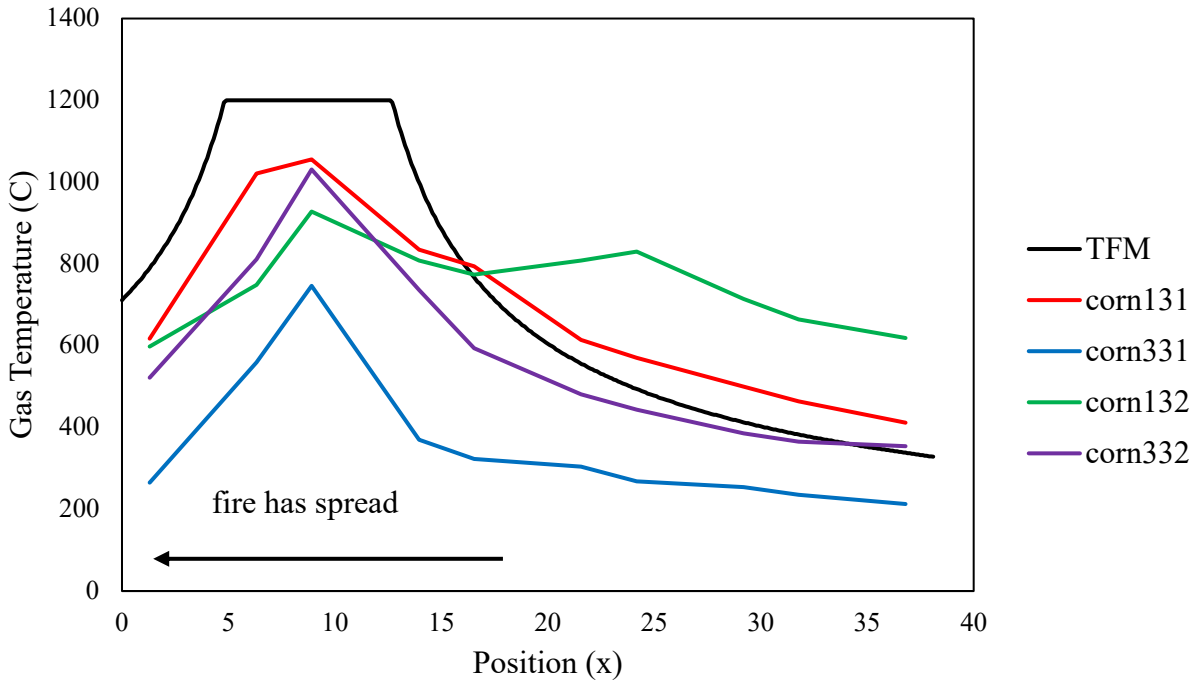

Figure 5.30 - Gas temperature comparison at the end of fire spread (length of compartment)

The traveling fire model (TFM) only considers one-dimensional fire spread along the length of a compartment, meaning that it assumes uniform gas temperatures along the width of this compartment. The fire spread model for large compartments using a transient flux-time product model for ignition, considers two-dimensional fire spread. To demonstrate the importance of considering two-dimensional fire spread, Figures 5.32 and 5.33, present the temperature gradients that occur through the width of the compartment during the corner ignition scenario.

Figure 5.31 presents the location of the gas temperature measurements for Figures 5.32 and 5.33. The gas temperatures were recorded along the length of one of the interior beams in the compartment at the location indicated by the red line.

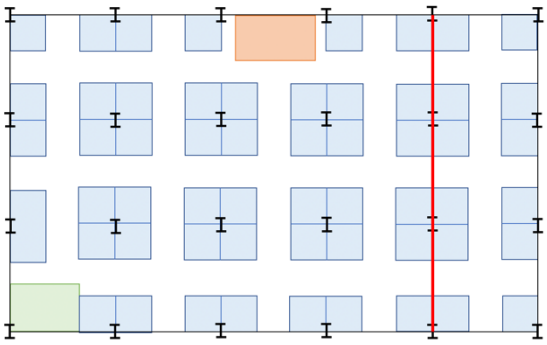

Figure 5.31 - Location of gas temperature measurements

Figure 5.32 presents the gas temperature variation along the width of the compartment in the beginning of the fire for the corn131, corn331, corn132, and corn332 simulations. The corn132 simulation experienced the largest temperature gradient of 755 °C, and the corn131 simulation experienced the smallest temperature gradient of 678 °C. Even the smallest temperature gradient experienced by the beam early in fire spread is significant here and should be considered by a design fire model.

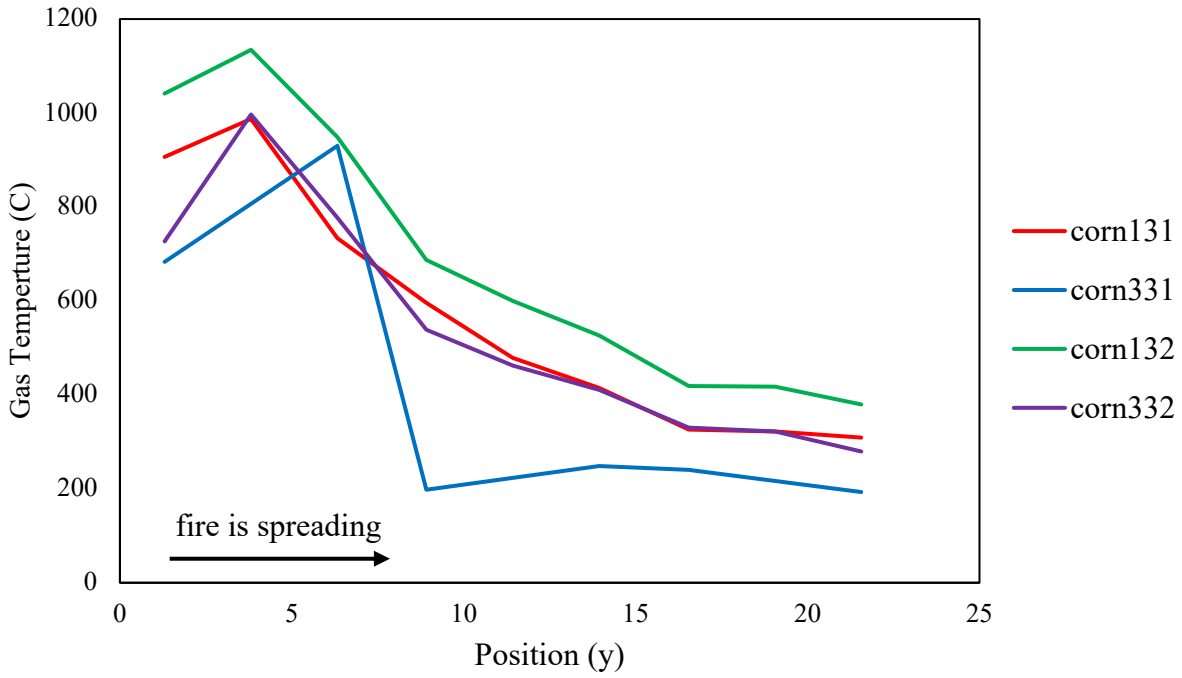

Figure 5.32 - Gas temperature comparison at the beginning of fire spread (width of the compartment)

Figure 5.33 presents the gas temperature variation along the width of the compartment at the end of fire spread for the corn131, corn331, corn132, and corn332 simulations. The corn131 simulation experienced the largest temperature gradient of 656 °C, and the corn132 simulation experienced the smallest temperature gradient of 298 °C. The temperature gradient experienced by the beam decreased in all four of the simulations presented from its value at the beginning of fire spread. The value of the thermal gradient at the end of fire spread is still significant and cannot be accurately represented by a uniform gas temperature as it would be treated in TFM.

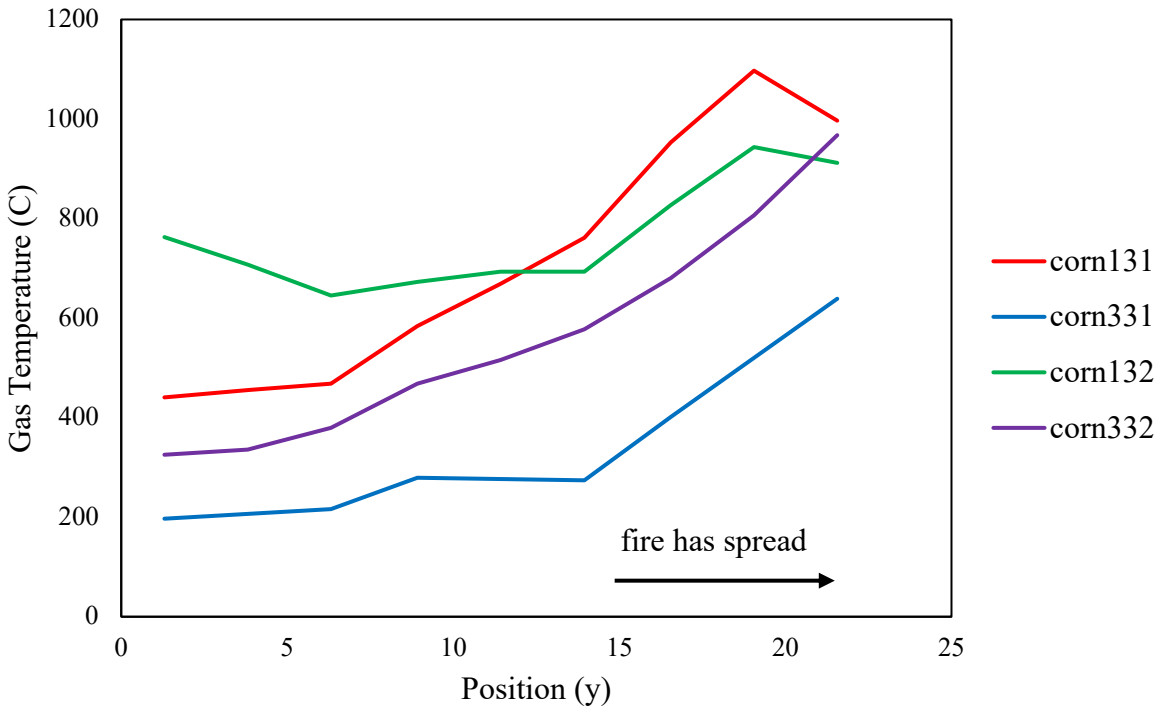

Figure 5.33 - Gas temperature comparison at the end of fire spread (width of compartment)

5.5.2 Fire Spread Rate

Table 5.5 compares the fire spread rates from the traveling fire model to the fire spread rate results from the fire spread model for large compartments. TFM predicts that a fire size equal to 5% of the floor area will spread at a rate of 0.11 m/min, a 10% fire size will spread at 0.22 m/min and a 25% fire size will spread at a rate of 0.55 m/min. The fire modeled by the fire spread model for large compartments grew and shrank during the duration of the fire so it cannot be defined by a single fire size, but generally the fire spread rates of this model correlated to fire spread rates for a 5-25% size fire in TFM. Overall, this shows that TFM provides reasonable predictions of the fire spread rate.

Table 5.5 - Fire spread rate comparison

Simulation	Fire Duration (min)	Spread Rate (m/min)	Comparison to TFM
cen131	113	0.338	10-25% fire size
cen132	91	0.420	10-25% fire size
cen331	208	0.183	5-10% fire size
cen332	120	0.317	10-25% fire size
corn131	155	0.245	10% fire size
corn132	109	0.348	10-25% fire size
corn331	251	0.152	5-10% fire size
corn332	157	0.243	10% fire size

5.6 Conclusions

In this work, a parametric study was performed to understand the range of thermal environments that can occur in large compartments during a fire event. This parametric study utilized the fire spread model for large compartments using a transient flux-time product model for ignition. This method provides the most detailed model of the thermal environment for large compartments. It models realistic fire dynamics using computational fluid mechanics and the transient flux-time product for ignition models realistic fire progression through the compartment. The goal of the parametric study was to characterize the range of thermal conditions that can occur in large compartments to help inform designers regarding the range of the conditions that a structure may experience under fire exposure. This was accomplished by varying the ignition location of the fire, the ventilation conditions, the heat release rate of the workstations, and the fuel load density. The corner ignition location resulted in the longest fire duration. The low ventilation

condition, the higher heat release rate of the workstations, and the higher fuel load density resulted in the highest structural temperatures and fastest fire spread rates. Overall, the ventilation conditions and the fuel load density had the more significant impact on structural temperatures and fire duration. Additionally, this study showed that well-ventilated compartments experienced larger temperature gradients along the length of an interior girder during the fire event.

The results of the parametric study using the fire spread model for large compartments with a transient flux-time product model for ignition were compared to the traveling fire model (TFM). It showed that the traveling fire model generally provided a conservative estimate of gas temperatures, expect in low ventilation compartments. In low-ventilation compartments, this study showed that the far field temperatures may be underpredicted by TFM in the later stages of heating. Structural fire engineers should consider the results presented in this study when designing fire protection for large compartments with low ventilation. TFM assumes a uniform temperature through the width of the compartment and the results of this study showed that when realistic two-dimensional fire spread is considered, significant temperature gradients can occur. This could affect the structural performance of the floor system. This study also showed that TFM provides reasonable predictions of fire spread rate. Note that TFM only captures 1D fire spread and therefore does not account for effects that may be significant for 2D fire spread.

Chapter 6 Conclusion and Future Work

6.1 Summary and Conclusions

The behavior of fire in large open-plan compartments is currently not well understood. This led to inadequate structural performance during accidental fires that occurred in buildings with open-plan layouts [4-11]. As open-plan compartments and large atriums become more common in architectural design, it is important to be able to accurately model and characterize this type of fire behavior. The goal of this body of work is to (1) improve thermal and structural modeling of compartments during traveling fire events and (2) use these improved modeling techniques to characterize the range of possible thermal environments that a compartment can experience during a traveling fire. The purpose of this work is to aid engineers in designing effective fire protection for large compartments.

To improve thermal and structural modeling of compartments under localized burning, Chapter 3 of this dissertation presented guidelines on how to represent the boundary condition at the structure-fire interface. Studies have suggested that the assumption of uniform heating often used in structural fire engineering cannot be assumed to be conservative. Computational fluid dynamics (CFD) provides the most detailed and accurate model of fire dynamics, and this can be coupled with a finite element (FE) model of a structure through the representation of the boundary conditions in order to analyze its thermal and mechanical response. There is a wide range of methods and parameters that are used when determining the boundary condition at the fire-structure interface and the main inconsistencies are related to the representation of solid

temperatures, the convective heat transfer coefficient, and the surface emissivity of steel. The purpose of this work was to investigate the existing methods for accuracy and computational efficiency and then to identify best practices to guide researchers in the complicated CFD-FE analysis of structures in fire. This study also aimed to show the impact that certain modeling assumptions can have on the prediction of structural response. The main conclusions of the study were that (1) the solid temperatures should be represented by the finite element prediction of surface temperature; (2) the heat transfer coefficient for a localized fire scenario cannot be accurately represented by a constant value; the heat transfer coefficient can vary significantly over the structural member and therefore, when possible, a spatially and temporally varying heat transfer coefficient determined by the CFD code should be used; and (3) a surface emissivity value of 0.9 should be used for localized fire scenarios of steel structures modeled using a coupled CFD-FE approach. The results and recommendations of this study provided guidance for representing the boundary conditions at the structure-fire interface for the coupled CFD-FE analyses performed in this dissertation.

The fire spread model for large compartments using a transient flux-time product for ignition was presented in Chapter 4. This work improved fire modeling for structural application and allowed for the study of traveling fires in large open-plan compartments. In this fire spread framework, the fuel load for an office building, was made up of clusters of workstations that were arranged in a realistic pattern on the floor plan. The fire began with the assumed ignition of an object. Detailed fire dynamics were modeled using computational fluid dynamics (CFD), which allows the user to specify exact compartment parameters, such as the compartment size, wall lining, ventilation conditions, and fuel load distribution. To reduce computational expense, each object (e.g., workstation) was represented by a burner that has a heat release rate equivalent to a

complete workstation, as determined by experimental tests. The fire was allowed to spread realistically from object to object through the use of a transient flux-time product ignition model. The improved flux-time product ignition model was derived to predict ignition under time-varying heat flux exposure and only requires well-documented material properties for implementation. This chapter presented validation of the equivalent burner assumption, the transient flux-time product ignition model, and the fire spread model for large compartments using experimental data from NIST [2]. The proposed fire spread model for large compartments aimed to provide designers with a realistic model of fire behavior in large compartments, including detailed fire dynamics and two-dimensional fire spread, to aid them in the design of resilient structures in fire while balancing accuracy with computational efficiency.

The fire spread model for large compartments using a transient flux-time product for ignition was used in Chapter 5 to improve understanding of the behavior of traveling fires. A parametric study was conducted to compile data and inform designers on the full range of thermal environments that can occur when a large compartment experiences a traveling fire event. In this study various features of the compartment characteristics and fire characteristics were varied, including fire origin, ventilation conditions, heat release rate of the workstations, and fuel load density. Additionally, the range of gas temperature results and burning durations predicted in the parametric study of the fire spread model were compared to that predicted by an existing fire model, the traveling fire model (TFM), to determine if a realistic thermal environment was represented in the simplified design models when compared to the CFD simulations and to determine if there were aspects of the fire response that are not captured by simplified models. The results of the parametric study showed that the corner ignition location resulted in the longest fire duration. In addition, the low ventilation condition, the higher heat release rate of the workstations,

and the higher fuel load density resulted in the highest structural temperatures and the fastest fire spread rates. The ventilation conditions and the fuel load density produced a more significant impact on structural temperatures and fire duration. When compared the TFM, it was found that TFM generally provided a conservative estimate of gas temperatures, except in low ventilation compartments. In low-ventilation compartments, this study showed that the far field temperatures may be underpredicted by TFM in the later stages of heating. Structural fire engineers should consider the results presented in this study when designing fire protection for large compartments with low ventilation. TFM assumes that the fire starts at one end of the floor and travels to the other, whereas in our simulations, the center ignition, corner ignition, and perimeter ignition models showed outward spread in all directions in a 2D pattern. When two-dimensional fire spread was modeled, large temperature gradients through the width of the compartment were observed, whereas TFM assumes uniform temperature through the width of the compartment. Nonetheless, this study showed that TFM provides reasonable predictions of fire spread rate and fire duration, and the peak temperature of 1200 C in the near field was conservative.

6.2 Recommendations for Future Work

6.2.1 Structural Response to Parametric Study

The structural response of the composite floor system modeled in the parametric fire study should be investigated. The thermal results of the fire spread model for large compartments using a transient flux-time product model for ignition showed highly non-uniform heating along the length and width of the compartment at the ceiling. Studies that have investigated the response of floor systems to the traveling fire model (TFM) found that smaller size fires (5%-25% of the floor area) resulted in the most critical response of the structure because of the highly non-uniform heating present in the smaller-scale fires [1,34]. Additionally, one of these studies found that the

corner fire resulted in the most critical response of the structure, although this fire path is not considered within the traveling fire model [34]. Studying the structural response of the composite floor system using the results of the parametric study will allow for the investigation of the effect of two-dimensional fire spread, and the corresponding highly non-uniform heating on composite floor systems. Studies that have investigated the structural response of composite floor systems in under traveling fire only considered one-dimensional fire spread. Additionally, the fire spread model for large compartments using a transient flux-time product ignition predicted higher far field temperatures than TFM for low ventilation conditions. The structural response of the floor system to the fire model presented in this dissertation should be studied to understand if there are certain compartment or fire conditions where TFM cannot be assumed to be conservative.

6.2.2 Column Behavior in Traveling Fires

The behavior of floor systems in response to traveling fires is dependent on the response of the fire-exposed columns. The current traveling fire model assumes uniform heating of the column although studies have shown that this assumption may not be conservative [31-32,74]. In addition, columns experienced bending moments induced by thermal gradients during full-scale structural fire experiments at Cardington [75]. One disadvantage of the fire spread model for large compartments using a transient flux-time product model for ignition in its current state is the model of temperature distribution through the height of the compartment. The equivalent burner assumption, while providing accurate predictions of thermal data at the ceiling, cannot provide accurate thermal predictions through the height of the compartment. In order to understand column behavior under the proposed fire spread model in this dissertation, smaller-scale simulations should be run using computational fluid dynamics where the workstations are explicitly modeled instead of using the equivalent burner assumption. Specifically, three scenarios should be

considered (1) an interior column model surrounded by four workstations, (2) a perimeter column next to two workstations and (3) a corner column beside one workstation. These simulations should then be coupled with a finite element model of the column to understand the corresponding thermal and structural behavior of the columns when subjected to realistic temperature gradients.

6.2.3 Updated Traveling Fire Model

The work presented in this dissertation showed the traveling fire model (TFM) has limitations to accurately modeling the fire dynamics that occur in large compartments. TFM does not consider two-dimensional fire spread and instead assumes uniform temperature through the width of the compartment. The fire spread model for large compartments using a transient flux-time product model for ignition showed that significant temperature gradients can occur through the width of the compartment. Additionally, TFM was shown to underpredict gas temperatures in the far field when the compartment was not well-ventilated. In order to address these limitations, TFM should be updated to include two-dimensional fire spread. This could be done using a probabilistic model. Also, TFM should include special provisions for the far-field temperature to account for the increased gas temperatures that occur in low ventilated conditions.

6.2.4 Experimental Traveling Fire Tests

In recent years, there have been large-scale experimental tests conducted to understand traveling fire behavior in large compartments. These included the Veselí Traveling Fire Test conducted in the Czech Republic in 2011 [76-77], the BRE laboratory tests in 2013 [78], the Tisová Traveling Fire Test also conducted in the Czech Republic in 2013 [79-80], and the Malveira fire test in Portugal in 2017 [81]. Unfortunately, these tests were not conducted to model natural fires, as they included uniform fuel loads and a single fuel source. Some were explicitly set up in an attempt to validate the traveling fire methodology (TFM), which is known to not represent a real

fire. This not only limits their ability to validate realistic traveling fire models; it also prevents the study of the natural behavior of traveling fires in an experimental setting. Experimental data on natural traveling fire behavior is important for the advancement of the field. It would further advance understanding of the fire dynamics present in large compartments and allow analytical models for fire spread be further validated.

Bibliography

[1] J. Stern-Gottfried and G. Rein, “Travelling fires for structural design-Part II: Design methodology,” *Fire Saf. J.*, vol. 54, pp. 96–112, 2012, doi: 10.1016/j.firesaf.2012.06.011.

[2] A. Hamins, “Experiments and modeling of multiple workstations burning in a compartment,” *Nist Ncstar*, 2005.

[3] National Fire Protection Assosciation, “Fire loss in the United States during 2019,” *Fire J. Boston, Mass.*, 2020.

[4] R. G. Gann *et al.*, “Reconstruction of the Fires in the World Trade Center Towers,” *Nist Ncstar 1-5*, 2005.

[5] J. L. Torero, “Fire-induced structural failure: The World Trade Center, New York,” *Proc. Inst. Civ. Eng. Forensic Eng.*, vol. 164, no. 2, pp. 69–77, 2011, doi: 10.1680/feng.2011.164.2.69.

[6] NIST, “Structural Fire Response and Probable Collapse Sequence of the World Trade Centre Building 7,” *Nist Ncstar 1-9*, vol. 2, 2008.

[7] I. A. Fletcher, “Tall Concrete Buildings Subject to Vertically Moving Fires: A Case Study Apporach, Ph.D. Thesis,” University of Edinburgh, 2006.

[8] M. D. Engelhardt *et al.*, “Observations from the fire and collapse of the faculty of architecture building, delft university of technology,” *Struct. Congr. 2013 Bridg. Your Passion with Your Prof. - Proc. 2013 Struct. Congr.*, no. April, pp. 1138–1149, 2013, doi: 10.1061/9780784412848.101.

[9] H. NELSON, “Science in action. An engineering view of the fire at the First Interstate Bank Building,” *Fire J. (Boston, MA)*, vol. 83, no. 4, pp. 28–34, 1989.

[10] J. G. Routley, C. Jennings, and M. Chubb, “Highrise Office Building Fire One Meridian Plaza,” no. February, 1991.

[11] B. Behnam, “Fire Structural Response of the Plasco Building: A Preliminary Investigation Report,” *Int. J. Civ. Eng.*, vol. 17, no. 5, pp. 563–580, 2019, doi: 10.1007/s40999-018-0332-x.

[12] A. DeSimone and A. E. Jeffers, “Best practices for modeling structural boundary conditions due to a localized fire,” *Fire Mater.*, 2019, doi: 10.1002/fam.2774.

[13] “BS476-20. Fire Tests on Buildings Materials and Strucutres - Part 20: Method for Determination of the Fire Resistance of Elements of Construcution,” 1987.

[14] “ISO 834-1. Fire-resistance Tests - Elements of Building Construcution - Part 1: General Requirements.”

[15] ASTM E119, “Standard Test Methods for Fire Tests of Building Construction and Materials, ASTM International, West Conshohocken, PA,” *ASTM Int. West Conshohocken, PA*, vol. 552, no. 1, pp. 1–36, 2016, doi: 10.1520/E0119-20.These.

[16] A. A. Khan, A. Usmani, and J. L. Torero, “Evolution of fire models for estimating structural fire-resistance,” *Fire Saf. J.*, vol. 124, no. December 2020, p. 103367, 2021, doi: 10.1016/j.firesaf.2021.103367.

[17] K. Hertz, “Assessment Of Performance-based Requirements For Structural Design,” 2005, pp. 315–325, doi: 10.3801/IAFSS.FSS.8-315.

[18] EN 1991-1-2, “Eurocode 1: Actions on structures -Part 1-5: General actions - Actions on structures exposed to fire,” *Eurocode 1*, vol. 2, no. 2002, p. 61 pp, 2002.

[19] A. M. Jonsdottir and G. Rein, “Out of range,” *Fire Risk Manag.*, pp. 14–17, 2009.

[20] G. C. Clifton, “Fire Model for Large Firecells,” *HERA Rep. R4-83*, 1996.

[21] P. J. Moss and G. C. Clifton, “Modelling of the cardington LBTF steel frame building fire tests,” *Fire Mater.*, vol. 28, no. 2–4, pp. 177–198, 2004, doi: 10.1002/fam.868.

[22] B. R. Kirby, D. E. Wainman, L. N. Tomlinson, T. R. Kay, and B. N. Peacock, “Natural Fires in Large Scale Compartments,” *Int. J. Eng. Performance-Based Fire Codes*, vol. 1, no. 2, pp. 43–58, 1999.

[23] J. Stern-Gottfried and G. Rein, “Travelling fires for structural design-Part I: Literature review,” *Fire Saf. J.*, vol. 54, pp. 74–85, 2012, doi: 10.1016/j.firesaf.2012.06.003.

[24] G. Rein *et al.*, “Multi-storey fire analysis for high-rise buildings,” 2007, pp. 605–616.

[25] R. L. Alpert, “Calculation of response time of ceiling-mounted fire detectors,” *Fire Technol.*, vol. 8, no. 3, pp. 181–195, 1972, doi: 10.1007/BF02590543.

[26] E. Rackauskaite, C. Hamel, A. Law, and G. Rein, “Improved Formulation of Travelling Fires and Application to Concrete and Steel Structures,” *Structures*, vol. 3, pp. 250–260, 2015, doi: 10.1016/j.istruc.2015.06.001.

[27] X. Dai, L. Jiang, J. Maclean, S. Welch, and A. Usmani, “A conceptual framework for a design travelling fire for large compartments with fire resistant islands,” *Proc. 14th Int. Interflam Conf.*, no. August, pp. 1039–1050, 2016.

[28] X. Dai, S. Welch, and A. Usmani, “A critical review of ‘travelling fire’ scenarios for performance-based structural engineering,” *Fire Saf. J.*, vol. 91, no. April, pp. 568–578, 2017, doi: 10.1016/j.firesaf.2017.04.001.

[29] T. Wakamatsu, Y. Hasemi, and A. V. Ptchelintsev, “Heating mechanism of building components exposed to a localized fire - FEM thermal and structural analysis of a steel

beam under ceiling -," *Proc. Int. Conf. Offshore Mech. Arct. Eng. - OMAE*, vol. 2, pp. 51–58, 1997.

[30] M. L. Janssens, *An Introduction to Mathematical Fire Modeling*, 2nd Editio. CRC Press, 2000.

[31] C. Zhang, G. Q. Li, and A. Usmani, "Simulating the behavior of restrained steel beams to flame impingement from localized-fires," *J. Constr. Steel Res.*, vol. 83, pp. 156–165, 2013, doi: 10.1016/j.jcsr.2013.02.001.

[32] M. M. S. Dwaikat, V. K. R. Kodur, S. E. Quiel, and M. E. M. Garlock, "Experimental behavior of steel beam-columns subjected to fire-induced thermal gradients," *J. Constr. Steel Res.*, vol. 67, no. 1, pp. 30–38, 2011, doi: 10.1016/j.jcsr.2010.07.007.

[33] C. Zhang, L. Choe, M. Seif, and Z. Zhang, "Behavior of axially loaded steel short columns subjected to a localized fire," *J. Constr. Steel Res.*, vol. 111, pp. 103–111, 2015, doi: 10.1016/j.jcsr.2014.11.012.

[34] A. Law, J. Stern-Gottfried, M. Gillie, and G. Rein, "The influence of travelling fires on a concrete frame," *Eng. Struct.*, vol. 33, no. 5, pp. 1635–1642, 2011, doi: 10.1016/j.engstruct.2011.01.034.

[35] J. Martinez, "Finite-Element Analysis of Steel-Concrete Composite Floor Systems under Traveling Fires," Univeristy of Michigan - Ann Arbor, 2020.

[36] R. Friedman, "An International Survey of Computer Models for Fire and Smoke," *J. Fire Prot. Eng.*, vol. 4, pp. 81–92, 1992.

[37] Stephen M. Olenick and D. J. Carpenter, "An Updated International Survey of Computer Models for Fire and Smoke," *J. Struct. Fire Eng.*, vol. 13, pp. 87–110, 2003.

[38] R. Friedman, "An International Survey of Computer Models for Fire and Smoke," *J. Fire*

Prot. Eng., vol. 4, no. 3, pp. 81–92, 1992, doi: 10.1177/104239159200400301.

[39] M. J. Hurley, Ed., *SFPE Handbook of Fire Protection Engineering*, 5th ed. Springer, 2016.

[40] K. McGrattan, S. Hostikka, R. McDermott, J. Floyd, C. Weinschenk, and K. Overhold, "Sixth Edition Fire Dynamics Simulator User 's Guide (FDS)," *NIST Spec. Publ. 1019*, vol. Sixth Edit, 2020.

[41] K. Prasad and H. R. Baum, "Coupled fire dynamics and thermal response of complex building structures," *Proc. Combust. Inst.*, vol. 30, no. 2, pp. 2255–2262, 2005, doi: 10.1016/j.proci.2004.08.118.

[42] N. Tondini, A. Morbioli, O. Vassart, S. Lechêne, and J. M. Franssen, "An integrated modelling strategy between a CFD and an FE software: Methodology and application to compartment fres," *J. Struct. Fire Eng.*, vol. 7, no. 3, pp. 217–233, 2016, doi: 10.1108/JSFE-09-2016-015.

[43] C. Zhang, J. G. Silva, C. Weinschenk, D. Kamikawa, and Y. Hasemi, "Simulation Methodology for Coupled Fire-Structure Analysis: Modeling Localized Fire Tests on a Steel Column," *Fire Technol.*, vol. 52, no. 1, pp. 239–262, 2016, doi: 10.1007/s10694-015-0495-9.

[44] U. Wickström, *Temperature calculation in fire safety engineering*. 2016.

[45] C. Zhang, G. Q. Li, and R. Wang, "Using adiabatic surface temperature for thermal calculation of steel members exposed to localized fires," *Int. J. Steel Struct.*, vol. 13, no. 3, pp. 547–556, 2013, doi: 10.1007/s13296-013-3013-2.

[46] J. C. G. Silva, A. Landesmann, and F. L. B. Ribeiro, "Fire-thermomechanical interface model for performance-based analysis of structures exposed to fire," *Fire Saf. J.*, vol. 83, pp. 66–78, 2016, doi: 10.1016/j.firesaf.2016.04.007.

[47] K. J. LaMalva, Ed., *Structural Fire Engineering*. Reston, VA: American Society of Civil Engineers.

[48] D. Kamikawa, Y. Hasemi, K. Yamada, and M. Nakamura, “Mechanical responses of a steel column exposed to a localized fire,” 2006, pp. 225–234.

[49] S. Higginson and G. Morris, “Modelling Heat Transfer to a Steel-Beam,” University of Edinburgh, 2012.

[50] P. A. Beata and A. E. Jeffers, “Spatial homogenization algorithm for bridging disparities in scale between the fire and solid domains,” *Fire Saf. J.*, vol. 76, pp. 19–30, 2015, doi: 10.1016/j.firesaf.2015.05.008.

[51] X. Yu and A. E. Jeffers, “A comparison of subcycling algorithms for bridging disparities in temporal scale between the fire and solid domains,” *Fire Saf. J.*, vol. 59, pp. 55–61, 2013, doi: 10.1016/j.firesaf.2013.03.011.

[52] K. McGrattan, S. Hostikka, R. McDermott, J. Floyd, C. Weinschenk, and K. Overhold, “Sixth Edition Fire Dynamics Simulator User ’s Guide (FDS),” *NIST Spec. Publ. 1019*, vol. Sixth Edit, 2016, doi: 10.6028/NIST.SP.1019.

[53] K. McGrattan, S. Hostikka, R. McDermott, J. Floyd, C. Weinschenk, and K. Overholt, “Sixth Edition Fire Dynamics Simulator Technical Reference Guide Volume 1 : Verification guide,” vol. 1, pp. 1–147, 2015.

[54] U. Wickström, S. Hunt, B. Lattimer, J. Barnett, and C. Beyler, “Technical comment—Ten fundamental principles on defining and expressing thermal exposure as boundary conditions in fire safety engineering,” *Fire Mater.*, vol. 42, no. 8, pp. 985–988, 2018, doi: 10.1002/fam.2660.

[55] T. L. Bergman, A. S. Lavine, F. P. Incropera, and D. P. DeWitt, *Fundmentals of Heat and*

Mass Transfer, 8th Editio. John Wiley & Sons, Inc., 2011.

[56] E. E. Smith and S. Satija, "Release Rate Model for Developing Fires.," *Am. Soc. Mech. Eng.*, vol. 1, no. 81-HT-4, 1981.

[57] E. Mikkola and I. S. Wichman, "Jq-," vol. 14, no. June 1989, pp. 87–96, 1990.

[58] T. J. Shields, G. W. Silcock, and J. J. Murray, "Evaluating ignition data using the flux time product," *Fire Mater.*, vol. 18, no. 4, pp. 243–254, 1994, doi: 10.1002/fam.810180407.

[59] L. M. Kells, *Elementary Differential Equations*, 4th Ed. N.Y.: McGraw-Hill, 1954.

[60] E. J. Scott, *Transform Calculus with an Introduction to Complex Variables*, 1st Ed. Harper and Brothers, 1955.

[61] D. W. Mackowski, "Conduction Heat Transfer: Notes For MECH 7210," *Mech. Eng. Dep. Auburn …*, pp. 1–242, 2011.

[62] S. Ritchie, K. Steckler, A. Hamins, T. Cleary, J. Yang, and T. Kashiwagi, "The Effect Of Sample Size On The Heat Release Rate Of Charring Materials," *Fire Saf. Sci.*, vol. 5, pp. 177–188, 1997, doi: 10.3801/iafss.fss.5-177.

[63] R. G. G. Thomas J. Ohlemiller, George W. Mulholland, Skandakumar H. Abeyesekere, James J. Filliben, "World Trade Center Disaster Fire Tests of Single Office Workstations," *NIST Investig.*, 2005.

[64] M. M. Hirschler, "Smoke and heat release and ignitability as measures of fire hazard from burning of carpet tiles," *Fire Saf. J.*, vol. 18, no. 4, pp. 305–324, 1992, doi: 10.1016/0379-7112(92)90022-5.

[65] A. Agarwal and A. H. Varma, "Fire Induced Progressive Collapse of Steel Building Structures: The Role of Interior Gravity Columns," *Eng. Struct.*, vol. 58, pp. 129–140,

2014, doi: 10.1016/j.engstruct.2013.09.020.

[66] ICC, *International Building Code*. Falls Church, VA: Internation Code Council, 2009.

[67] *ASCE-7: Minimum design loads for buildings and other structures*, no. 7 98. 2000.

[68] *AISC-360: Specification for Structural Steel Buildings*. Chicago, IL: American Institure of Steel Construction, 2010.

[69] F. A. John L. Ruddy, Joseph P. Marlo, Socrates A. Ioannides, *AISC Design Guide 19: Fire Resistance of Structural Steel Framing*. Chicago, IL: American Institure of Steel Construction, 2003.

[70] U. Labratories, *UL Databases and Directories*. 2017.

[71] ISOLATEK, *CAFCO User's Manual*. 2008.

[72] V. Gupta *et al.*, "Ventilation effects on the thermal characteristics of fire spread modes in open-plan compartment fires," *Fire Saf. J.*, vol. 120, no. January 2020, 2021, doi: 10.1016/j.firesaf.2020.103072.

[73] NFPA, "NFPA 557 Determination of Fire Loads for Use in Strucutral Fire Protection Design." National Fire Protection Association, Quincy, MA, 2002.

[74] D. Drysdale, *An Introduction to Fire Dynamics*, 3rd Editio. John Wiley & Sons, Inc., 2011.

[75] C. Zhang, J. L. Gross, T. P. McAllister, and G.-Q. Li, "Behavior of Unrestrained and Restrained Bare Steel Columns Subjected to Localized Fire," *J. Struct. Eng.*, vol. 141, no. 10, p. 04014239, 2015, doi: 10.1061/(asce)st.1943-541x.0001225.

[76] C. G. Bailey, T. Lennon, and D. B. Moore, "The behaviour of full-scale steel-framed buildings subjected to compartment fires," *Struct. Eng.*, vol. 77, no. 8, pp. 15–21, 1999.

[77] L. E. Al Simões da Silva, *Design of composite joints for improved fire robustness*, no.

September. 2013.

[78] S. S. Huang, I. Burgess, and B. Davison, “A structural fire engineering prediction for the veselí fire tests, 2011,” *J. Struct. Fire Eng.*, vol. 4, no. 1, pp. 1–8, 2013, doi: 10.1260/2040-2317.4.1.1.

[79] J. P. Hidalgo *et al.*, “An experimental study of full-scale open floor plan enclosure fires,” *Fire Saf. J.*, vol. 89, no. February, pp. 22–40, 2017, doi: 10.1016/j.firesaf.2017.02.002.

[80] J. Degler, A. Eliasson, J. Anderson, D. Lange, and D. Rush, “A-priori modelling of the Tisova Fire Test as input to the experimental work,” *First Int. Conf. Struct. Saf. under Fire Blast*, no. September, pp. 429–438, 2015.

[81] D. Rush, D. Lange, J. Maclean, and E. Rackauskaite, “Effects of a travelling fire on a concrete column - Tisova fire test,” *Appl. Struct. Fire Eng.*, no. October, pp. 15–16, 2017, doi: 10.14311/asfe.2015.057.

[82] J. P. Hidalgo *et al.*, “The Malveira fire test: Full-scale demonstration of fire modes in open-plan compartments,” *Fire Saf. J.*, vol. 108, no. December 2018, p. 102827, 2019, doi: 10.1016/j.firesaf.2019.102827.